

AD-A080 373

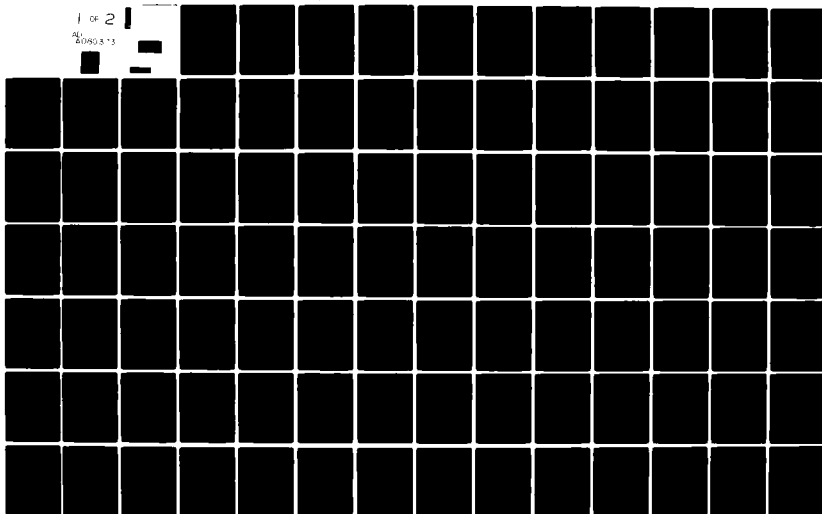
AIR FORCE INST OF TECH WRIGHT-PATTERSON AFB OH SCH00--ETC F/B 17/7
DETERMINISTIC ANALYSIS OF THE EFFECTS OF SENSOR ERRORS ON STRAP--ETC(U)
DEC 79 R H REYNOLDS
AFIT/6E/EE/79-30

UNCLASSIFIED

NL

1 of 2

AL
2080373



DISCLAIMER NOTICE

**THIS DOCUMENT IS BEST QUALITY
PRACTICABLE. THE COPY FURNISHED
TO DDC CONTAINED A SIGNIFICANT
NUMBER OF PAGES WHICH DO NOT
REPRODUCE LEGIBLY.**

AFIT/GE/EE/79-30

6 DETERMINISTIC ANALYSIS OF THE
EFFECTS OF SENSOR ERRORS ON
STRAPPED-DOWN INS PERFORMANCE.

9 Master's THESIS.

14 AFIT/GE/EE/79-30

10 Richard H. Reynolds
2nd Lt USAF

11 3 Dec 79

12 170

Approved for public release, distribution unlimited

AFIT/GE/EE/79-30

DETERMINISTIC ANALYSIS OF THE
EFFECTS OF SENSOR ERRORS ON
STRAPPED- DOWN INS PERFORMANCE

THESIS

Presented to the Faculty of the School of Engineering^v
of the Air Force Institute of Technology
Air University (ATC)
In Partial Fulfillment of the
Requirements for the Degree
Master of Science

by

Richard H. Reynolds
2nd Lt USAF

Graduate Electrical Engineering
3 December 1979

A 23
31

PREFACE

This thesis was prepared with the interest of providing insight into the causes and effects of errors in a strapped-down inertial navigation system operated in a high dynamic environment. It is hoped that the information provided will be useful for both myself and anyone else who may be involved in the development of strapped-down inertial navigation systems for use in a high dynamic environment.

I would like to thank Mr. Jack W. Bell of the Air Force Avionics Lab for his help and support in this effort. His help and support was instrumental in the completion of this thesis. Also, Mr. Bell Arranged and set up the strapped-down simulation that was used to obtain the data used in this work as well as sponsoring the entire project.

A further thanks should go to Major Salvatore Balsamo without whose classroom instruction and general guidance, this task could not have been performed. Finally, I would like to express gratitude to my wife, Melinda Canincia-Reynolds, for the support and assistance she provided.

CONTENTS

	<u>Page</u>
Preface.....	ii
List of Figures.....	v
List of Tables.....	viii
List of Symbols.....	ix
Abstract.....	xi
I. Introduction.....	1
Background.....	1
Statement of Problem.....	2
Plan of Attack.....	3
Sequence of Events.....	3
II. Description of Computer Simulation and Navigation System and Sensor Models and Their Implementation in Obtaining Data for an Error Analysis.....	4
Overview of Strapped-Down Simulation Cap- abilities.....	5
Navigation System Model.....	6
Navigation Mode Equations.....	7
Sensor Model.....	12
Accelerometer Mode.....	13
Gyro Model.....	17
Flight Profile.....	27
Summary.....	29
III. Effects of the Sensor Errors and Structural Modes on the INS Errors.....	30
Effects of Laser Gyro Errors.....	31
Gyro Bias Error.....	35
Gyro Misalignment Error.....	40
Gyro Scale Factor Error.....	44
Gyro Random Walk Error.....	45
Summary.....	45
Effects of Quartz-Flexure Accelerometer Errors.....	56

	<u>Page</u>
Accelerometer Bias Error.....	60
Accelerometer Misalignment Error.....	66
Accelerometer Scale Factor Error.....	68
Other Accelerometer Errors.....	72
Summary.....	72
Effects of Structural Modes.....	82
Summary.....	88
Conclusions.....	89
IV. Sensitivity of INS Errors to Sensor Errors.....	90
Sensitivity to Laser Gyro.....	90
Laser Gyro Misalignment Error.....	95
Laser Gyro Scale Factor Error.....	100
Laser Gyro Random Walk Error.....	104
Summary of Sensitivity to Laser Gyro Errors	104
Sensitivity to Accelerometer Errors.....	108
Accelerometer Bias Error.....	108
Accelerometer Misalignment.....	113
Other Accelerometer Errors.....	117
Summary of Sensitivity to Accelerometer... Error.....	117
Conclusions on Sensitivity Analysis.....	133
V. Conclusions and Recommendations.....	139
Conclusions.....	139
Recommendations.....	141
Bibliography.....	142
Appendices.....	143
Vita.....	155

LIST OF FIGURES

<u>Figure</u>	<u>Page</u>
1. Block Diagram of Navigation System.....	8
2 Orientation of Aircraft Body Axis.....	12
3 Quartz-Flexure Lateral Accelerometer.....	14
4 Ring Laser Roll Rate Gyro Model.....	19
5 Two-Degree-of-Freedom Roll Rate Gyro Model.....	21
6 Comparison of Position Error Time Histories with Only Gyro Errors Present.....	24
7 Description of Flight Profile.....	28
8 Simulation Results Obtained with no Structural Modes, Ideal Accelerometer, and all Laser Gyro Errors Present.....	32
9 Comparison of Error Time Histories with Laser Gyro Bias Error only, all Gyro Errors, and all Ideal Sensors.....	36
10 Comparison of Errors for Case of Laser Gyro Misalignment Error only, all Gyro Errors, and Ideal Sensors.....	41
11 Comparison of Errors for Case of Laser Gyro Scale Factor Error only, All Gyro Errors, and Ideal Sensors.....	46
12 Comparison of Errors for Case of Laser Gyro Random Walk Error only, all Gyro Errors, and Ideal Sensors.....	49
13 Simulation Results Over One Schuler Period for Case of all Laser Gyro Errors.....	53
14 Error Time Histories for Case of all Accel- erometer Errors Present.....	57
15 Comparison of Errors for Case of Accelerometer Bias Error only, all Accelerometer Errors, and Ideal Sensor.....	61
16 Comparison of Errors for Case of Accelerometer Misalignment Error only, all Accelerometer Errors, and Ideal Sensors.....	65

FigurePage

17	Comparison of Errors for Case of Accelerometer Scale Factor Error only, all Accelerometer Errors, and Ideal Sensors.....	69
18	Comparison of Errors for Case for Accelerometer Nonlinearity Error only, all Accelerometer Errors, and all Ideal Sensor.....	73
19	Comparison of Errors for Case of Accelerometer Errors only, all Accelerometer Errors, and all Ideal Sensors.....	76
20	Simulation Results Obtained Over One Schuler Period for Case of all Accelerometer Errors.....	79
21	Comparison of Errors for Case of Structural Modes and No Structural Modes.....	84
22	Comparison of Errors for Cases of All Laser Gyro Errors at Full Value, Gyro Bias Error at 50% Value, and all Ideal Sensors.....	91
23	Comparison of Errors for Cases of All Laser Gyro Errors at Full Value, Gyro Misalignment at 50% Value, and all Ideal Sensors.....	97
24	Comparison of Errors for Cases of All Laser Gyro Errors at Full Value, Gyro Scale Factor Reduced 50%, and All Ideal Sensors.....	101
25	Comparison of Error for Cases of All Laser Gyro Errors at Full Value, Gyro Random Walk Reduced 50%, and All Ideal Sensors.....	105
26	Comparison of Error Cases of All Laser Gyro Errors at Full Value, and All Reduced 50%.....	109
27	Comparison of Errors for Cases of All Accelerometer Errors at Full Value, Accelerometer Bias Reduced 50%, and All Ideal Sensor.....	114
28	Comparison of Errors for Cases of All Accelerometer Errors at Full Value, Accelerometer Misalignment Reduced 50%, and Ideal Sensor.....	118
29	Comparison of Errors for Cases of All Accelerometer Errors at Full Value, Accelerometer Scale Factor Reduced 50%, and Ideal Sensors.....	121
30	Comparison of Errors for Cases of All Accelerometer Errors at Full Value, Accelerometer Cross-Coupling Reduced 50%, and Ideal Sensor....	124

Figure

Page

31	Comparison of Errors for Cases of All Accelerometer Errors at Full Value, Accelerometer Nonlinearity Reduced 50%, and Ideal Sensors.....	127
32	Comparison of Errors for Cases of All Accelerometer Errors at Full Value, All Reduced 50%.....	130
33	Comparison of Errors for Cases of All Sensor Errors at Full Value and all Reduced 50%..	135
C-1	Wander Azimuth (Computation) and Earth Coordinated Frames (Ref 2:9).....	150
C-2	Wander Azimuth (Computation) and Body Coordinate Frames (Ref 2:13).....	152

LIST OF TABLES

<u>Table</u>		<u>Page</u>
I	Quartz-Flexure Accelerometer Nominal Values.....	16
II	Laser Gyro Nominal Values.....	22
III	Two-Degree-of-Freedom Nominal Values.....	23
IV	Laser Gyro Error Sensitivity.....	112
V	Accelerometer Error Sensitivity.....	134

LIST OF SYMBOLS

<u>Symbol</u>	<u>Definition</u>
\underline{f}	Specific Force Vector
C_b^c	Matrix to Transform a Vector from Computational Frame to Body Frame
\underline{w}_{ce}	Rotation Rate of Frame e with Respect to Frame c
\underline{V}	Velocity Vector
α	Wander Angle
ϕ	Roll Rate
θ	Pitch Angle
ψ	Yaw Angle
L	Latitude
l	Longitude
\underline{g}	Gravity Vector
R_o	Radius of Earth (Assume Spherical Earth)
h	Altitude Above Earth's Surface
\underline{w}_{ce}^{ck}	Skew Symmetric Form of \underline{w}_{ce}^c
A_y	Longitudinal Acceleration Including Bending Effects
Δt	Sample time
γ_1, γ_2	Accelerometer Misalignment Error Coefficients
τ	Lag Time Constant
ϵ_{BIAS}	Sensor Bias Error
C_{yx}	Accelerometer Cross-Coupling Error
C_{yy}	Accelerometer Nonlinearity Error
SF_A	Accelerometer Scale Factor

<u>Symbol</u>	<u>Definition</u>
A	Accelerometer Scale Factor Error
Vy	Incremental Value of Lateral Velocity
	Incremental Value of Rotation Rate
μ_1, μ_2	Gyro Misalignment Coefficients
E_{WALK}	Gyro Random Walk Error
SF_G	Gyro Scale Factor
ϵ_G	Gyro Scale Factor Error
$\Delta\theta_z$	Incremental Value of Roll Angle
p	Indicates Time Derivative
r	Position Vector
<u>Subscripts</u>	
x,y,z	Vector Components
I	Indicates Quantity has been Integrated
M	Indicates Quantity Includes Misalignment Effects
L	Indicates Quantity has Passed Through a Lag
k	Iteration Number
B	Indicates Quantity Includes Bias Error
N	Indicates Quantity Includes Nonlinearity Error
Q	Indicates Quantity has been Quantized
C	Indicates Quantity Includes Cross-Coupling Error
<u>Subscript or Superscript</u>	
e	Indicates Earth Frame
i	Indicates Inertial Frame
c	Indicates Computational Frame
b	Indicates Body Frame

ABSTRACT

The operation of a strapped-down inertial navigation system in a high dynamic environment was simulated. Its performance was assessed using a laser gyro and a quartz-flexure accelerometer as the sensors. Using deterministic values for the sensor errors, the effects of the sensor errors on the INS performance was assessed. Emphasis is placed on the effects that the sensor errors have on the INS errors in a high dynamic environment. Structural mode effects on INS performance are also evaluated. Following this an analysis of the sensitivity of the INS errors in position and velocity to each inertial sensor is determined. Using this sensitivity analysis, the sensor parameters required to obtain a performance specification of ≤ 1 nm/hr position error and ≤ 3 ft/sec velocity error are defined. Finally, recommendations of areas for improvement are presented.

CHAPTER I

INTRODUCTION

Background

It would be difficult, if not impossible, to determine when the first inertial navigation system was developed. The first patent for an assemblage of three gyros and a gravity vertical as a navigation system was given in 1924 to an American, C.G. Abbot. Since that time much effort has been spent in regards to inertial navigation systems (INS). During the 1930's the concept of using accelerometers mounted on a stabilized platform was utilized (Ref 5:8-12).

Through the years many different types of INS have been designed, but they can be classified under two distinct groups, strapped-down and gimbaled systems. The distinguishing feature of these two groups is the way in which their orientation with respect to inertial space is maintained. In the case of most gimbaled systems the platform is mounted with gimbales such that it remains fixed in some orientation with respect to inertial space regardless of the movements of the body on which it is mounted. The strapped-down systems are fixed to the body and, therefore, the relation of the platform frame to inertial space is maintained by updating the transformation matrices using the information received from the gyros. Because of the

extra computational load required for the strapped-down systems to maintain orientation with inertial space, this group of systems received little attention until the 1960's. As computer technology progressed, the size and weight of equipment necessary to handle this additional computational load was drastically reduced and more emphasis was placed on strapped-down systems. As further refinements have been and are being made in the area of micro computers during the seventies, development of the laser gyro also progressed. With these advances in technology, the potential of the strapped-down systems have grown. Possible advantages that strapped-down systems could have over gimbaled systems include smaller size, less weight, and greater maintainability and reliability. With these factors in mind, future commitments of resources and money for furthering the development of the strapped-down INS is desirable (Ref 2:1).

Statement of Problem

Past analysis of inertial navigation systems has shown that the gimbaled systems are more accurate than the strapped-down systems. The implications are that the reason for this difference in performance of the strapped-down and gimbaled INS is due to the harsher environment that the strapped-down is subjected to. An analysis of the error propagation of the sensor errors should give insight into the effect of the sensor errors on the total system errors (Ref 7:37-38). This

would then be a basis for working at improving the strapped-down INS performance. In undertaking this error analysis, a digital strapped-down INS simulation recently developed by the Charles Stark Draper Lab under contract to the Air Force Avionics Lab at Wright-Patterson AFB is utilized.

Plan of Attack

Using the strapped-down INS simulation developed by the Draper Lab, a series of INS error time histories will be generated. From examining the time histories, the effect of the sensor errors on the INS errors will be evaluated. By changing the values of the sensors errors, the sensitivity of INS errors to sensor errors will be developed. Finally, the sensor parameters necessary to achieve a position error of ≤ 1 nm/hr and a velocity error of ≤ 3 ft/sec will be determined.

Sequence of Events

A general overview of the capabilities of the strapped-down INS simulation is presented first. Following this, a detailed description of the sensor and navigation models is presented. Also, a description of the flight profile and sensor parameters used in the simulations is given. Based on the simulation analysis of the effect of sensor errors on INS errors is performed. Conclusions are then drawn from this analysis.

CHAPTER II

Description of Computer Simulation and Navigation System and Sensor Model and Their Implementation in Obtaining Data for an Error Analysis

The strapped-down inertial navigation system simulation referenced in the introduction provided the data that is used in the error analysis that is presented in later chapters. The simulation is a digital computer program coded in FORTRAN and is implemented on a CDC 6600 computer. The program was designed for ease of user interaction, and proved to be a useful tool for analyzing inertial navigation system errors.

This section provides a brief introduction to the capabilities of the strapped-down simulation. A detailed description of the navigation system and its associated inertial sensors are then presented. Finally, the flight profile used to generate the simulations for the error analysis is described.

Overview of Strapped-Down Simulation Capabilities

The strapped-down inertial navigation system simulation (SDINS) employs an F-4 aircraft model. Nonlinear six-degrees-of-freedom equations of motion and nonlinear aero dynamics valid beyond the stall-angle-of-attack are implemented. Bending effects as well as three longitudinal-and three lateral-directional structural modes are included.

The capability for perturbation inputs such as winds and gusts is also available. The other models included are those for a flight-control system, navigation system, and their associated sensors, as well as a gravity model. In the work done for this paper, a rotating spherical earth model is used for the computations, but an elliptical model is provided in the simulation.

This is only a brief overview of the strapped-down INS simulation program. Since this work is only concerned with the details of the actual navigation model and its associated sensors, this portion of the system is now described in detail.

Navigation System Model

Presented here is the algorithm used in the strapped-down INS simulation to represent a strapped-down Local Vertical Wander Azimuth (LVWA) navigation system. The following discussion of this algorithm is based on information taken from reference (2). The navigation model can be divided into two major subsections, a low-speed loop computed at 5 hertz and a high-speed loop computed at 50 hertz. This representation results from the need to update the body-to-computational transformation matrix at a high frequency in order to maintain accuracy; while the other computations need not be performed at this high of an iteration rate.

The high speed navigation loop consists of updating the body-to-computational or local-vertical wander azimuth transformation matrix, and transforming the navigation sensor velocities from the body frame to the computational frame and the summation of these velocities over the low speed computational time period. The generation of the body-to-computational transformation matrix and transformation of the velocities are staggered in time; with the transformation matrix being computed midway between the times at which the transformation of the velocities occur. The update of this transformation matrix is achieved using a third order quaternion. It is from this body-to-computational frame transformation matrix that the attitude angles are computed for comparison with the corresponding true angles generated in the vehicle portion of the simulation.

The function of the low-speed portion of the system model is to perform the necessary operations on the sensor signals in order to find position and velocities. All signals are defined in the computational frame, but a transformation matrix for transforming from computational frame to earth frame is maintained. It is from this transformation matrix that latitude, longitude, and wander angle are obtained (Appendix C derives the transformation in terms of these quantities). The velocities are taken from the integration of the accelerometer signals. A further integration of the vertical channel velocity yields altitude.

Since the vertical channel of an inertial navigation system is unstable without aiding, a third-order damping scheme is applied.

The equations implemented in the navigation model are now examined. Appendix A provides a review of the notation and reference frames that are used. It should be noted that the local vertical wander azimuth frame is the same frame as the computational frame and it is referred to as the computational frame in the following discussion. The x, y, and z coordinates of this frame are defined in an up, east, and north sense (Ref 1:49-51).

Navigation Model Equations

Figure 1 shows a block diagram of the basic inertial navigation system model. The accelerometers provide a measure of the specific force. The measurement is in the body frame and must be transformed to the computational frame. Thus,

$$\underline{f}^c = C_b^c \underline{f}^b \quad (1)$$

where \underline{f} represents specific force, and C_b^c is the transformation matrix to transform from the body frame to the computational frame, and c and b represent computational frame and body frame, respectively.

The block labeled I represents the integration of the velocity differential equation that is derived in Appendix B. This equation is

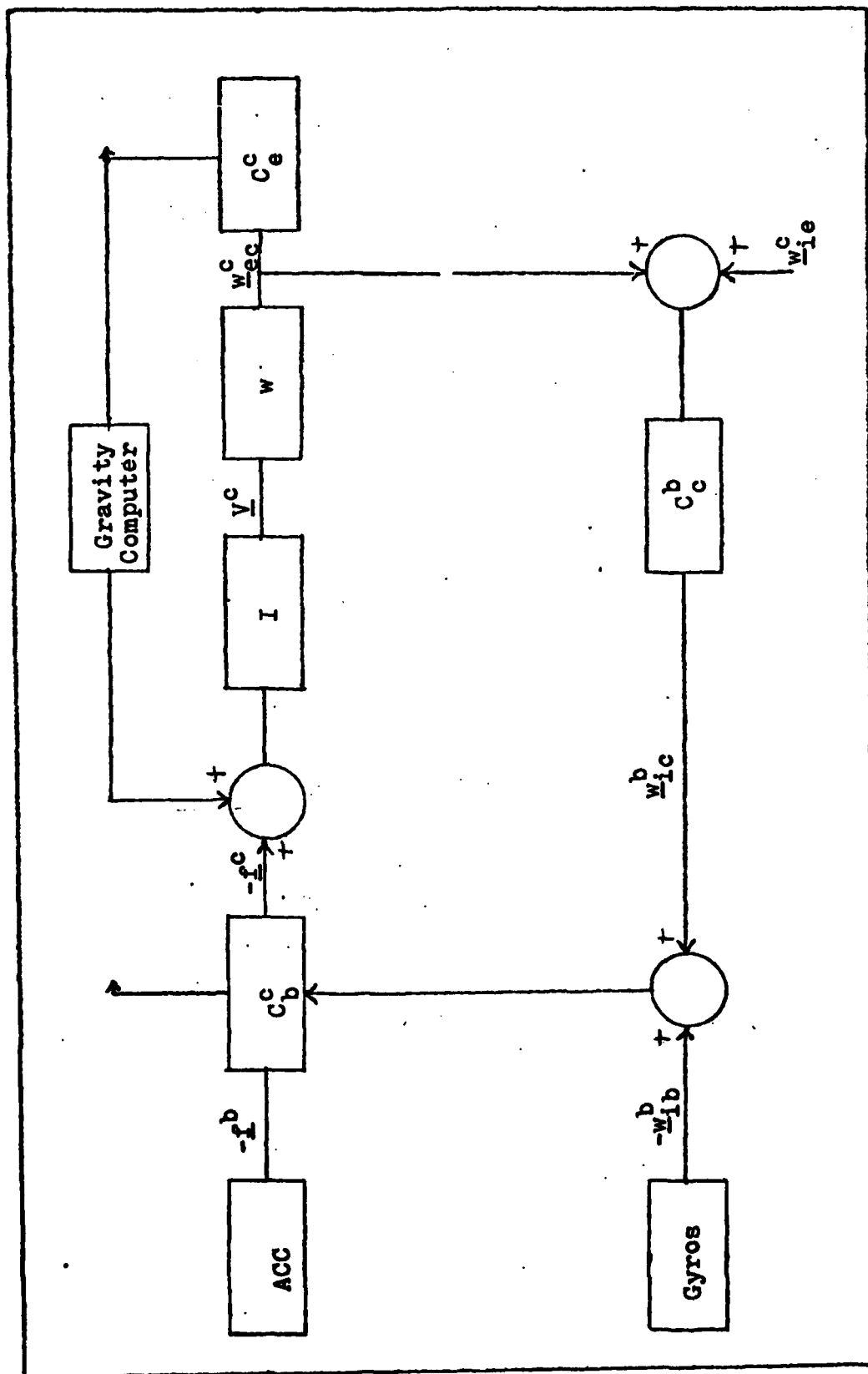


Figure 1. Block Diagram of Navigation System (Ref 2:41)

$$\dot{\underline{v}}^c = \underline{f}^c + \underline{g}^c - (2\underline{w}_{ie}^c + \underline{w}_{ec}^c) \times \underline{v}^c \quad (2)$$

where \underline{g} represents the acceleration due to gravity, \underline{w}_{ie} represents the rotation rate of the earth frame with respect to the inertial frame, and \underline{w}_{ec} represents the rotation rate of the computational frame with respect to the earth frame.

By dividing the proper components of \underline{v}^c , the components of \underline{w}_{ec}^c are computed. (The block labeled w represents these calculations). They are

$$w_{ecy}^c = -v_{ecz}^c / (R_0 + h) \quad (3)$$

and

$$w_{ecz}^c = v_{ecy}^c / (R_0 + h) \quad (4)$$

where R_0 is the radius of the earth (assuming spherical earth) and h is the altitude above the earth's surface. ($w_{ecx}^c = 0$ since the x axis is the vertical axis). \underline{w}_{ec}^c is then fed back to be used in the velocity differential equations. \underline{w}_{ec}^c is also used to formulate \underline{C}_e^c , the transformation matrix to transform a vector from the earth frame to the computational frame. To do this, (using the fact $\underline{w}_{ec}^c = -\underline{w}_{ce}^c$), the skew symmetric form of $-\underline{w}_{ce}^c$ is found.

$$\underline{w}_{ce}^{ck} = \begin{bmatrix} 0 & -w_{cez} & w_{cey} \\ w_{cez} & 0 & -w_{cex} \\ -w_{cey} & w_{cex} & 0 \end{bmatrix} \quad (5)$$

Then this matrix is used in the formulation of the rate of change of a direction cosine matrix:

$$\dot{C}_e^c = \underline{w}_{ce}^{ck} C_e^c \quad (6)$$

It is then from C_e^c that latitude, longitude, and wander angle are calculated. (Appendix C provides the derivation of C_e^c in terms of these quantities).

The gyros provide a measure of the angular rate of the body frame with respect to inertial space, \underline{w}_{ib}^b . This is then differenced with \underline{w}_{ic}^b resulting in

$$\underline{w}_{bc}^b = \underline{w}_{ib}^b - \underline{w}_{ic}^b \quad (7)$$

where \underline{w}_{ic}^b , the rotation rate of the computational frame relative to inertial space is determined by adding \underline{w}_{ie}^c to \underline{w}_{ec}^c and then transforming to the body frame.

$$\underline{w}_{ic}^b = C_c^b (\underline{w}_{ie}^c + \underline{w}_{ec}^c) \quad (8)$$

The quantity \underline{w}_{ie}^c , the angular velocity of the earth frame relative to inertial space, is used in the velocity differential equation as well as in equation (8). Assuming a spherical earth rotating at a constant rate,

$$\underline{w}_{ie}^e = \begin{bmatrix} 0 \\ 0 \\ w_{ie} \end{bmatrix} \quad (9)$$

where w_{ie} is the rate of the earth's rotation, $15^\circ/\text{hr}$.
Thus,

$$\underline{w}_{ie}^c = C_e^c \underline{w}_{ie}^e \quad (10)$$

Completing the gyro loop of the diagram in figure 1 requires the calculation of C_b^c . In order to maintain the desired accuracy in calculating C_b^c , a third order quaternion update is used instead of the direction cosine differential equation. However, just as \underline{w}_{ec}^c is needed to calculate C_e^c , \underline{w}_{bc}^b is needed to perform the quaternion update. Following the calculation of C_b^c , the Euler angles, roll, pitch, and yaw, are computed using the elements of C_b^c (Ref 2:22-31). (Appendix C provides a derivation of C_b^c in terms of the Euler angles).

$$g_x = -g_0 \left[1 - 2(h/R_0) + 3(h/R_0)^2 \right] + w_{ie}^2 \cdot R_0 (1 + h/R_0) (1 - \sin^2 L) \quad (11)$$

$$g_y = -w_{ie}^2 \cdot R_0 (1 + h/R_0) \sin L (-\cos L \sin \alpha) \quad (12)$$

$$g_z = -w_{ie}^2 \cdot R_0 (1 + h/R_0) \sin L (\cos L \cos \alpha) \quad (13)$$

where g_0 is the gravity constant ($g_0 = 32.1725 \text{ ft/sec}^2$),
 R_0 is the radius of the earth ($R_0 = 20,860,000 \text{ feet}$), L
is the latitude, and α is the wander angle.

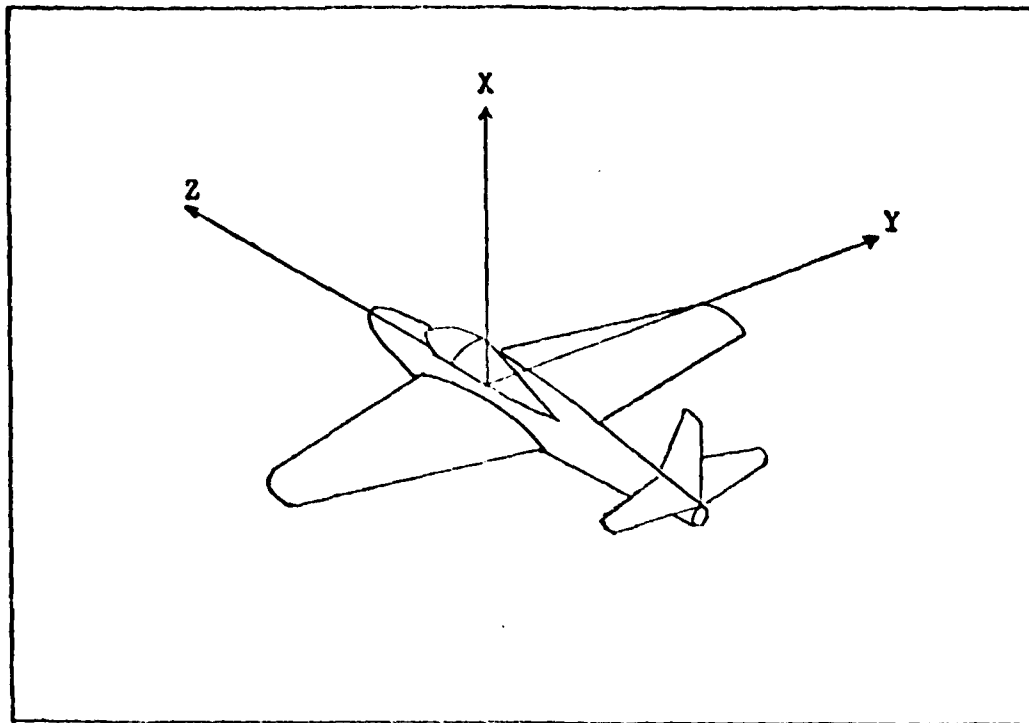


Figure 2. Orientation of Aircraft Body Axis.

A final note on the navigation algorithm before examining the sensor models that are used to generate the navigation algorithm inputs concerns the generation of errors in position, velocity, and attitude. These errors are generated by the differencing the navigation model outputs with those from the aircraft equations-of-motion. Therefore, the error quantities include effects from computational errors (Ref 1: 58).

Sensor Model

Figure 2 shows the orientation of the aircraft body axis. There are three gyros and three accelerometers modeled for the navigation system. Each gyro measures the rotation rate about one of the principle body axis. Similarly,

there is an accelerometer located on each body axis. It is with reference to this configuration that the discussion on the gyro and accelerometer models is based. Also, only the roll-rate (Z axis) gyro model and the lateral (Y axis) accelerometer model are presented since they are representative of the others. The accelerometer model is presented first and is followed by the gyro model.

Accelerometer Model

The accelerometer implemented in the strapped-down INS simulation is representative of the quartz-flexure class of accelerometers. The accelerometer error sources modeled include misalignment, bias, scale factor, cross-coupling, and nonlinearity. The model assumes that the statistical data on these error sources for a specific instrument are supplied as a simulation input. Also, the model has a limiter to limit the accelerations to $\pm 10 \cdot g$.

Figure 3 shows a block diagram of the lateral accelerometer model. The input signal, A, represents the rigid body acceleration including bending effects. This signal is integrated using a rectangular integration scheme. Thus,

$$A_{yI} = \frac{A_{yk} + A_{y(k-1)}}{2} \cdot \Delta t \quad (14)$$

where the subscript I represents an integrated signal, k and k-1 represents the iteration number, and Δt is the period between samples. At this point, the effects of the misalignment

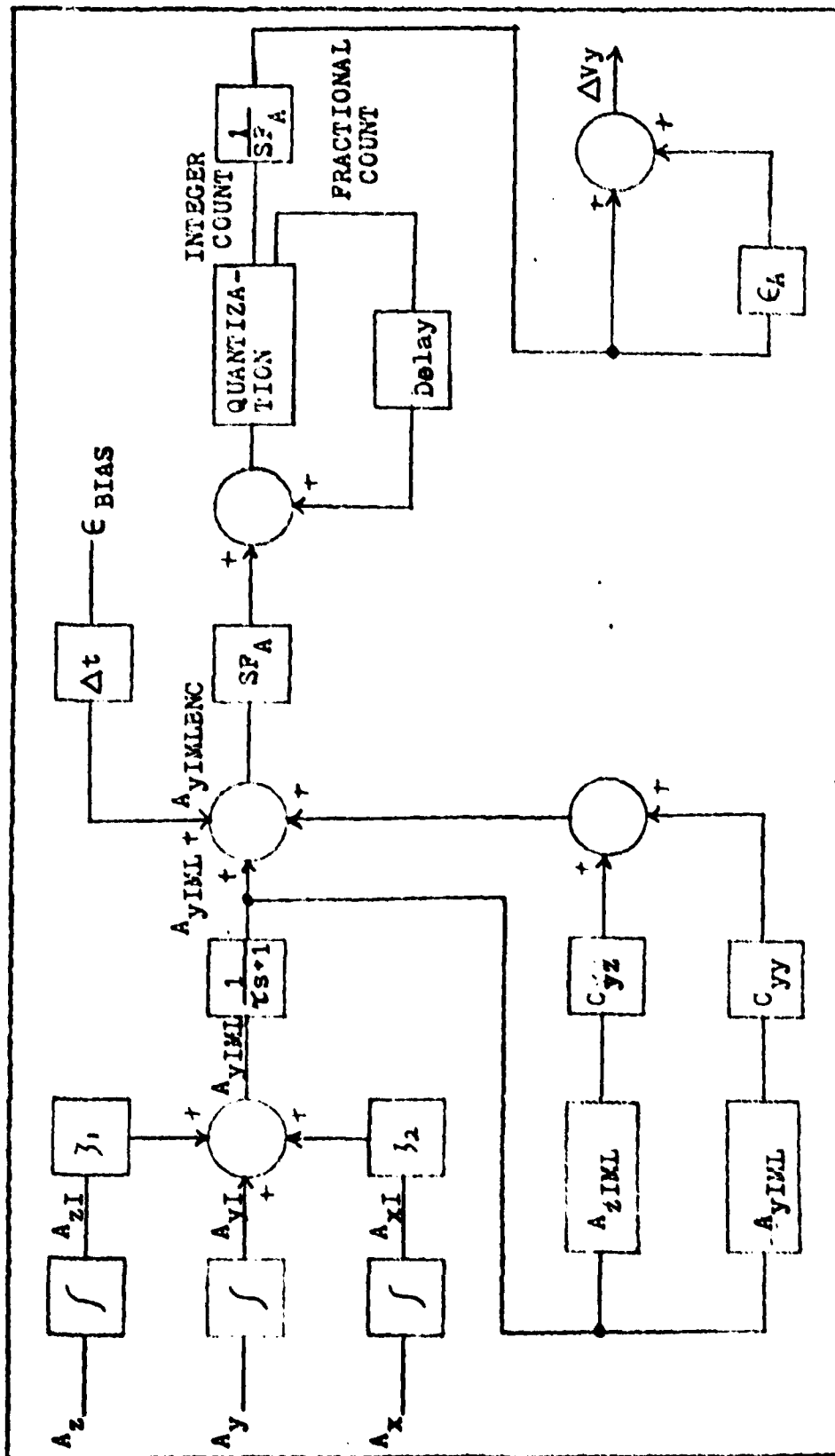


Figure 3. Quartz-Plexure Lateral Accelerometer Model (Ref 1:48)

error are accounted for. The coefficient of misalignment, γ , is multiplied by the respective signal and then added to the integrated lateral acceleration. Therefore,

$$A_{yIM} = A_{yI} + \gamma_1 A_{xI} + \gamma_2 A_{zI} \quad (15)$$

where the subscript M represents signal with misalignment effects and represents the other acceleration signals after they are integrated. This signal is now fed through a first order lag to represent the delays of the instrument.

$$A_{yIML} = A_{yIM} (1/(\gamma s + 1)) \quad (16)$$

where γ = time constant of the lag and subscript L indicates the signal passes through a lag. The bias error is added to the accelerometer signal after it passes through the lag network.

$$A_{yIMLB} = A_{yIML} + \epsilon_{BIAS} \cdot \Delta t \quad (17)$$

where subscript B represents signal with bias effects and ϵ_{BIAS} represents the statistical value for the bias error as stated in the specifications for the accelerometer used. Before the quantization, the nonlinearity error and cross-coupling error are accounted for,

$$A_{yIMLBNC} = A_{yIMLB} + (C_{yx} A_{xIMLB} + C_{yy} A_{yIMLB}) A_{yIMLB} \quad (18)$$

Table I

Quartz-Flexure Accelerometer Nominal Values (Ref 1:70)

Parameter	Symbol	Value
Misalignment Coefficients	β_1, β_2	5×10^{-5} rad
Time Constant of Lag	τ	1×10^{-6} sec
Scale Factor	SF_A	32,000 pps/g
Bias Error	ϵ_{Bias}	50 g
Cross-Coupling Coefficients	C_{yx}	19.6×10^{-5} rad/sec
Nonlinearity Coefficients	C_{yy}	40 g/g ²
Scale Factor Error	ϵ_A	100 ppm

where subscripts M and C represent nonlinearity and cross-coupling coefficient and C_{yy} is the nonlinearity coefficient. This signal is now converted to pulses by the scale factor, SF_A , and then quantized.

Table 1 shows a listing of the parameter values that are used for the accelerometer in the simulations that were made for this work. The error parameter values are the deterministic tolerances as listed in manufacturer's performance specifications for a quartz-flexure accelerometer. These figures are representative of presently available instruments, but do not necessarily reflect the limit of achievable performance.

The quantization takes an integer count of the value of the present signal plus the value of the fractional part of the previous sample period integer count. This integer count is then divided by the scale factor and the effects of the scale factor error are accounted for resulting in the incremental value of the lateral velocity,

$$\Delta V_y = (1/SF_A)(1+E_A)A_{yIMLBNCQ} \quad (19)$$

where E_A is the scale factor error and subscript Q represents the signal including quantization and scale factor. The incremental velocities are then summed up in the navigation system subroutine of the strapped-down INS simulation to be used in the calculation of velocity. This summation, as was mentioned in the navigation algorithm description, is done at a higher iteration rate than the rate at which the velocity differential equation is solved (50 hertz as opposed to 5 hertz)(Ref 1:47-49).

Gyro Model

Two types of gyros are modeled in the strapped-down INS simulation. They are laser gyro and two-degree-of-freedom mechanical gyro. There are three of each type modeled, one for measuring rotation rate about each of the three body axis. The roll-rate laser gyro is described here and then differences of the two-degree-of-freedom gyro are pointed out. Once again, statistical data on the instrument error is assumed available. Error sources

modeled include bias, misalignment, and scale factor.

An illustration of the block diagram for the roll rate laser gyro is shown in Figure 4. w_z , the angular inertial velocity about the body roll axis including bending effects is fed into an integrator. Once again a rectangular integration routine is used. Therefore,

$$\beta_{zI} = \frac{w_{zk} + w_{z(k-1)}}{2} \cdot \Delta t \quad (20)$$

After interpretation, the effects of misalignment error are accounted for, resulting in

$$\beta_{zIM} = \beta_{zI} + K_1 \beta_{xI} + K_2 \beta_{yI} \quad (21)$$

where K_1 and K_2 represent the coefficients of misalignment for their respective signals. The bias error is now added to the roll rate signal. It is a function of the time period and not of a rotation magnitude. Also, at this point, the random walk is accounted for, resulting in,

$$\beta_{zIMB} = \beta_{zIM} + \epsilon_{BIAS} \Delta t + R_L (\Delta t)^{\frac{1}{2}} \quad (22)$$

where ϵ_{BIAS} is the bias error and R_L is the random walk error. ($R_L = E_{WALK} * RAN$, where E_{WALK} is the tolerance specification and RAN is a random number). The signal is now converted to pulses via the scale factor, SF_G :

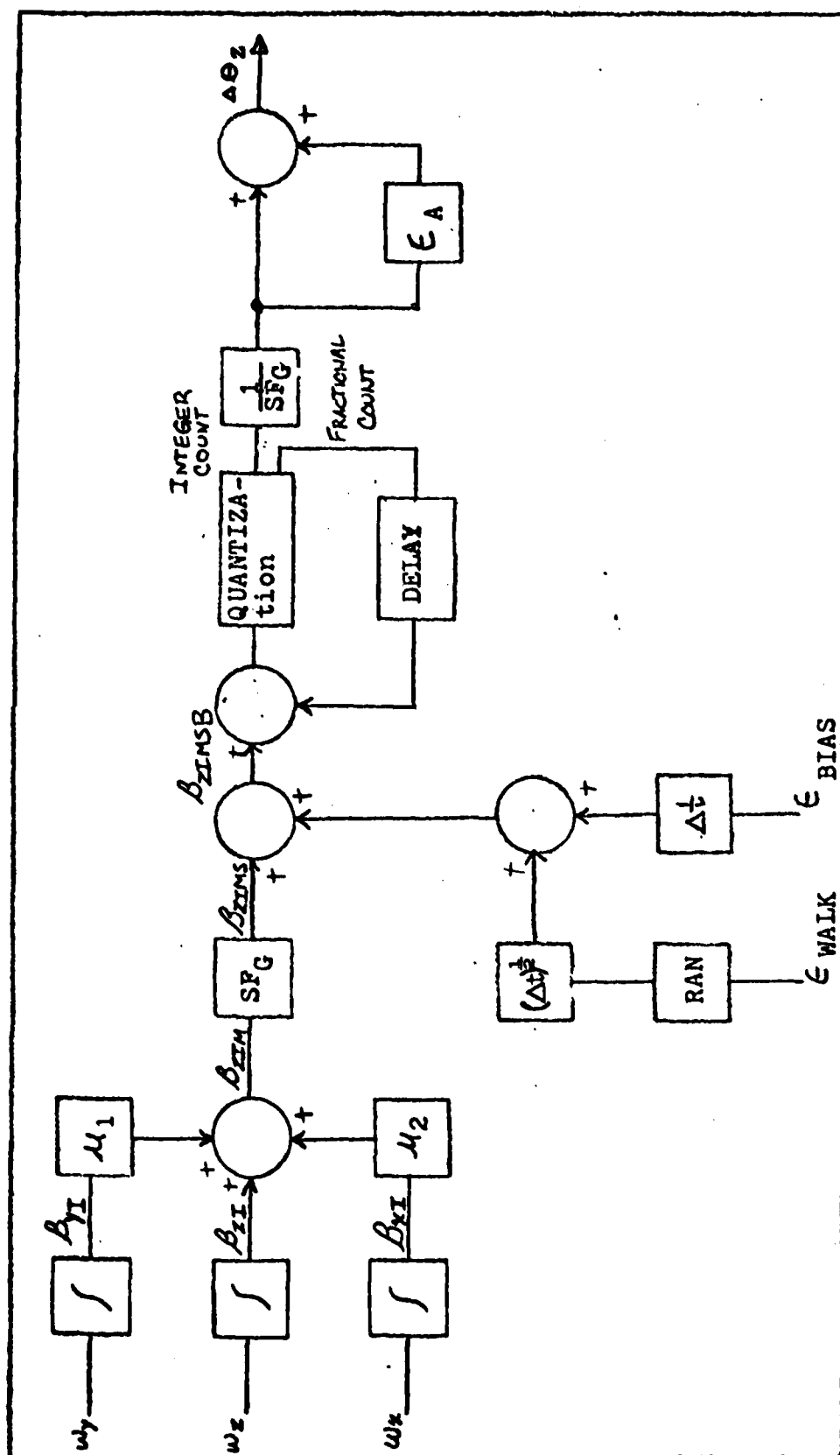


Figure 4. Ring Laser Roll Rate Gyro Model (Ref 1.46)

$$\beta_{zIMBS} = \beta_{zIMB}(SF_G) \quad (23)$$

This signal is then quantized as in the case of the accelerometer model, and then is multiplied by the inverse of the scale factor. The error in scale factor is then taken into account resulting in incremental value of the roll axis rotation.

$$\Delta\Theta_z = (1/SF_G)(\beta_{zIMBS})(1 + \epsilon_G) \quad (24)$$

where ϵ_G is the error in scale factor. This signal is now summed in the high speed loop of the navigation system models before being used in the calculation of the velocity and position (Ref 1:46-47).

Figure 5 shows a block diagram of the roll channel of the two-degree-of-freedom mechanical gyro model. This model is the same as the laser gyro except that it accounts for errors peculiar to the two-degree-of-freedom mechanical gyro. These errors are the acceleration dependent and angular dependent terms. Also, the laser gyro model requires a lag to account for delays that are not present in the laser gyro model (Ref 3:22-25).

The values of the parameters used in the laser gyro and two-degree-of-freedom mechanical gyro, when obtaining the simulations for the error analysis, are listed in Tables II and III. These values are representative of presently available sensors.

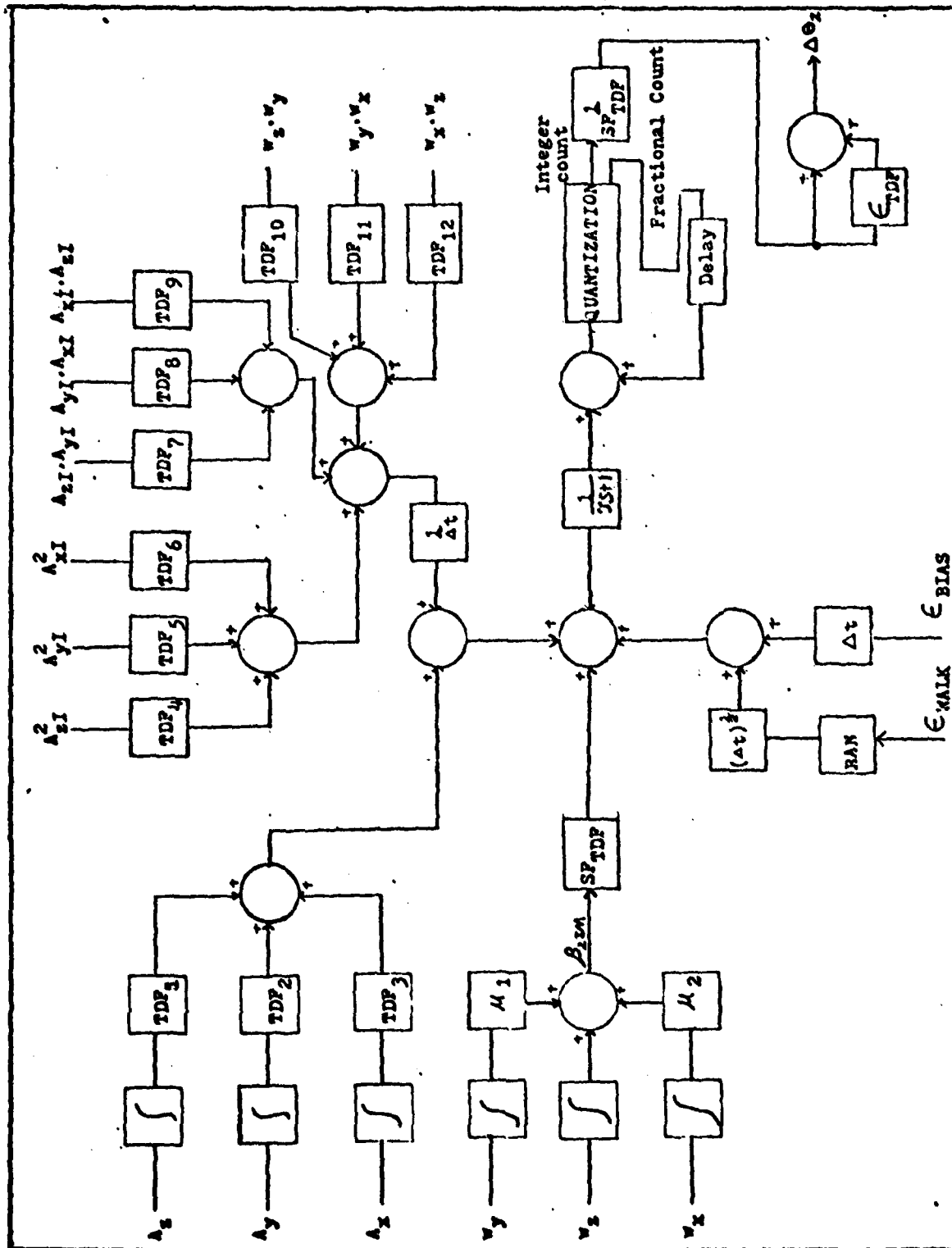


Figure 5. Two-Degree-of-Freedom Roll Rate Gyro Model (Ref. 3:25)

Table II
Laser Gyro Nominal Values (Ref 1:70)

Parameter	Symbol	Value
Misalignment Coefficients	M_1, M_2	5×10^{-5} rad
Scale Factor	SFG	1.57 sec/pulse
Bias Error	Bias	0.01 °/hr
Scale Factor Error	ϵ_G	5×10^{-6} ppm
Random Walk Error	ϵ_{walk}	0.005 °/hr

Since the two types of gyro models are available for the simulations, a comparison of the results of the simulation using each gyro model is made. Figure 6 shows the INS error time histories obtained for both simulations. The laser gyro provides better overall performance than the two-degree-of-freedom mechanical gyro; and it has the additional errors due to acceleration and angular rate dependent terms. Based on these results, the laser gyro is chosen for the simulations used in this work.

TABLE III

Two-Degree-of-Freedom Gyro Nominal Values (Ref 3:36)

Parameters	Symbol	Z-Output -Axis	Y-Output -Axis	Source
Misalignment Coefficients	M_1, M_2	10^{-4} rad	10^{-4} rad	
Scale Factor	SP_G	$1.57 \frac{\text{sec}}{\text{pulse}}$	$1.57 \frac{\text{sec}}{\text{pulse}}$	
Bias Error	ϵ_{Bias}	$0.01 \frac{\text{deg}}{\text{hr}}$	$0.01 \frac{\text{deg}}{\text{hr}}$	
Scale Factor Error	ϵ_{TDF}	50 ppm	50 ppm	
g -Dependent Errors	TDF_1	0.02	0.04	
	TDF_2	$0.04 \frac{\text{deg}}{g}$	0.02	
	TDF_3	$0.01 \frac{h}{g}$	0.01	
g^2 -Dependent Errors	TDF_4	0.02	0.0	A_z
	TDF_5	$0.00 \frac{\text{deg}}{g}$	$0.02 \frac{\text{deg}}{g}$	A_y
	TDF_6	$0.005 \frac{h^2}{g}$	$0.005 \frac{h^2}{g}$	A_x
g_{xg} -Dependent Errors	TDF_7	0.01	0.01	A_z^2
	TDF_8	$0.04 \frac{\text{deg}}{h^2}$	$0.04 \frac{\text{deg}}{h^2}$	A_z^2
	TDF_9	$0.04 \frac{h^2}{g}$	$0.04 \frac{h^2}{g}$	A_y^2
w_{xw} -Dependent Errors	TDF_{10}	$0.00 \frac{\text{deg}}{h}$	0.00	w_y
	TDF_{11}	80	20	w_x
	TDF_{12}	$20 \frac{(\text{rad})^2}{\text{sec}}$	80	w_z

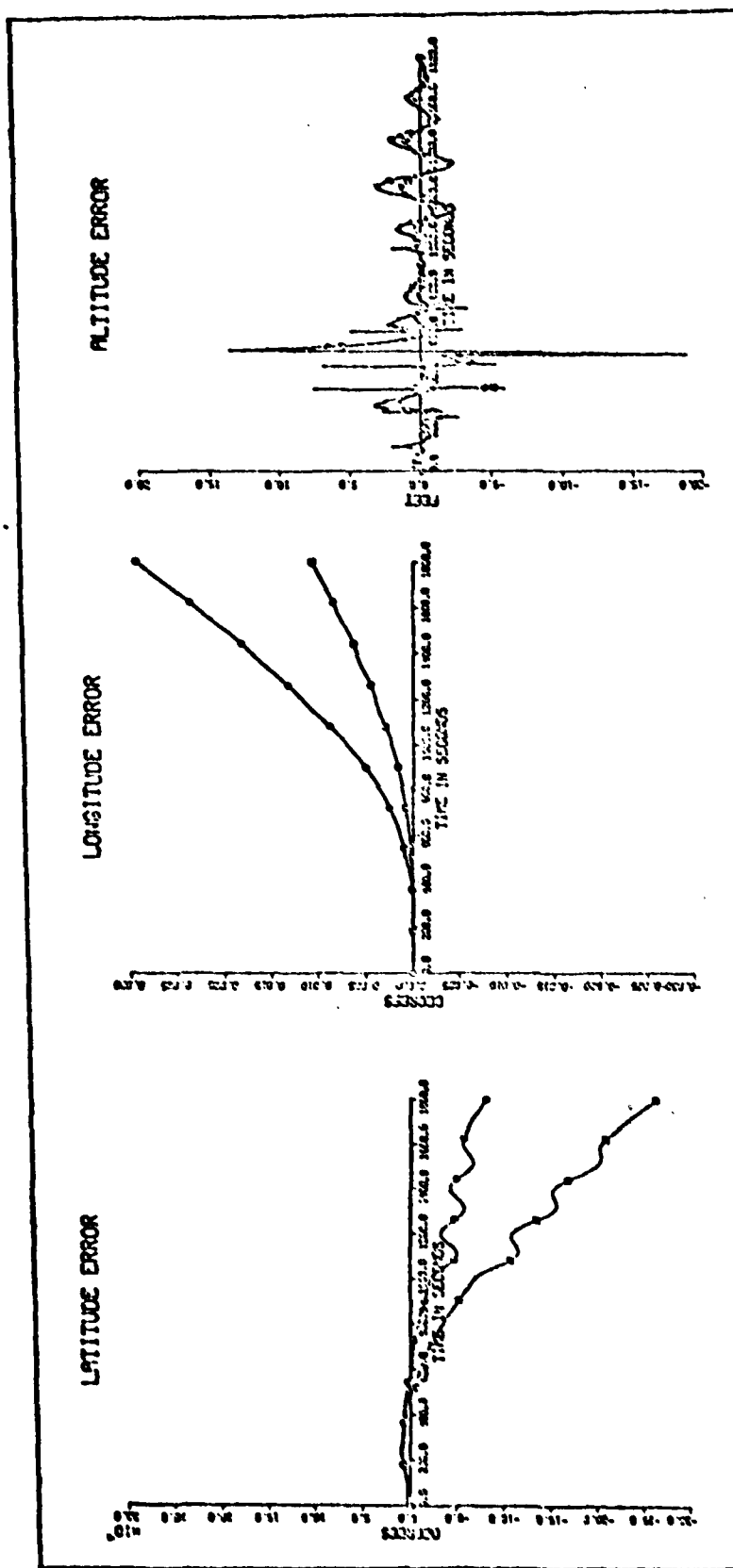


Figure 6a. Comparison of Position Error Time Histories with only Gyro Errors Present

- Represents results obtained using ring-laser gyro.
- Represents results obtained using two-degree-of-freedom gyro.

THIS PAGE IS UNCLASSIFIED
DATE 11-11-2011 BY 60322

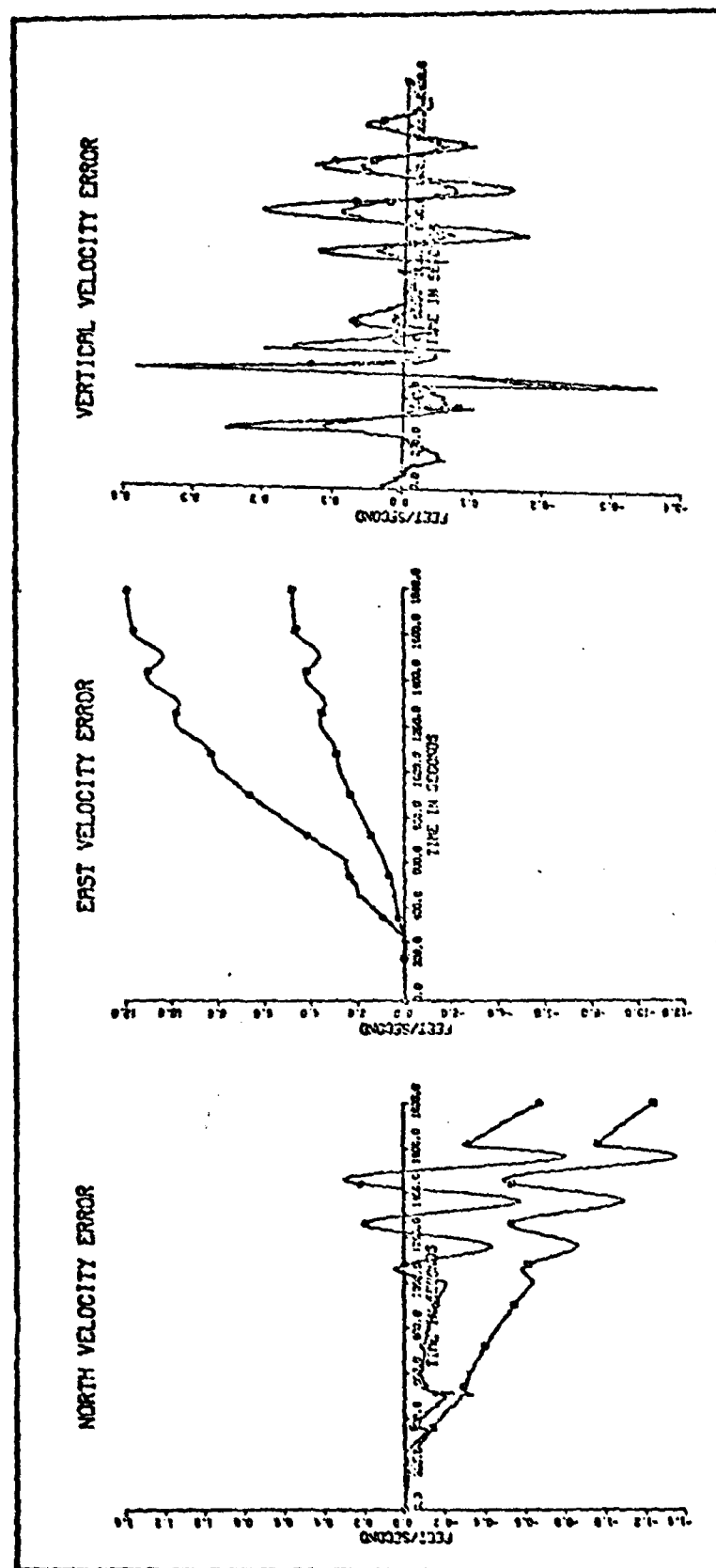


Figure 6b. Comparison of Velocity Error Time Histories with only Gyro Errors Present

- Represents results obtained using ring-laser gyro.
- Represents results obtained using two-degree-of-freedom gyro.

THIS PAGE IS CONTAINING CLASSIFIED INFORMATION

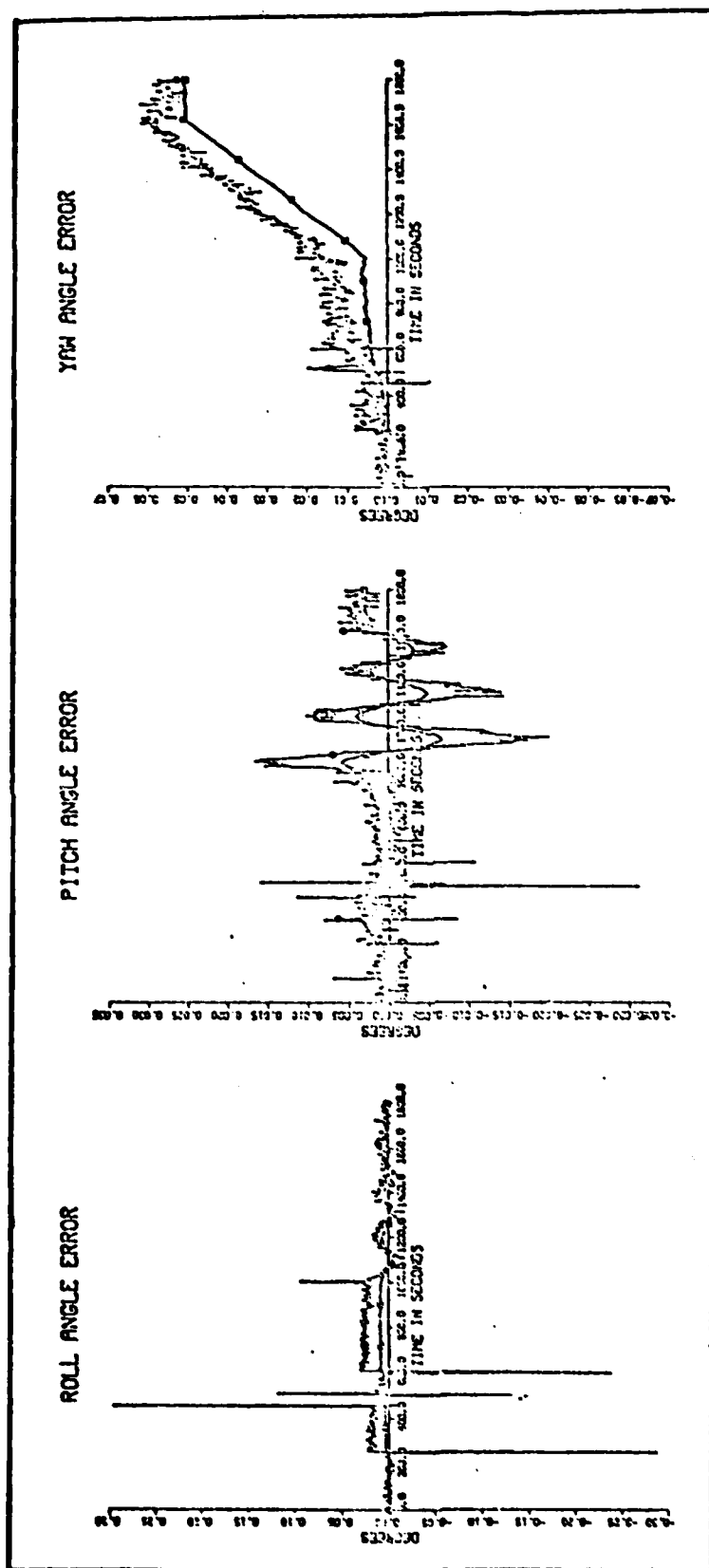


Figure 6c. Comparison of Attitude Error Time Histories with only Gyro Errors Present

- Represents results obtained using ring-laser gyro.
- Represents results obtained using two-degree-of-freedom gyro.

Flight Profile

As is eluded to in the introduction, part of the errors in a strapped-down INS result from the high dynamic environment that the sensors are subjected to when the navigation system is used on a fighter-type aircraft. Time histories for the INS errors in position velocity and attitude are generated using the strapped-down INS simulations so that the effects of the high dynamic environment can be assessed. Therefore, a flight profile containing several maneuvers typical of a tactical aircraft mission is chosen. Figure 7 shows the flight profile implemented for this work. The initial start of the simulation assumes that the aircraft is in straight and level flight at a cruise speed of mach .5 at an altitude of 5000 feet, and a heading of north. At 100 seconds into the simulation, the aircraft descends to 500 feet while increasing its velocity to mach .75. After completion of the descent, the aircraft performs a snap roll. Following the roll, at about 360 seconds into the flight, a weapon delivery is simulated. This maneuver consists of a dive at a 12.5 degree angle followed by a 3.5g pull-up. After a leveling off from the weapon delivery, the aircraft performs another snap roll followed by an evasive maneuver. The evasive maneuver consists of a climb at a flight path angle of 20° with a bank of 45° to the right for seven seconds followed by a bank to the left of 45° for seven seconds, leveling off at an altitude of 5000 feet and a speed of mach .75. Upon

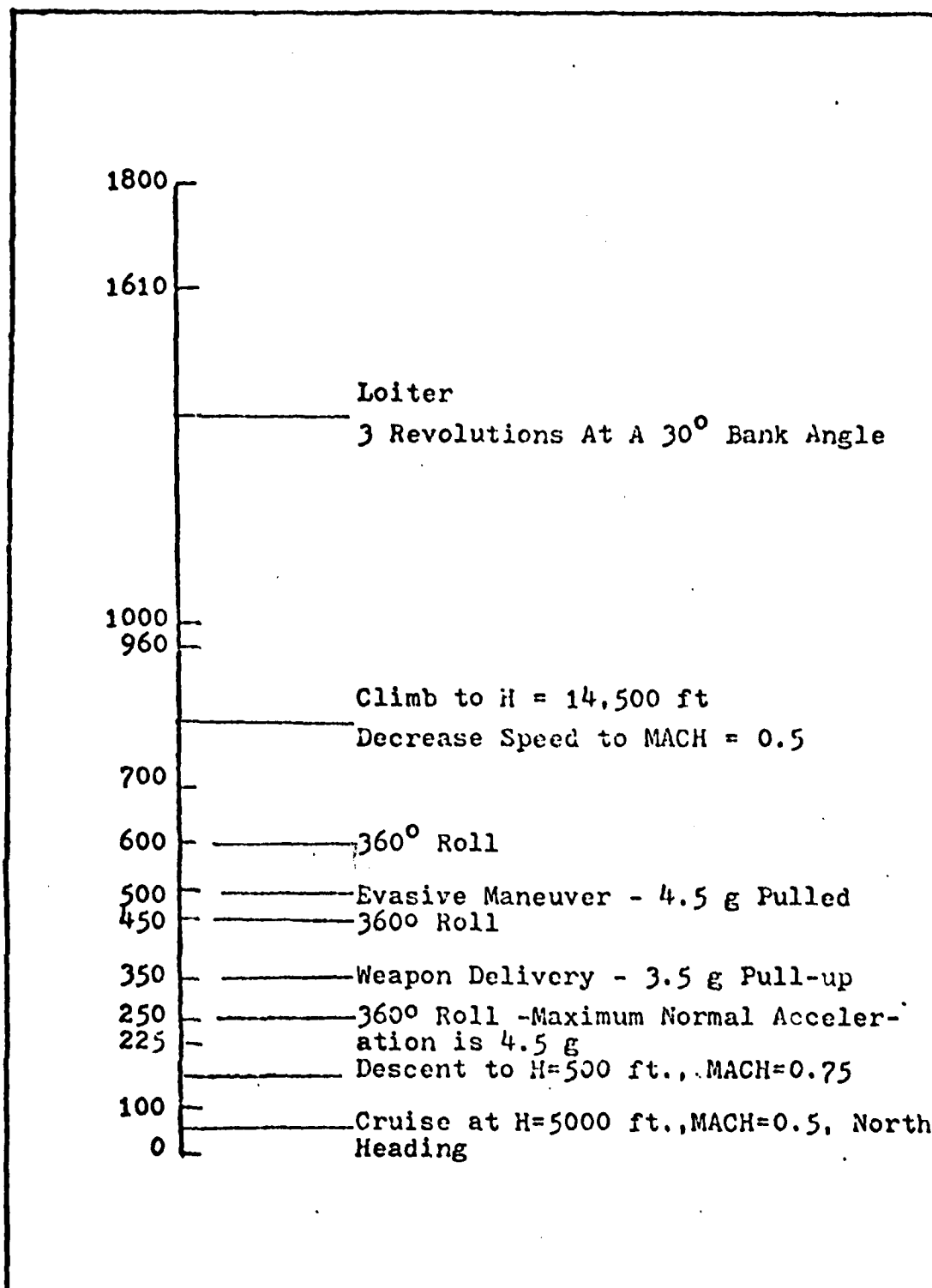


Figure 7. Description of Flight Profile (Ref 4:1173)

leveling off at 5000 feet, the aircraft performs a third snap roll followed by a climb to 14,500 feet during which its speed is decreased to mach .5. The final maneuver simulated is a loiter. During this phase of the flight, the aircraft turns through three revolutions at a 30° bank before returning to straight and level flight on a north heading. This maneuver is completed at about the 1620 second time point. The aircraft then maintains straight and level flight for the remainder of the flight time (Ref 4: 133-135).

Summary

This chapter has provided a description of the models implemented and assumptions made in using the strapped-down simulation to obtain the INS error time histories used in the deterministic error analysis that is to follow. This is not meant as a complete description of the strapped-down simulation and does not reflect the full capabilities of this computer simulation.

CHAPTER III

Effects of the Sensor Errors and Structural Modes on the INS Errors

This chapter presents a deterministic evaluation of the effects the sensor errors have on the errors of the strapped-down INS. Time histories of the INS errors in attitude, velocity, and position are obtained using the strapped-down INS simulation. The simulations are made for the case with each sensor error source isolated as well as for the cases where all sensor errors and no sensor errors are present. In these cases, structural modes are not sensed. An additional simulation is used to illustrate the effects of structural modes. The flight profile and sensor parameters given in the previous chapter are used in the generation of these error time histories. The analysis and comparison of these error time histories are presented in three major sections: effects of laser gyro errors, effects of accelerometer errors, and effects of structural modes. For the sections on sensor error effects, a general overview of the error time history obtained with all errors present will be presented, followed by a breakdown of the effects of the individual sensor error sources. Following these sections, the effects of the structural modes will be considered. A basis for the evaluation of the performance

of the INS, when structural modes are not sensed, is set at ≤ 3 ft/sec velocity error and ≤ 1 nm/hr position error.

Also, in analyzing the simulation results, use is made of the error state equations for a local vertical platform for confirming the results.

Effects of Laser Gyro Errors

Figure 8 shows the time history obtained for the laser gyro with all errors present. The roll and pitch Euler angle errors and the east and north velocity errors as well as the longitude and latitude errors are low frequency sinusoids with transients due to the maneuvers superimposed upon them. The yaw angle error is ramp-like in nature while the vertical channel errors, altitude and vertical velocity, are relatively unaffected by the sensor errors. The reason for the vertical channel being indifferent to sensor errors is because it is stabilized with a third order damping system. The aircraft maneuvers generally result in the Euler angles experiencing step or pulsed transients. The local level velocity errors are effected by the integration of the effect of the pitch and roll angle errors on the acceleration vectors. This effect results in the velocity errors experiencing steps or ramps. These same effects were passed on into the position errors, but since the position errors are effected by the integration of the velocity errors, the effects are more benign. The position errors then couple back to effect the roll and pitch angle errors. Since the position errors

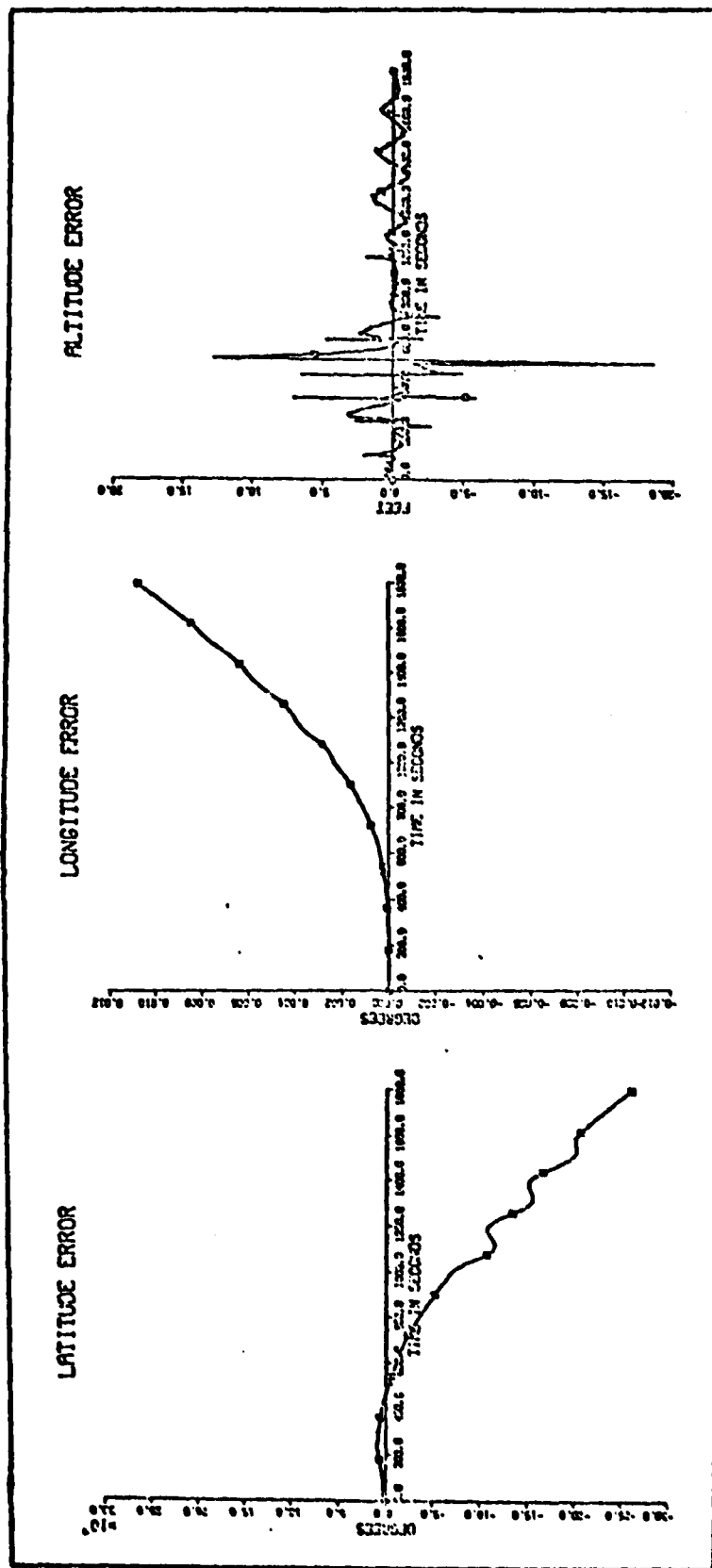


Figure 8a. Simulation Results Obtained with no Structural Modes, Ideal Accelerometer, and all Laser Gyro Errors Present (Position Errors)

THIS PAGE IS BEST QUALITY AVAILABLE
 GPO 1967 O-350-100-100

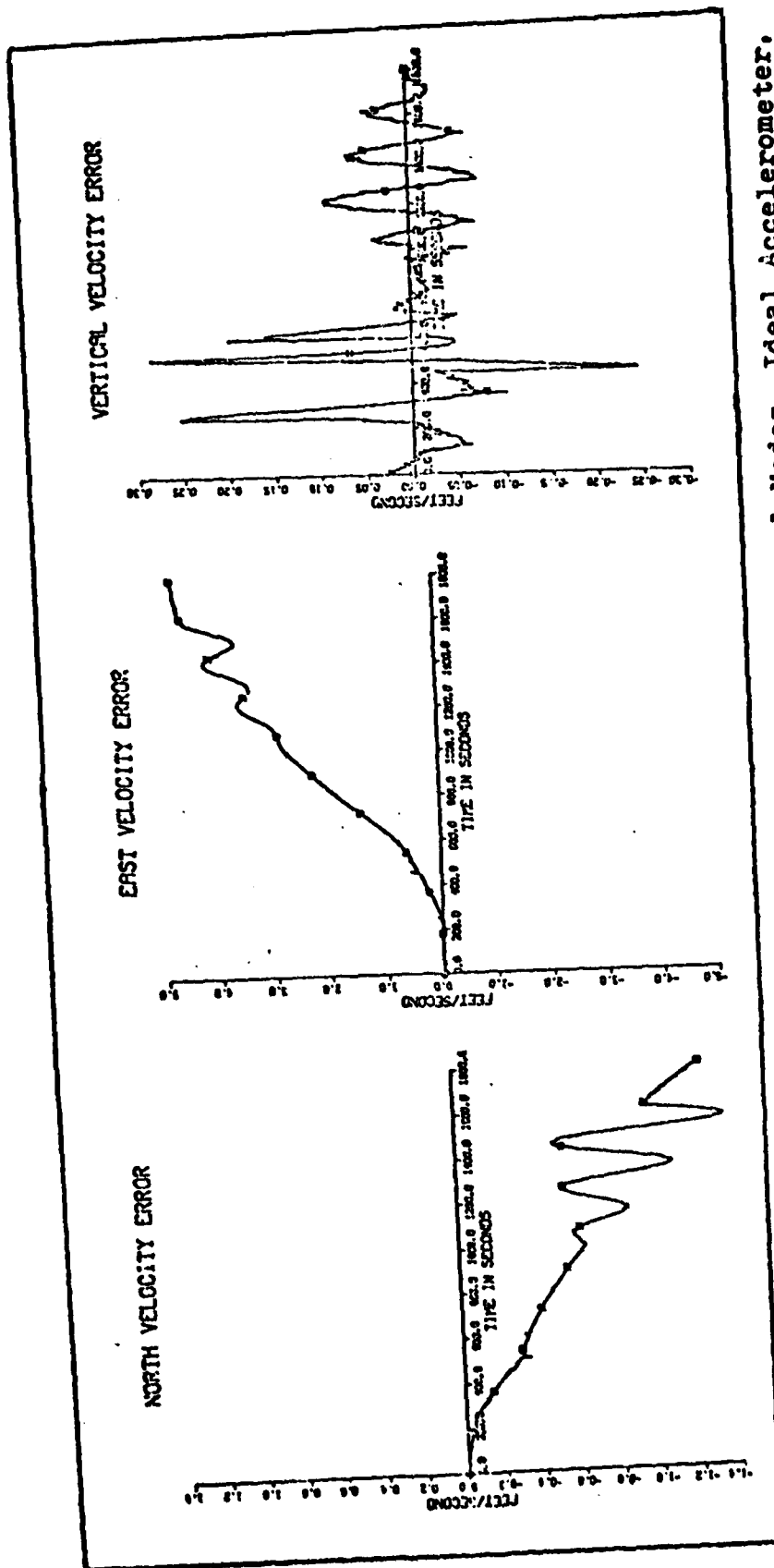


Figure 8b. Simulation Results Obtained with no Structural Modes, Ideal Accelerometer, and all Gyro Errors Present (Velocity Errors)

THIS PAGE IS BEST QUALITY PRINTING

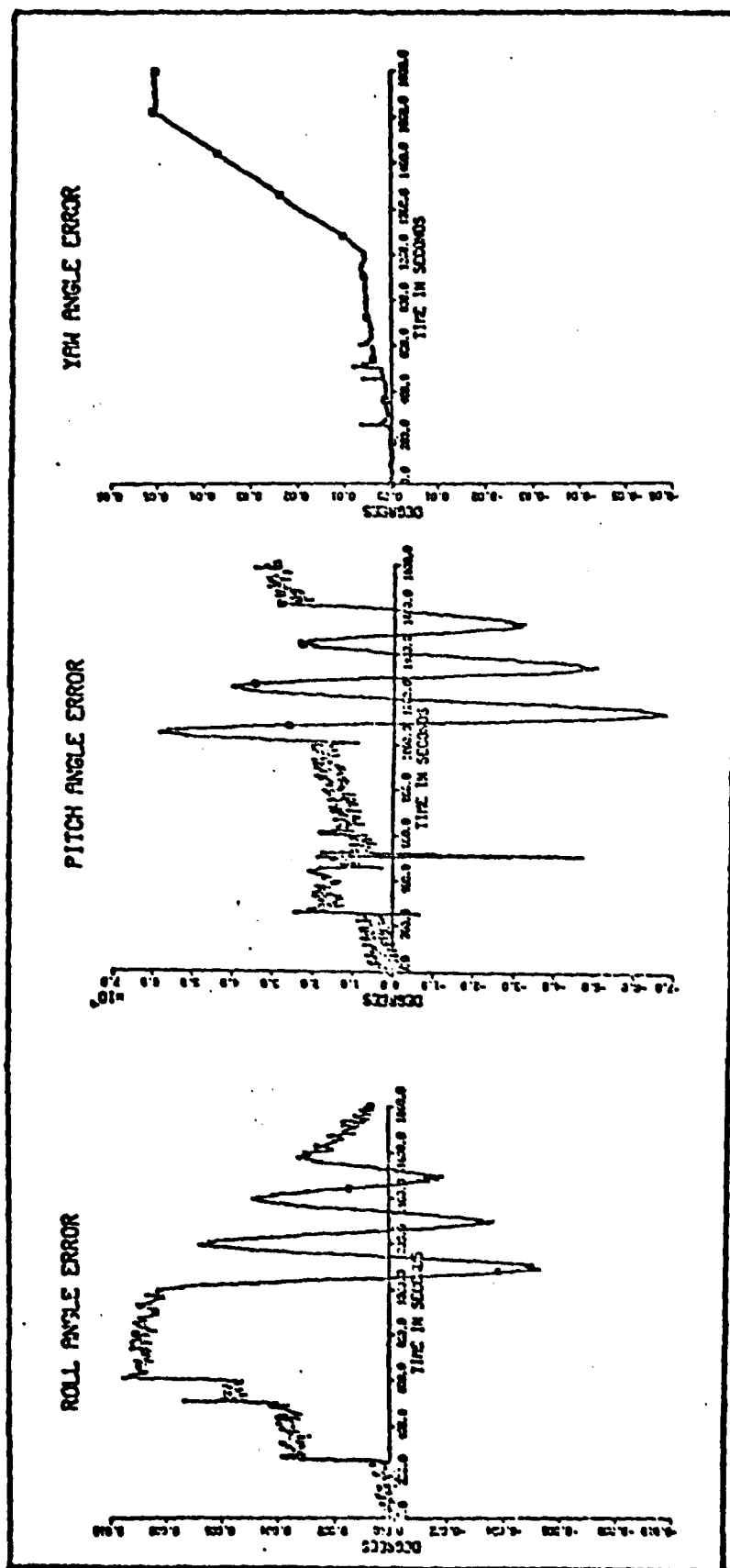


Figure 8c. Simulation Results Obtained with no Structural Modes, Ideal Accelerometer, and all Gyro Errors Present (Attitude Errors)

have little effect on the yaw angle error, it is ramp-like in nature. One of the most prominent effects of the maneuvers is that of the loiter. The loiter introduces a sinusoidal error into the navigation system variables.

The time histories shown in figure 8 are a composite of the effects of each individual sensor error. Each of these error sources is now considered separately to determine their individual effect on the INS errors.

Gyro Bias Error. Figure 9 shows the plots of the INS errors for simulations with only bias error present, all errors present, and no errors. The bias error plot is represented by the square, the plot of all errors by a triangle, and the case for ideal sensors is marked with a square.

The presence of the gyro bias error results in the Euler angles initially ramping off at the rate of the bias error ($0.01^{\circ}/\text{hr}$). The yaw angle error is only slightly effected by the aircraft maneuvers and, thus, it continues to ramp off at about $0.01^{\circ}/\text{hr}$. Before the loiter maneuver, the bias error accounts for about half of the total error, but during the loiter the bias error becomes negligible compared to the other gyro errors.

The snap rolls cause a step in the bias induced pitch angle error. Also, during the loiter maneuver, the amplitude of the oscillation of the pitch angle decreases more rapidly with all sensors present than with only the bias error present. This indicates that the bias error prolongs the settling of errors induced by the maneuvers of the

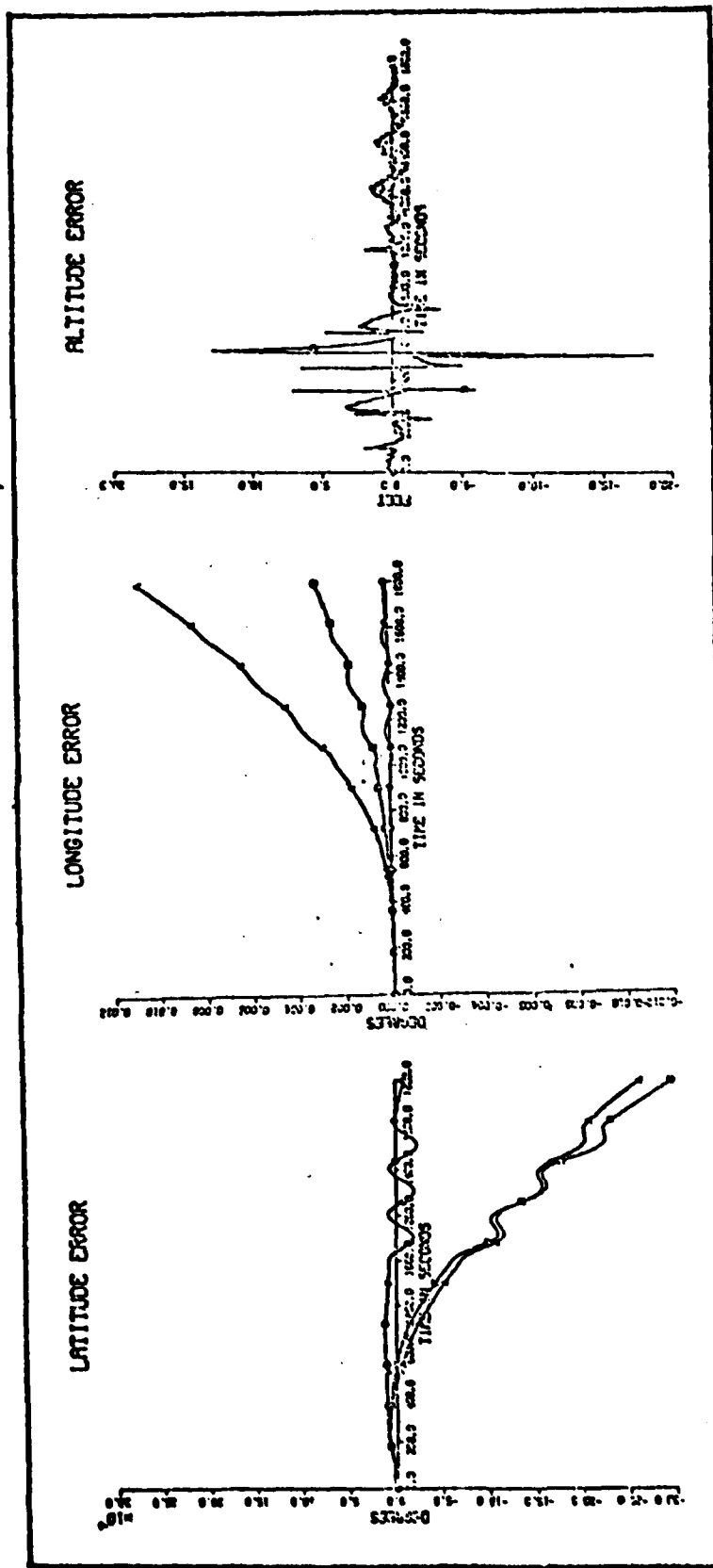


Figure 9a. Comparison of Position Error Time Histories with Laser Gyro Bias Error only, all Gyro Errors, and all Ideal Sensors

- Case with gyro bias error only.
- Case with ideal sensors.
- △ Case with all gyro errors.

THIS PLOT IS NOT TO BE USED FOR
ANALYSIS OF THE RESULTS OF THE
TESTS

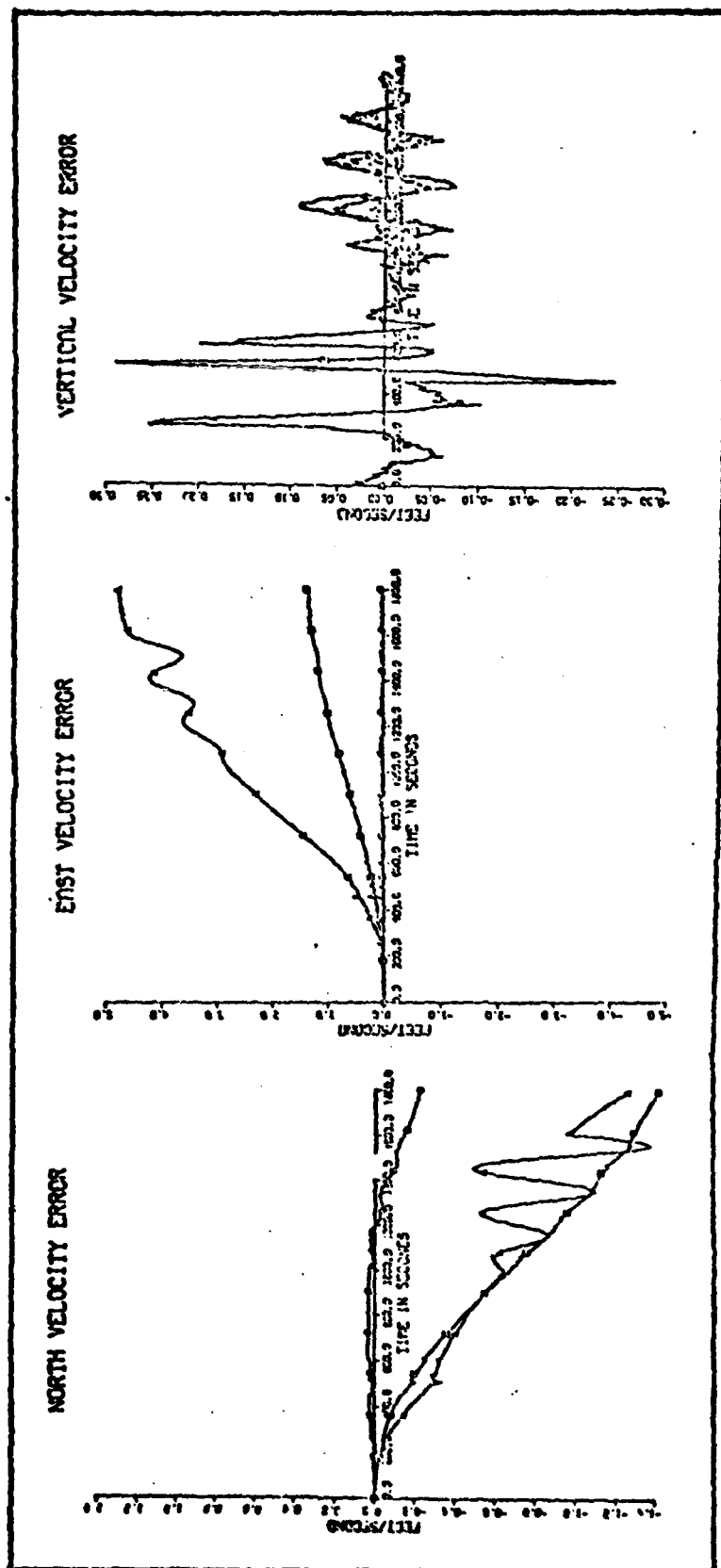


Figure 9b. Comparison of Velocity Error Time Histories with Laser Gyro Bias Error only, all Gyro Errors, and all Ideal Sensors

- Case with gyro bias error only.
- Case with ideal sensors.
- △ Case with all gyro errors.

Diagram 9b. Velocity Error Time Histories with Laser Gyro Bias Error only, all Gyro Errors, and all Ideal Sensors

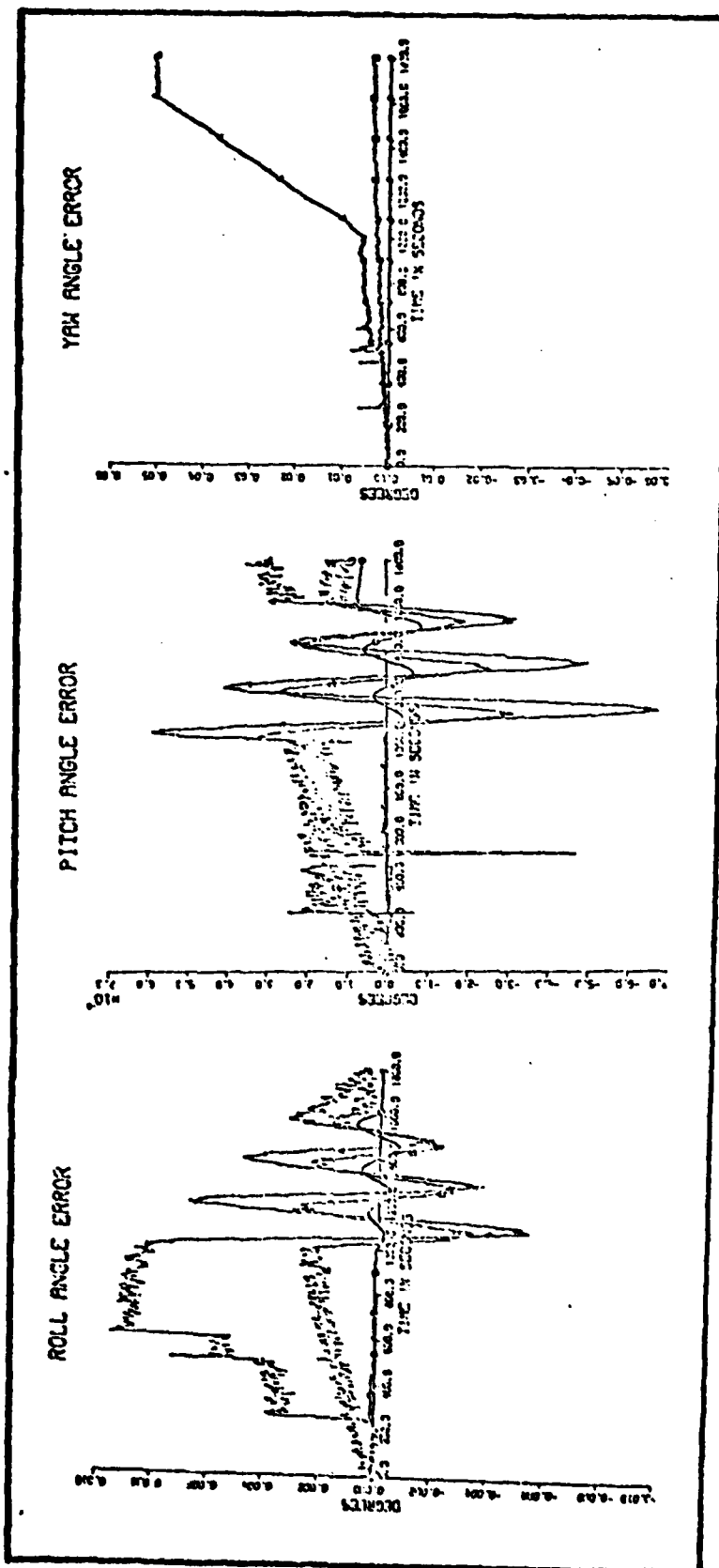


Figure 9c. Comparison of Attitude Error Time Histories with Laser Gyro Bias Error only, all Gyro Errors, and all Ideal Sensors

- Case with gyro bias error only.
- Case with ideal sensors.
- △ Case with all gyro errors.

aircraft. The bias error proves to be the primary driver of the pitch angle error. The bias error induces a ramp of $0.01^{\circ}/\text{hr}$ in the roll angle error that is only slightly altered by any aircraft maneuvers until the loiter maneuver is begun. During the loiter, as in the case of the pitch angle, the bias induced roll angle error tends to slow the settling of the error induced in the roll angle by the maneuvers. The bias error accounts for a large part of the roll angle error except during the phases of the flight where the snap rolls occur. Here, steps are introduced by other gyro errors and this causes the roll angle to become much larger when all gyro errors are present than when the bias alone is present. The east velocity error is largely influenced by the integration of the roll angle's effect on the vertical acceleration. This gives it a ramp-like nature with a slope of approximately $(3.5 \text{ ft/sec})/\text{hr}$. The steps are introduced into the roll angle when all sensor errors are present, resulting in a larger slope in the east velocity error with all gyro errors present than with only the bias error present. This indicates that the bias error is not the main contributor to the east velocity error. The effect of the bias error on the north velocity error is more pronounced. The bias error contributes a major portion of the north velocity error due to gyro errors. Also, the ramp induced in the north velocity error by the gyro bias is only slightly effected by the loiter maneuver and is larger than the error due to all gyro errors.

The position errors, latitude and longitude, are mainly driven by the integral of the velocity errors. Therefore, they too, exhibit a ramp-like nature. However, during the loiter there are more oscillations in the position errors, but this is not caused by the gyro errors because these oscillations are evident even when ideal sensors are used. As is expected, since position errors are largely influenced by the integration of the velocity errors, the bias error has a similar effect on the position errors as it does on the velocity errors.

Gyro Misalignment Error. The second gyro source examined is the misalignment error. Figure 10 shows the results of the simulations made with misalignment error only plotted against simulation results for the ideal gyro and for the laser gyro with all errors present. The most immediately noticeable effect of the misalignment error occurs in the yaw angle error at the points where the snap rolls are performed, but its most degrading effect occurs during the loiter. The misalignment error produces a rather steeply sloping yaw angle error that rises until the loiter is completed. Appreciable effects from the misalignment error are also found in the pitch and roll angle errors. Steps occur in these errors during the snap rolls and the evasive maneuvers.

However, the step in the pitch angle error during the second snap roll is in the opposite direction of the steps from the other snap rolls. This indicates that the pitch

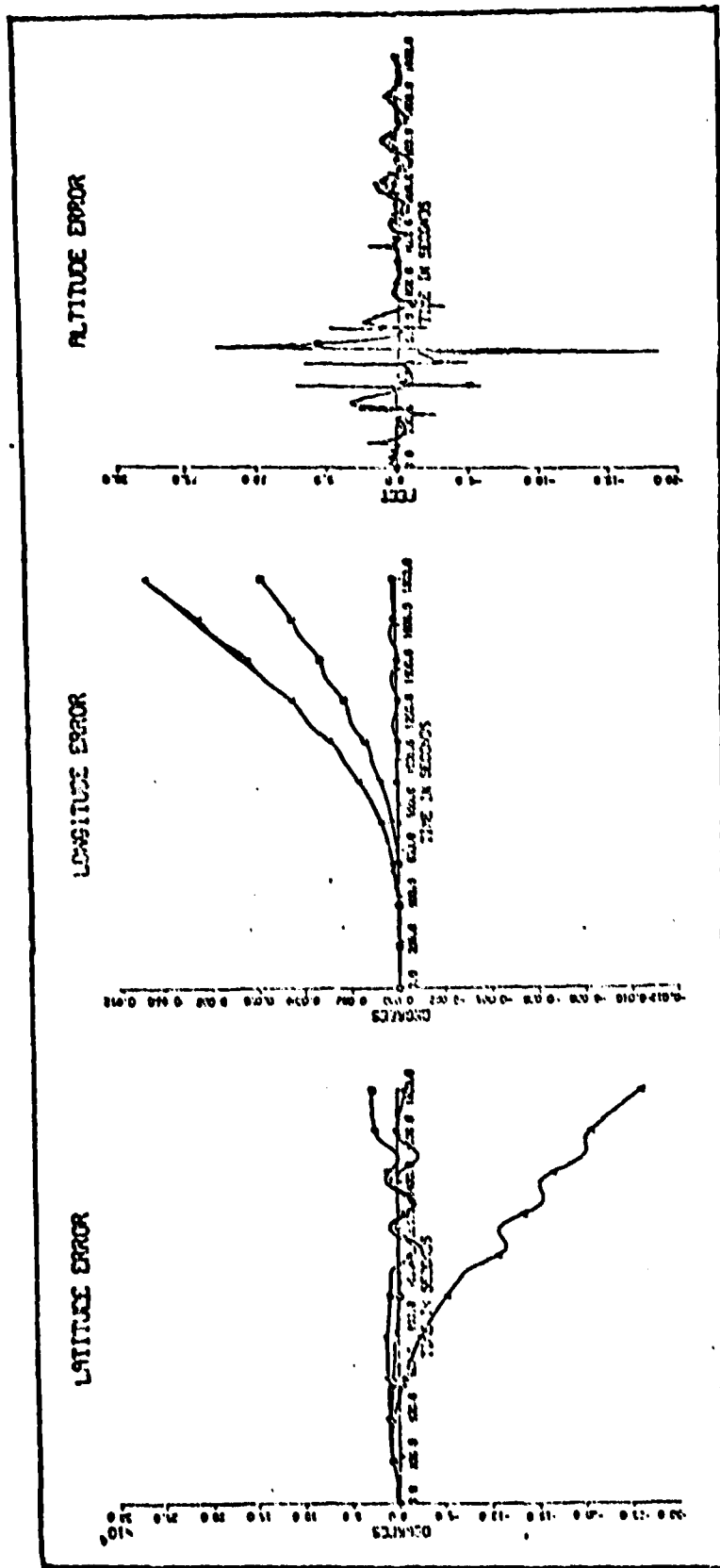


Figure 10a. Comparison of Position Errors for Case of Laser Gyro Misalignment Error only, all Gyro Errors, and Ideal Sensors

- Case with misalignment error only.
- Case with ideal sensors.
- △ Case with all gyro errors present.

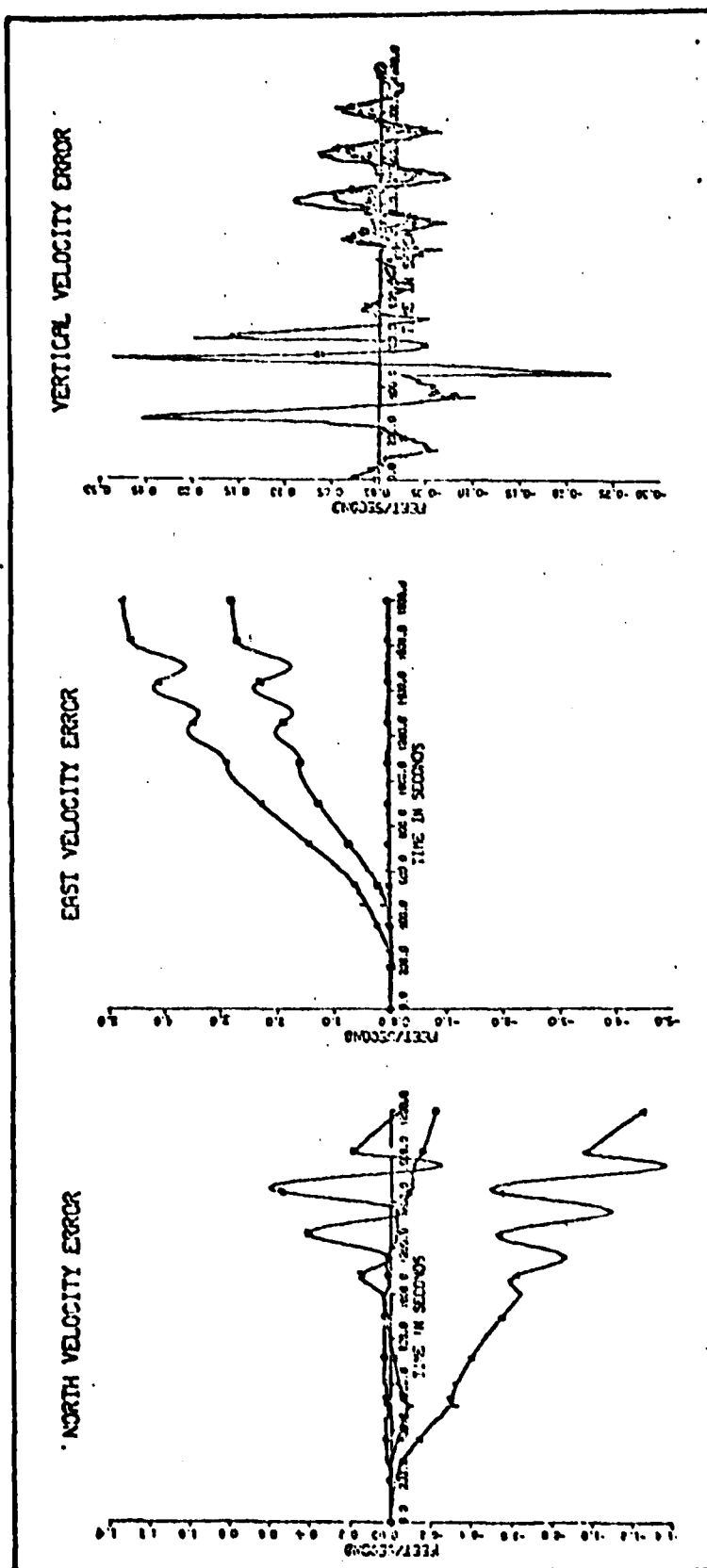


Figure 10b. Comparison of Velocity Errors for Case of Laser Gyro Misalignment Error only, all Gyro Errors, and Ideal Sensors

- Case with misalignment error only.
- Case with ideal sensors.
- △ Case with all gyro errors present.

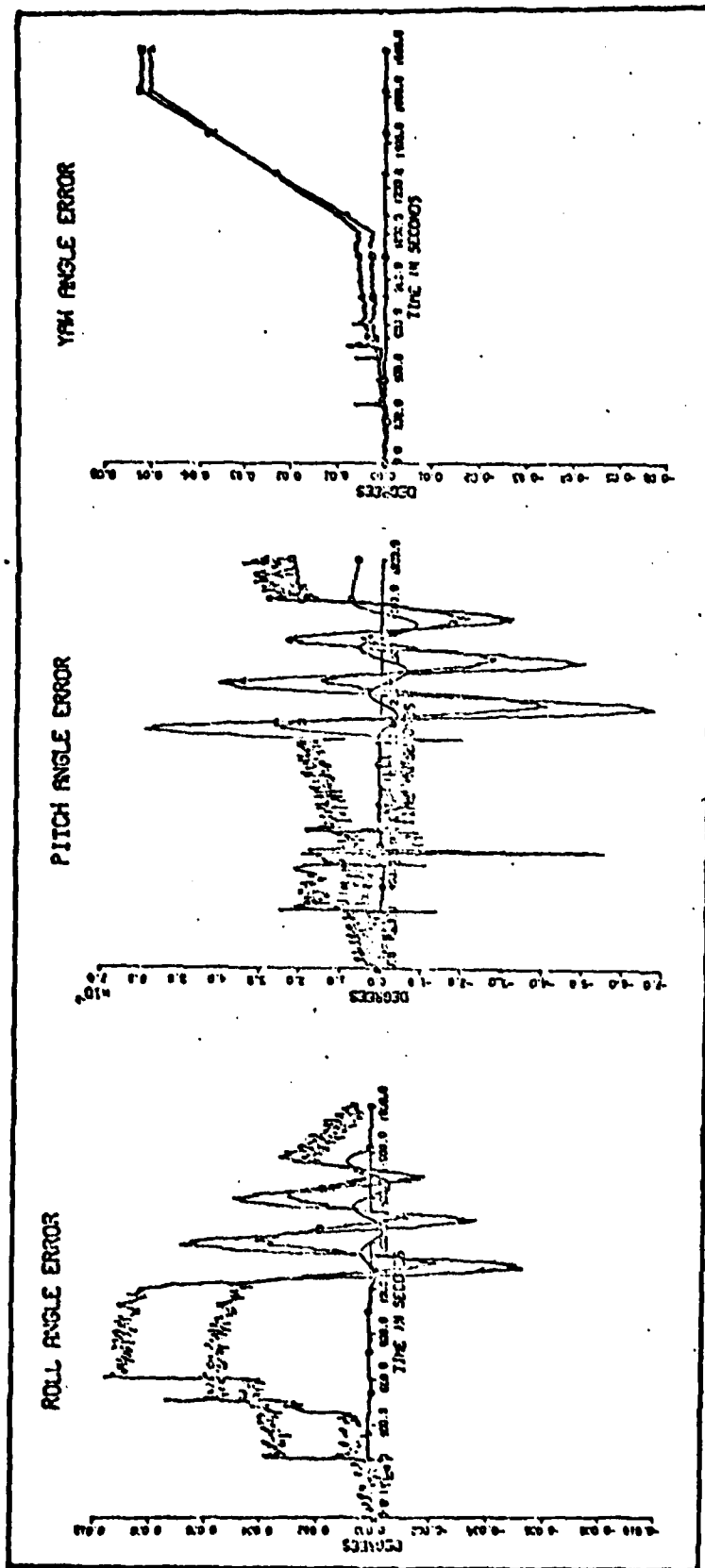


Figure 10c. Comparison of Attitude Errors for Case of Laser Gyro Misalignment Error only, all Gyro Errors, and Ideal Sensors

- Case with misalignment error only.
- Case with ideal sensors.
- △ Case with all gyro errors present.

angle is sensitive to roll direction, while the roll angle error has steps at each snap roll that are in the same direction. The misalignment error clearly makes up for a large portion of all of the Euler angle errors and during loiter it becomes even more dominant. The step errors in the roll and pitch angle errors are integrated and result in ramp errors in the east velocity error. This ramp error makes up for most of the difference that existed between the bias error induced east velocity error and that resulting from all of the gyro errors. This increased ramp effect is enough by itself to push the east velocity error to the three nautical mile error value. Therefore, reduction of the misalignment error is highly desirable for improving the INS performance. Because of the large yaw error and the relatively small pitch error, the north velocity error is only mildly effected by the misalignment error during most of the flight. (The coupling of the pitch angle to vertical acceleration tends to subtract from the coupling of the yaw error with the east acceleration). However, during the loiter, the misalignment error causes the north velocity error to oscillate as the aircraft turns through the three turns. Once again, since the position errors are largely effected by the integration of the velocity errors, the effects on them due to misalignment error are similar to those of the velocity errors.

Gyro Scale Factor Error. A third laser gyro error source considered in this analysis is the scale factor error. The error time histories obtained for it are shown

in Figure 11. The scale factor has less overall effect on the INS errors than either the bias or the misalignment errors. The most notable effect of the scale factor error is the steps it introduces in the roll angle error when the aircraft does a snap roll. Notice that the second roll creates a negative step error. This is because the second roll is made to the opposite direction of the others. The value of these steps is about 0.0019° . Since the second roll is done in the opposite direction of the others, the effect of the steps on the east velocity error and thus the longitude error caused by the scale factor is small compared to that caused by the misalignment error.

Gyro Random Walk Error. The plots obtained to illustrate the effects of the gyro random walk error on the INS performance are shown in Figure 12. The random walk error has little effect on the INS errors when compared with the effects of the misalignment, bias, and scale factor errors. The only noticeable effect the random walk error has is a step error in pitch angle during the evasive maneuver. This effect, however, does not cause any appreciable error in the velocity and position parameters. Therefore, the random walk error can be considered negligible when using the scale factor, bias, and misalignment errors specified.

Summary. Figure 13 shows the simulation results for the laser gyro with all errors present and with a 54 minute extension of level flight added to the flight profile. Adding this additional flight time allowed the illustration

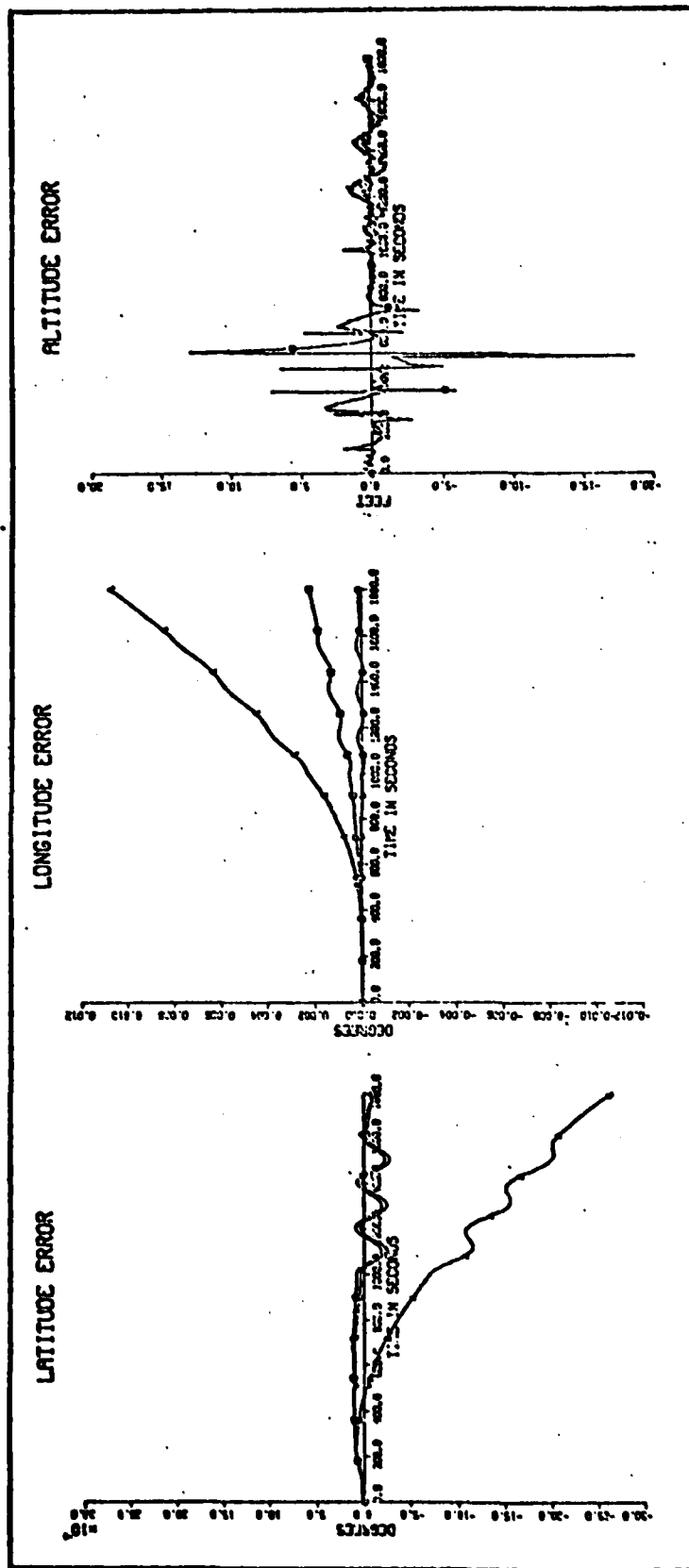


Figure 11a. Comparison of Position Errors for Case of Laser Gyro Scale Factor Error only, all Gyro Errors, and Ideal Sensors

- Case with gyro scale factor error only.
- Case with ideal sensors.
- △ Case with all gyro errors present.

THIS PAGE IS NOT QUALITY CONTROLLED
FROM COPY PROCESSED BY DDC

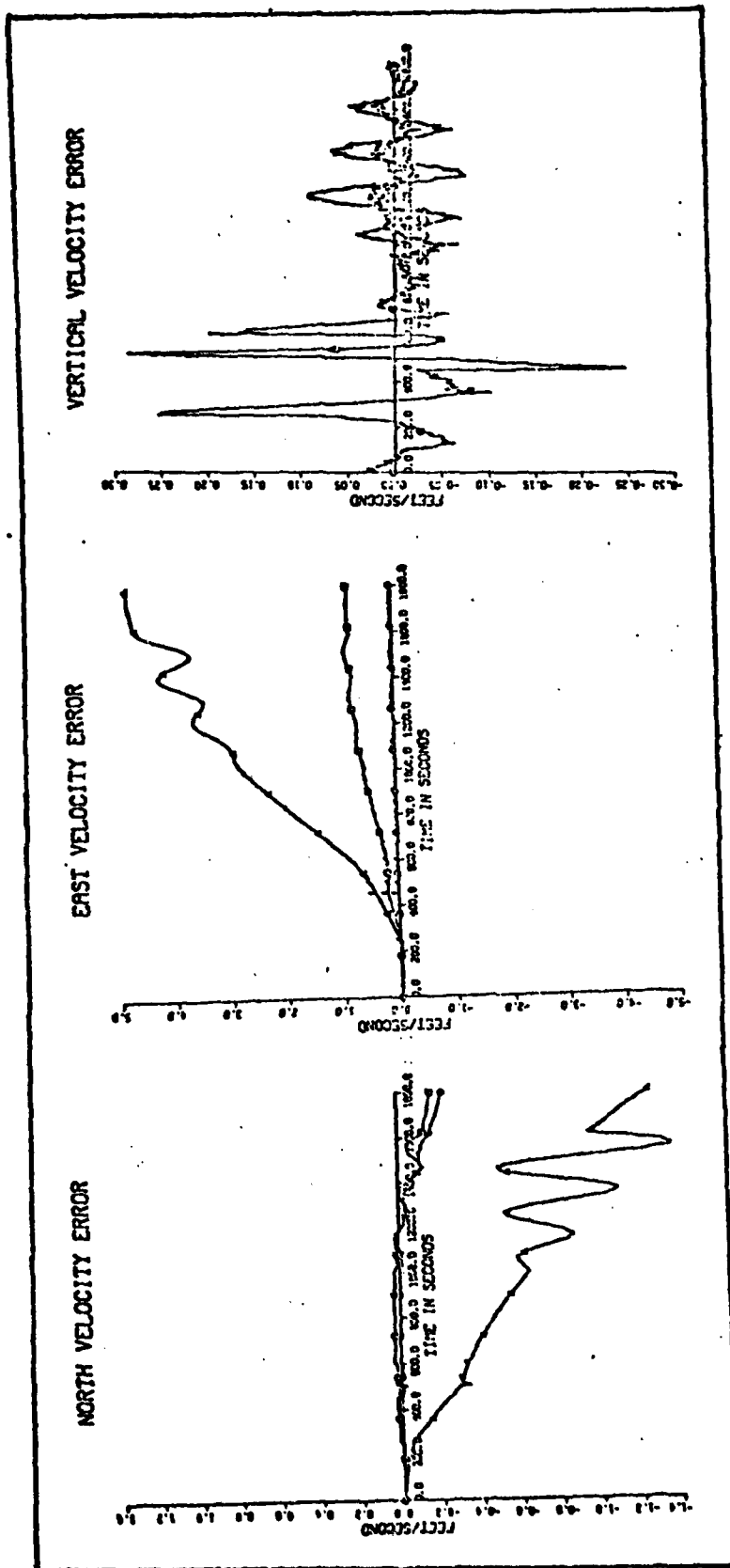


Figure 11b. Comparison of Velocity Errors for Case of Laser Gyro Scale Factor Error only, all Gyro Errors, and Ideal Sensors

- Case with gyro scale factor error only.
- Case with ideal sensors.
- △ Case with all gyro errors present.

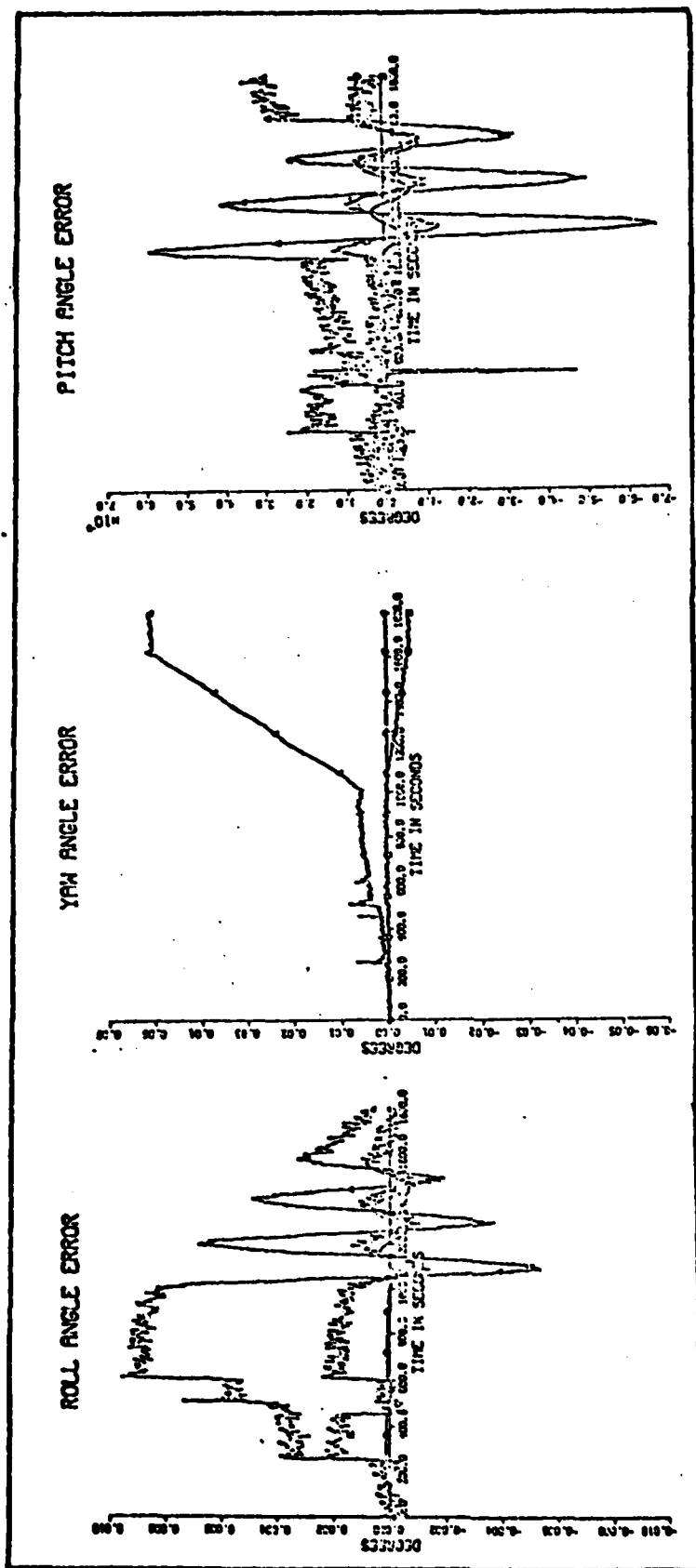


Figure 11c. Comparison of Attitude Errors for Case of Laser Gyro Scale Factor Error only, all Gyro Errors, and Ideal Sensors

- Case with gyro scale factor only.
- Case with ideal sensors.
- △ Case with all gyro errors present.

THIS DOCUMENT CONTAINS UNCLASSIFIED INFORMATION

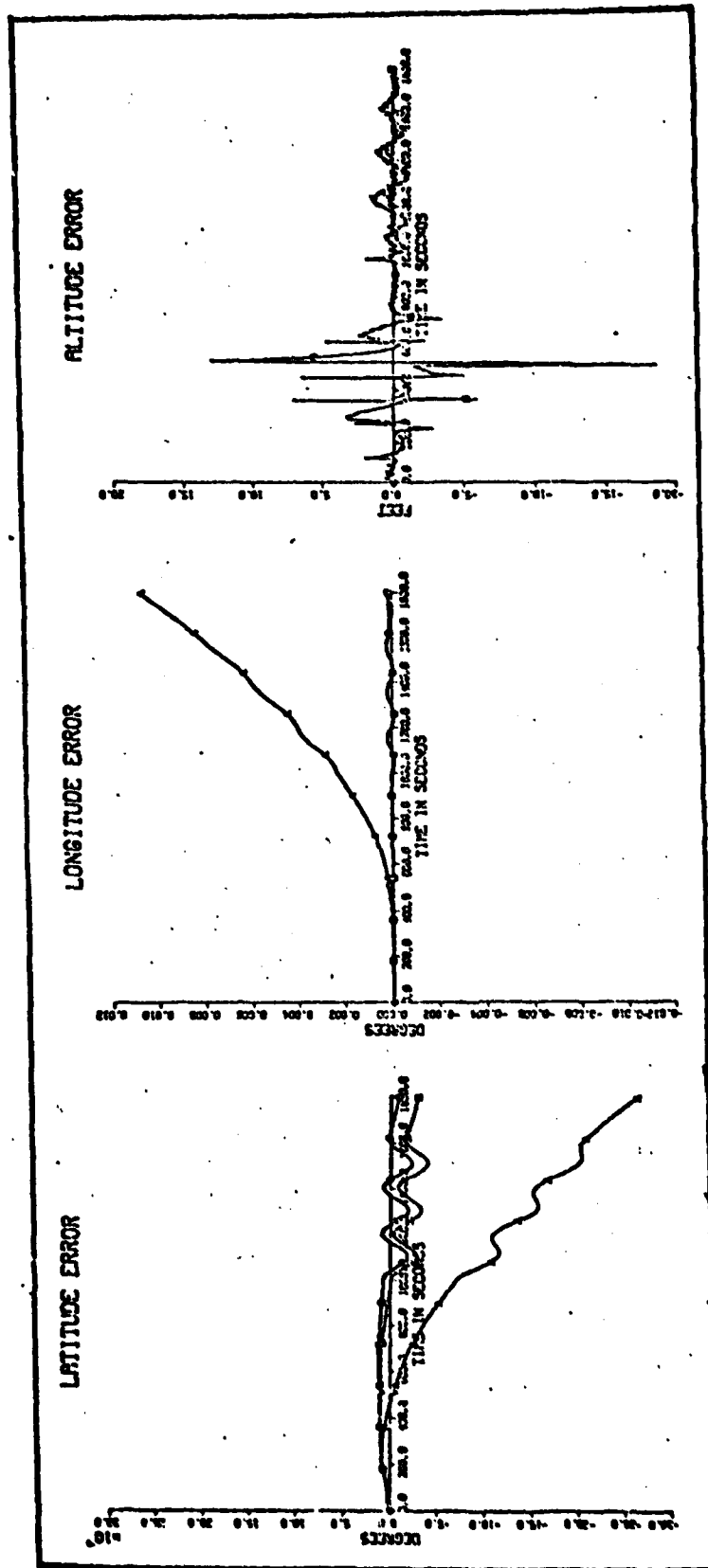


Figure 12a. Comparison of Position Errors for Case of Laser Gyro Random Walk Error only, all Gyro Errors, and Ideal Sensors

- Case with random walk error only.
- Case with ideal sensors.
- △ Case with all gyro errors present.

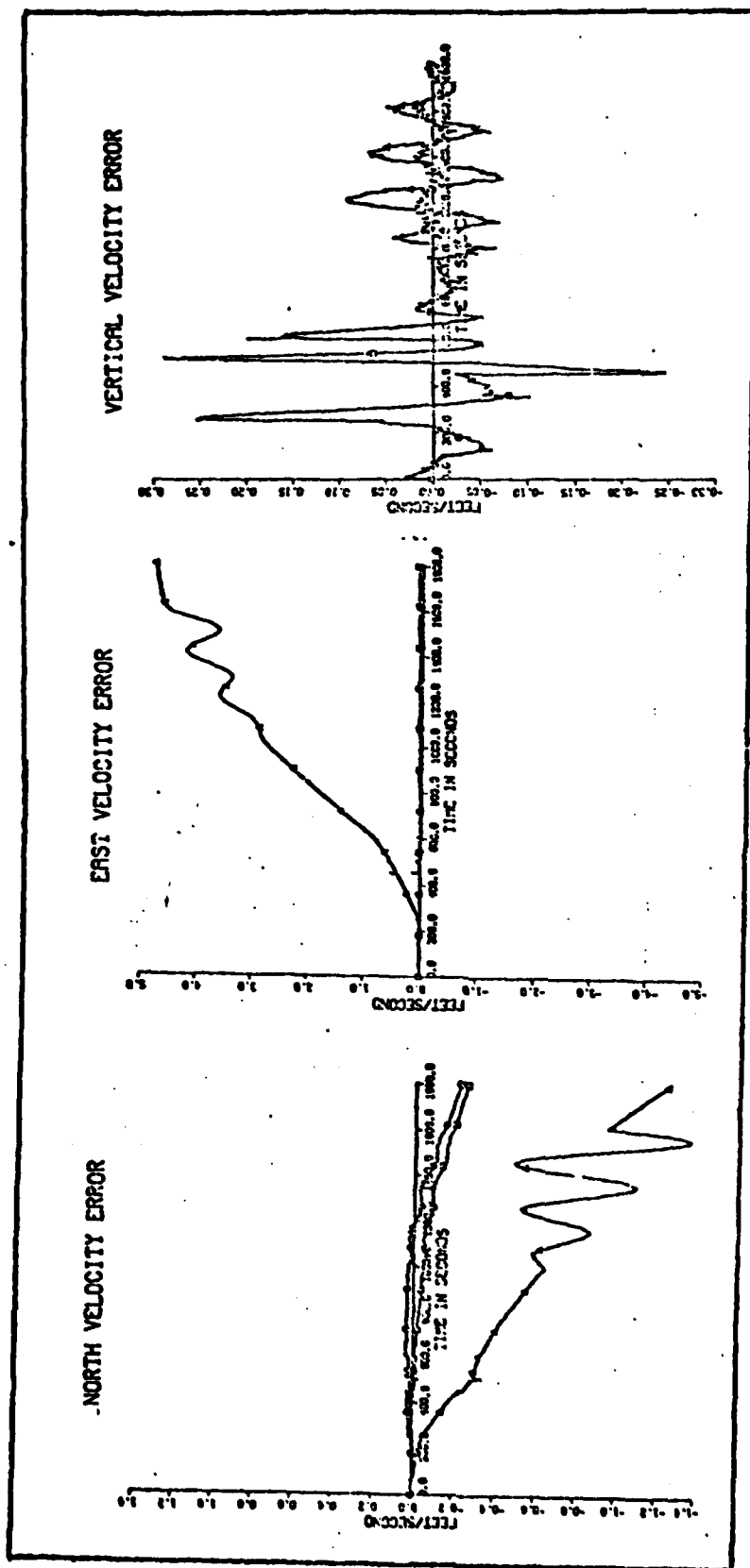


Figure 12b. Comparison of Velocity Errors for Case of Laser Gyro Random Walk Error only, all Gyro Errors, and Ideal Sensors

- Case with random walk error only.
- Case with ideal sensors.
- △ Case with all gyro errors present.

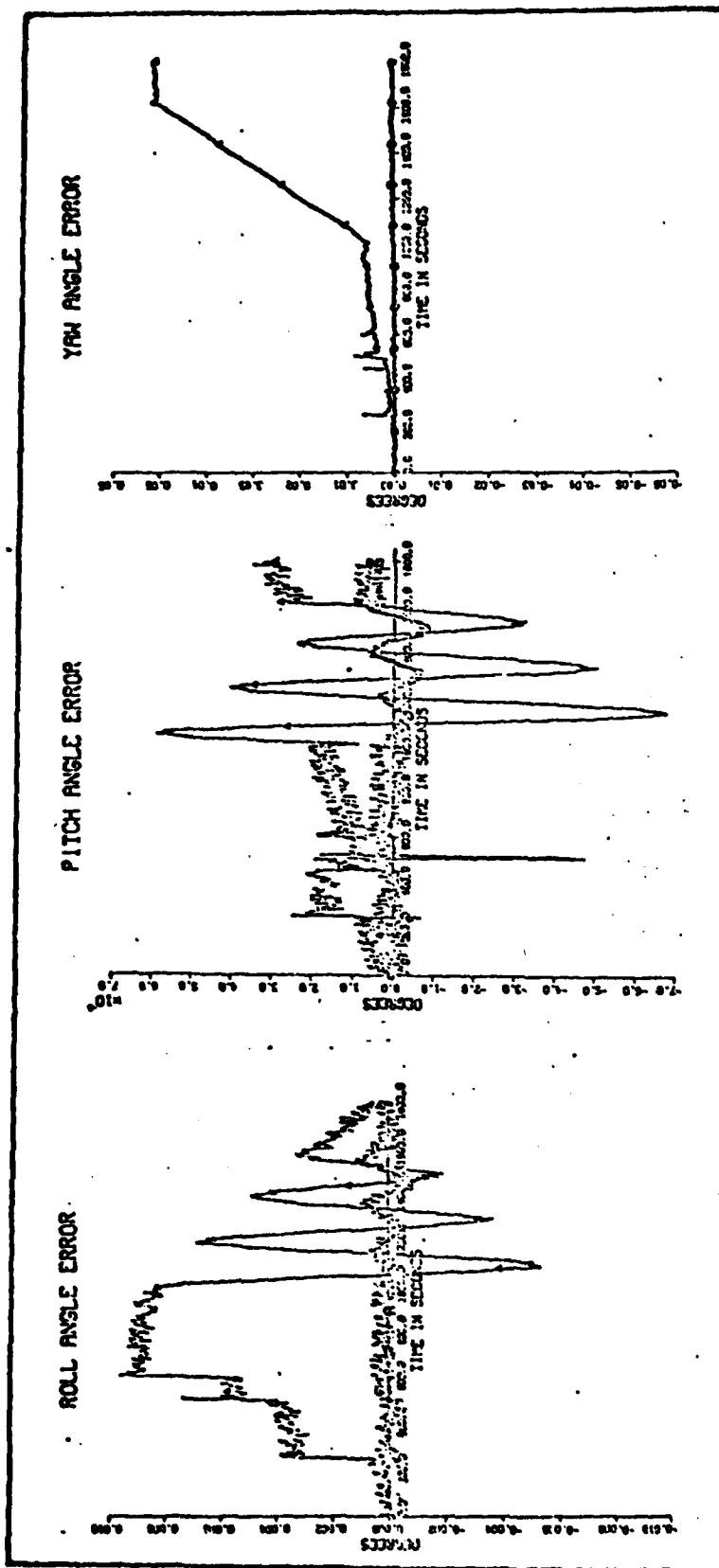


Figure 12c. Comparison of Attitude Errors for Case of Laser Gyro Random Walk Error only, all Gyro Errors, and Ideal Sensors

- Case with gyro random walk error only.
- Case with ideal sensors.
- △ Case with all gyro errors present.

of the errors after one Schuler period. Examining the yaw angle error, it is seen that upon completion of the maneuvers, the error ramps up with a slope equal to the bias error just as it did at the outset. The pitch and roll angle experience oscillations at the Schuler frequency. As is seen in the graphs, the amplitude of the Schuler frequency oscillation of the roll angle is smaller than the largest value of step errors that resulted from the high dynamic maneuvers. Likewise, the pitch angle error has a Schuler frequency amplitude that is smaller than the largest amplitudes of the oscillations created by the loiter. The implications of this are that the strapped-down system definitely experiences degradation in performance when subjected to a high dynamic environment.

The north velocity error is much closer to meeting the specifications than the east velocity error. Examination of the 84 minute simulation shows that the north velocity error reaches a peak at about one hour. The value at this point is -4 ft/sec. This results in a latitude error of 1 nm. Thus the latitude error is the only parameter that reaches the specifications and it is quite marginal.

The overall effect of the laser gyro errors indicates that improvements must be made before a performance specification of ≤ 3 ft/sec velocity error and ≤ 1 nm/hr position error can be achieved. The major problems are in east velocity error, and thus the longitude error. These error result

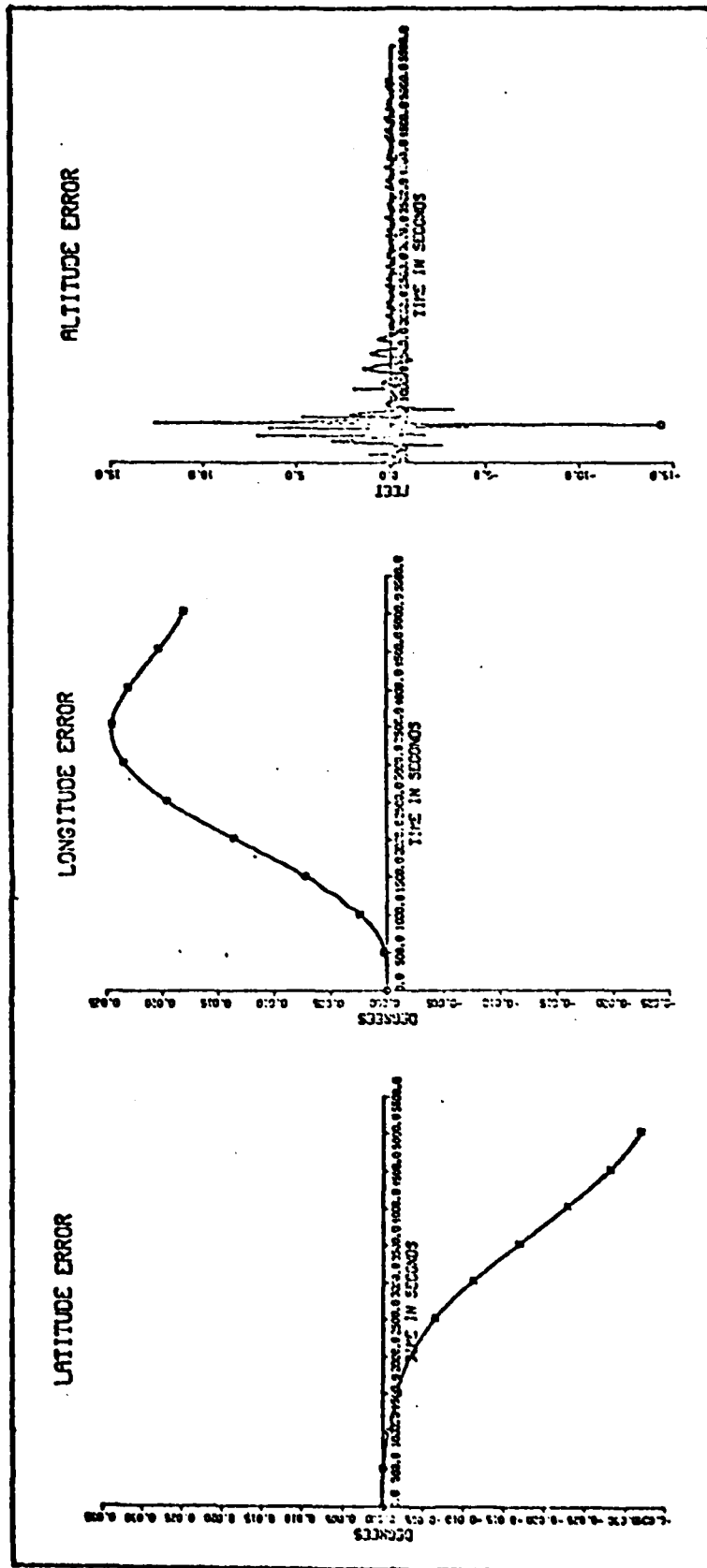


Figure 13a. Simulation Results Over one Schuler Period for Case of all Laser Gyro Errors (Position Errors)

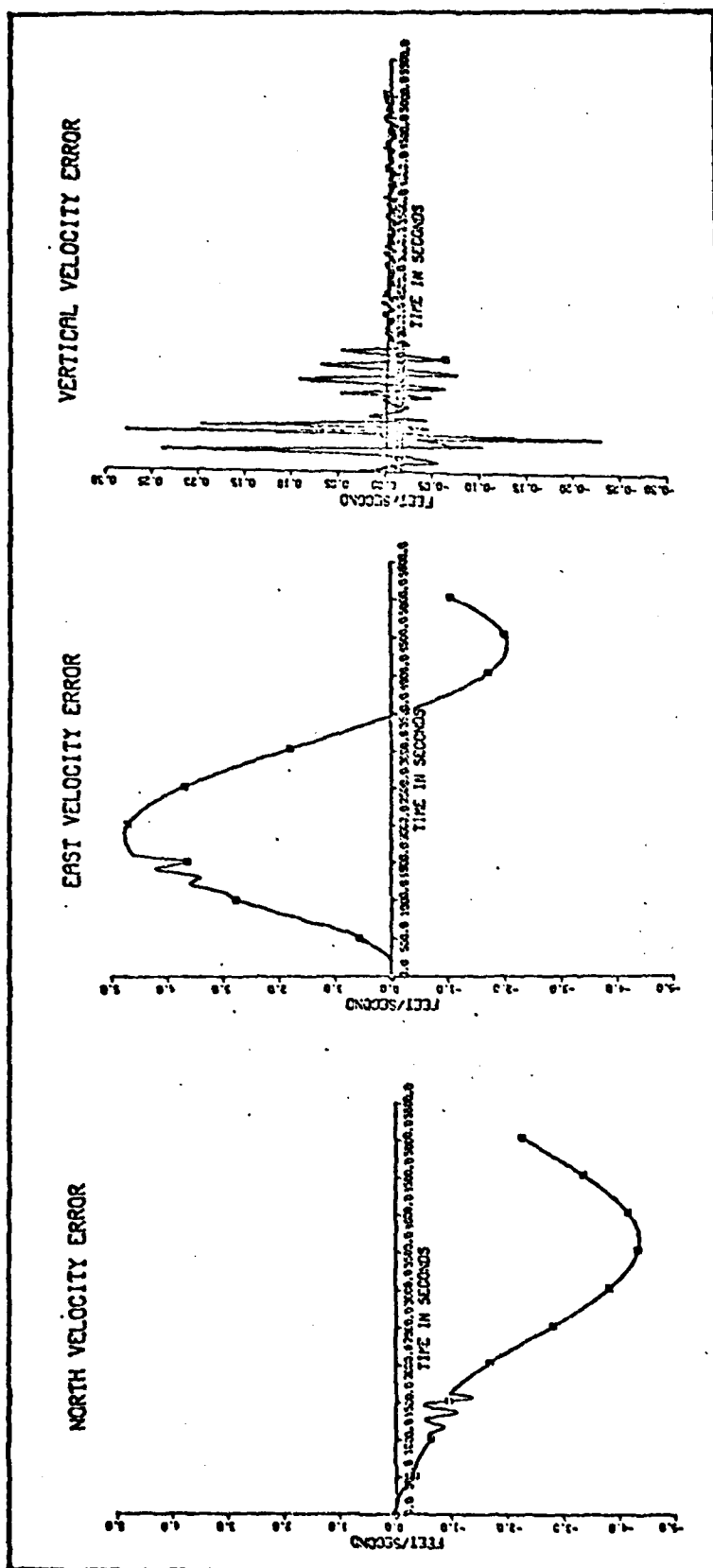


Figure 13b. Simulation Results Over one Schuler Period for Case of all Laser Gyro Errors (Velocity Errors)

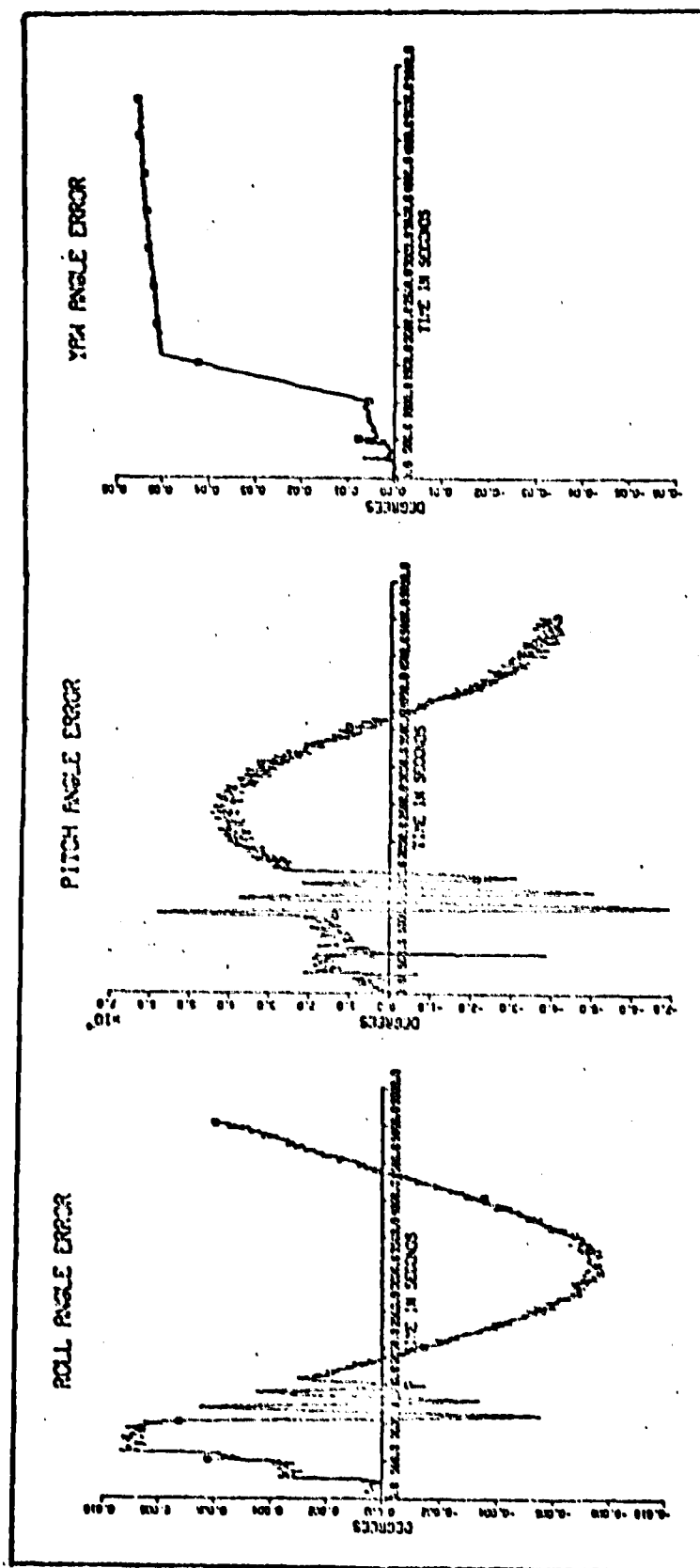


Figure 13c. Simulation Results Over one Schuler Period for Case of all Laser Gyro Errors (Attitude Errors)

from the large roll angle errors created primarily by the misalignment error, while the bias and scale factor error would have had about twice as much effect because the sign of the step errors in the roll angle caused by the scale factor error are dependent upon the direction of the rolls. Conversely, the step errors induced by the gyro misalignment error added regardless of the roll direction.

Effects of Quartz-Flexure Accelerometer Errors

A similar analysis to that presented on the laser gyro errors is now presented for the accelerometer errors. Figure 14 shows the error time histories generated for the quartz-flexure accelerometer with all error sources present. Unlike the gyro errors, the accelerometer errors produce errors in the velocity and thus position errors, which then couple back to effect the velocity errors. However, the loiter maneuver still has the same basic effect on the accelerometer error induced INS errors. That is, the INS errors oscillate as the aircraft performs the loiter maneuver.

The east velocity error tends to be relatively stable except for step errors from the snap rolls and evasive maneuver. It does oscillate during the loiter maneuver, but its mean remains fairly constant. The north velocity error, however, tended to be ramp-like and changed directions at the point of the start of the loiter maneuver. The position errors followed the general nature of the velocity

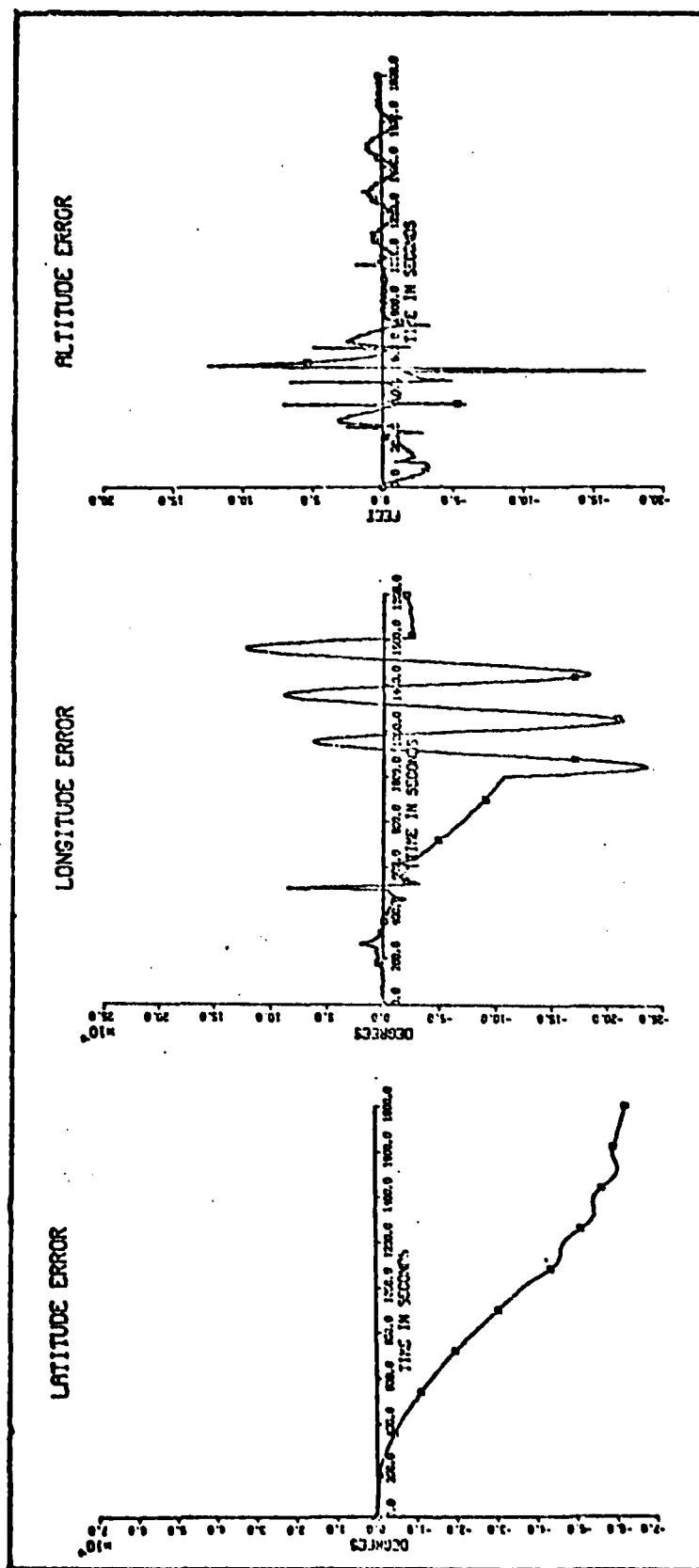


Figure 14a. Error Time Histories for Case of all Accelerometer Errors Present
(Position Errors)

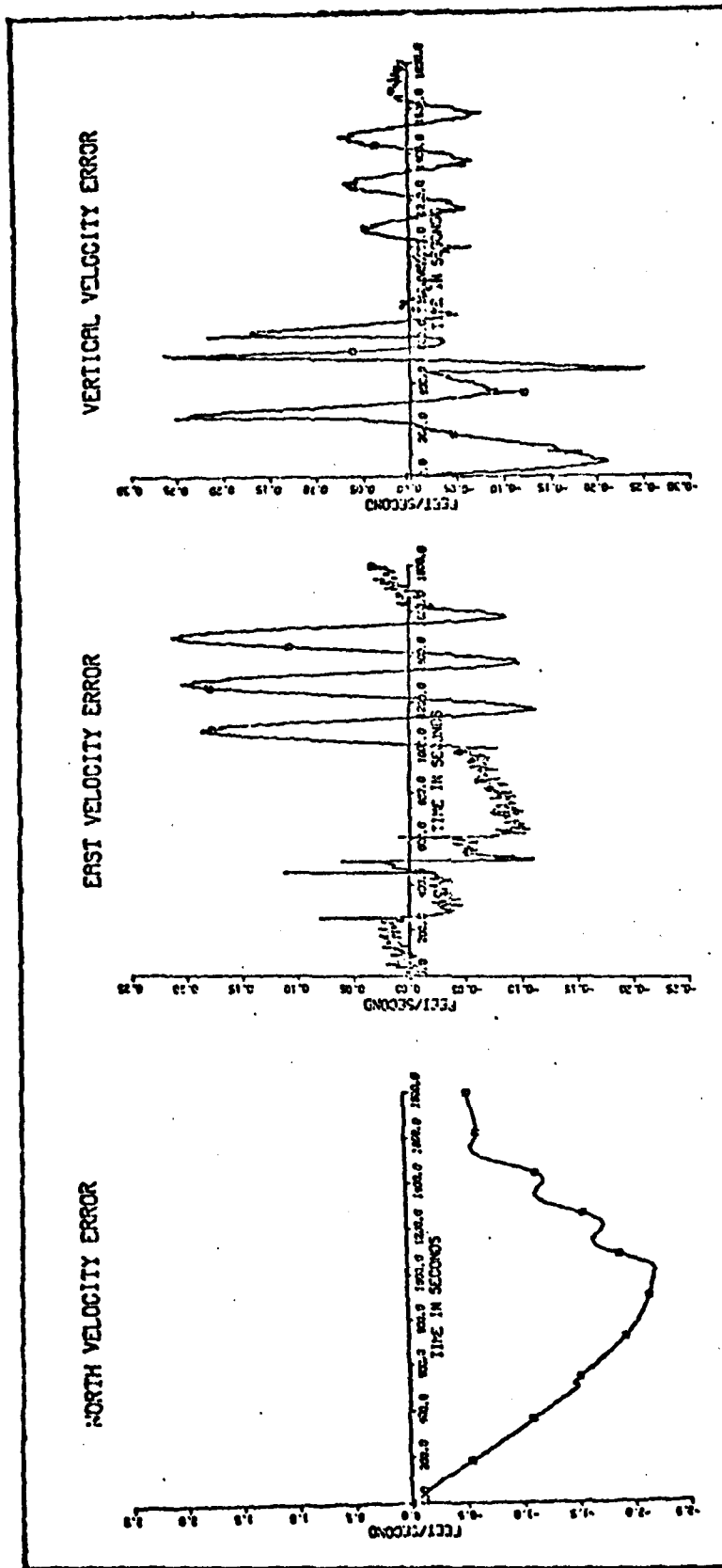


Figure 14b. Error Time Histories for Case of all Accelerometer Errors Present (Velocity Errors)

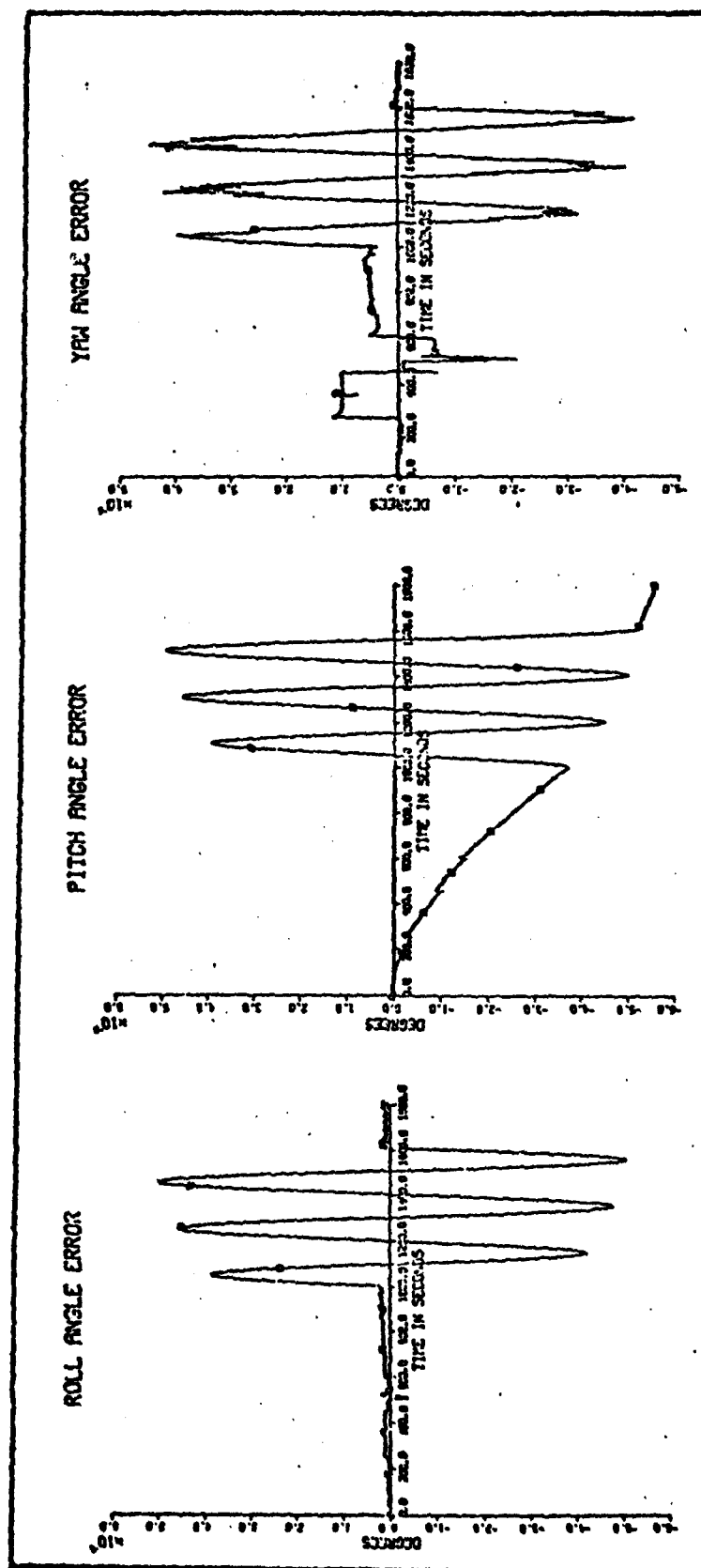


Figure 14c. Error Time Histories for Case of all Accelerometer Errors Present (Attitude Errors)

errors except that the latitude error did not change directions. The pitch angle error resembles the north velocity while the roll angle is of the same form as the east velocity error. The yaw angle error is relatively stable except for the steps induced by the snap rolls and evasive maneuver. As was the case of the gyro errors, accelerometer errors have little effect on the vertical channel. The effect of the individual accelerometer errors on INS performance is now assessed.

Accelerometer Bias Error. The bias error is the dominate accelerometer error source. Figure 15 shows the results of the simulation obtained with the bias as only accelerometer error. It produces a ramp in the east velocity error that is of a much larger magnitude than that for the case where all accelerometer errors are present. This results because the other accelerometer errors create east velocity errors that are of the opposite sign. Also, there is a sign change in the east velocity error at the beginning of the loiter. The longitude error follows the same general characteristics as the east velocity error except that it does not change signs. Small pulses are visible on the accelerometer bias error induced east velocity error at the points of the evasive maneuver and snap rolls. The pitch and roll angles both ramp off before oscillating as the loiter maneuver begins. The pitch angle is essentially the same as the north velocity error. The yaw angle error with bias error only, basically follows the

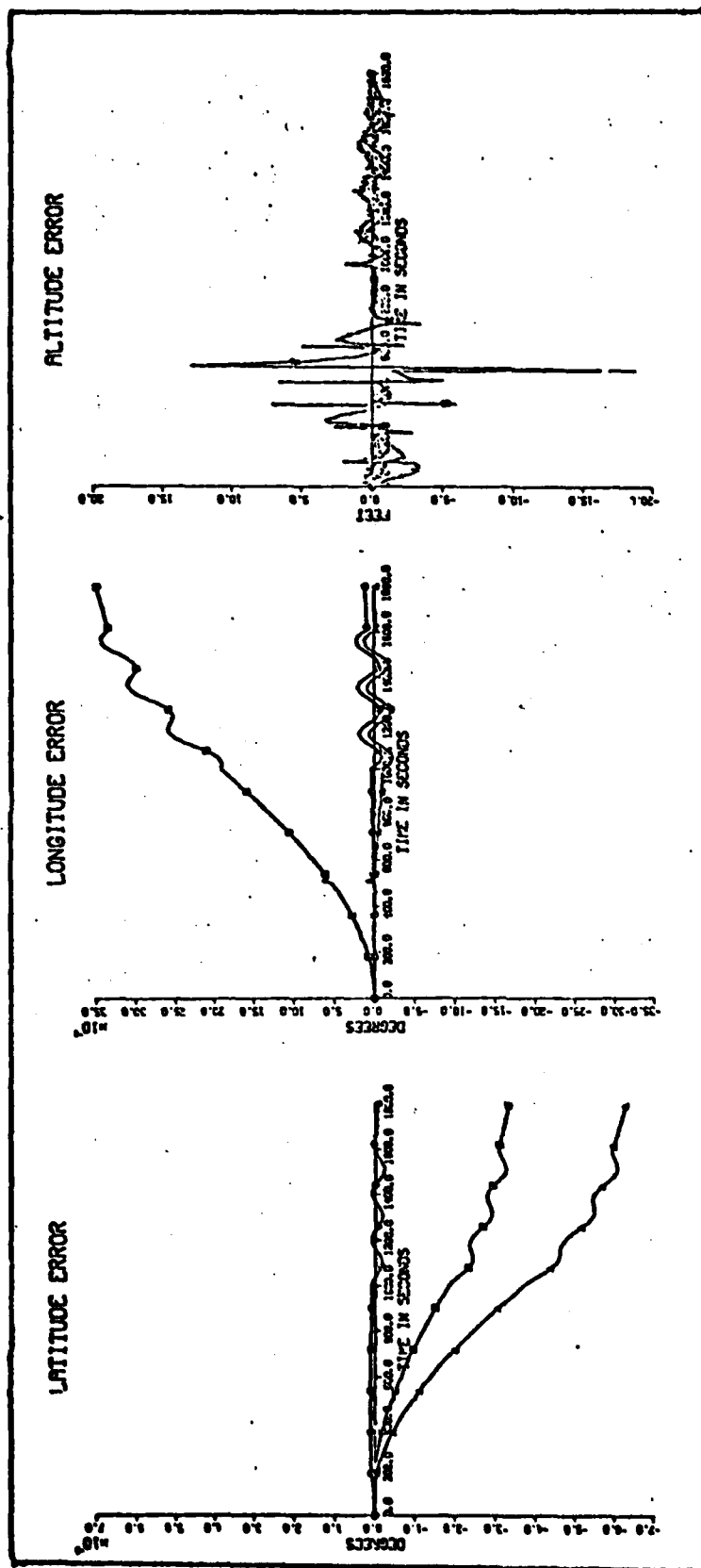


Figure 15a. Comparison of Position Errors for Case of Accelerometer Bias Error only.
all Accelerometer Errors, and Ideal Sensors

- Case with accelerometer bias error only.
- Case with ideal sensors.
- △ Case with all accelerometer errors present.

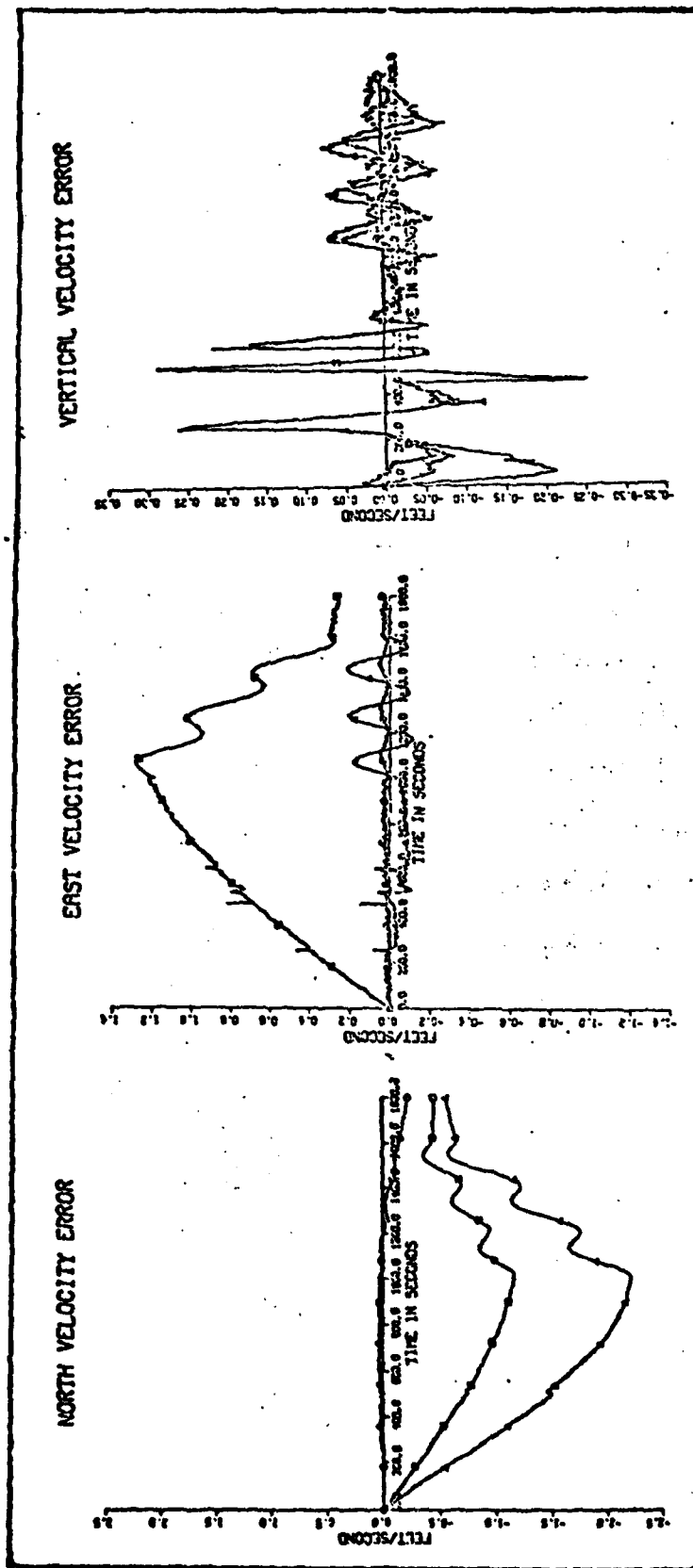


Figure 15b. Comparison of Velocity Errors for Case of Accelerometer Bias Error only, all Accelerometer Errors, and Ideal Sensors

- Case with accelerometer bias error only.
- Case with ideal sensors.
- △ Case with all accelerometer errors present.

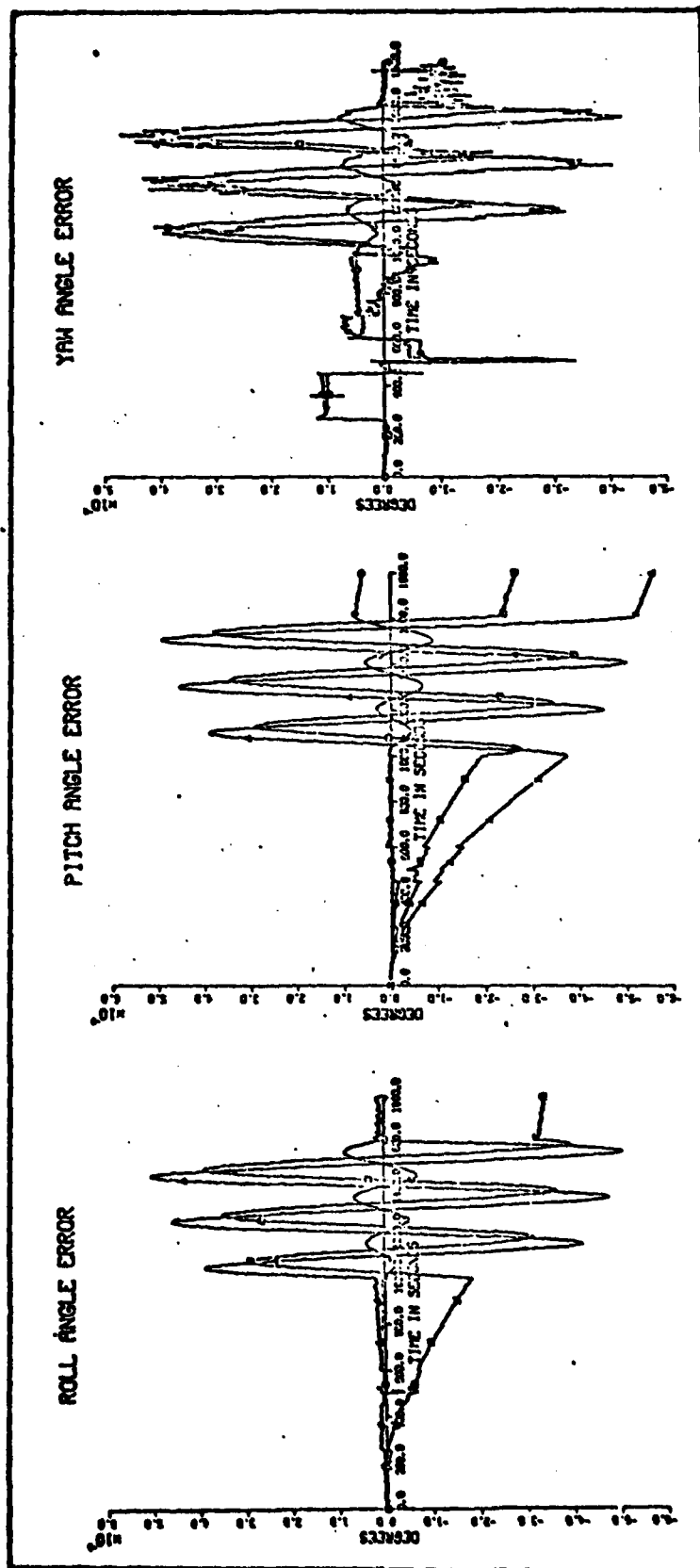


Figure 15c. Comparison of Attitude Errors for Case of Accelerometer Bias Error only.

- Case with accelerometer bias error only.
- Case with ideal sensors.
- △ Case with all accelerometer errors present.

same wave form as the yaw angle error with no accelerometer errors present, except that it ramps off after experiencing a step error at the outset of the climb.

Accelerometer Misalignment Error. Figure 16 shows the effect of the accelerometer misalignment error on the INS errors. Although the pulses induced at the maneuvers are more pronounced and the overall error more unsettled, the east velocity error that results from accelerometer misalignment has the same general form as that for the bias error only in the opposite direction. The magnitude is about six times smaller than that due to bias, but it still has the effect of offsetting some of the error caused by the bias. Also, the pulse introduced into the east velocity error by the evasive maneuver is more pronounced with the misalignment error. The longitude error that results is also of the opposite sign and about six times smaller than that achieved with the accelerometer bias error. The accelerometer misalignment had little effect on the north velocity error, and thus, the latitude error was also relatively unaffected by misalignment. The misalignment error did however, have an appreciable effect on the roll angle error. The roll angle experiences steps at the snap rolls, with the direction of the steps being dependent on the direction of the roll. This indicates that if the second roll had been in the same direction as the other rolls, the error in roll angle produced by the misalignment error would have been increased.

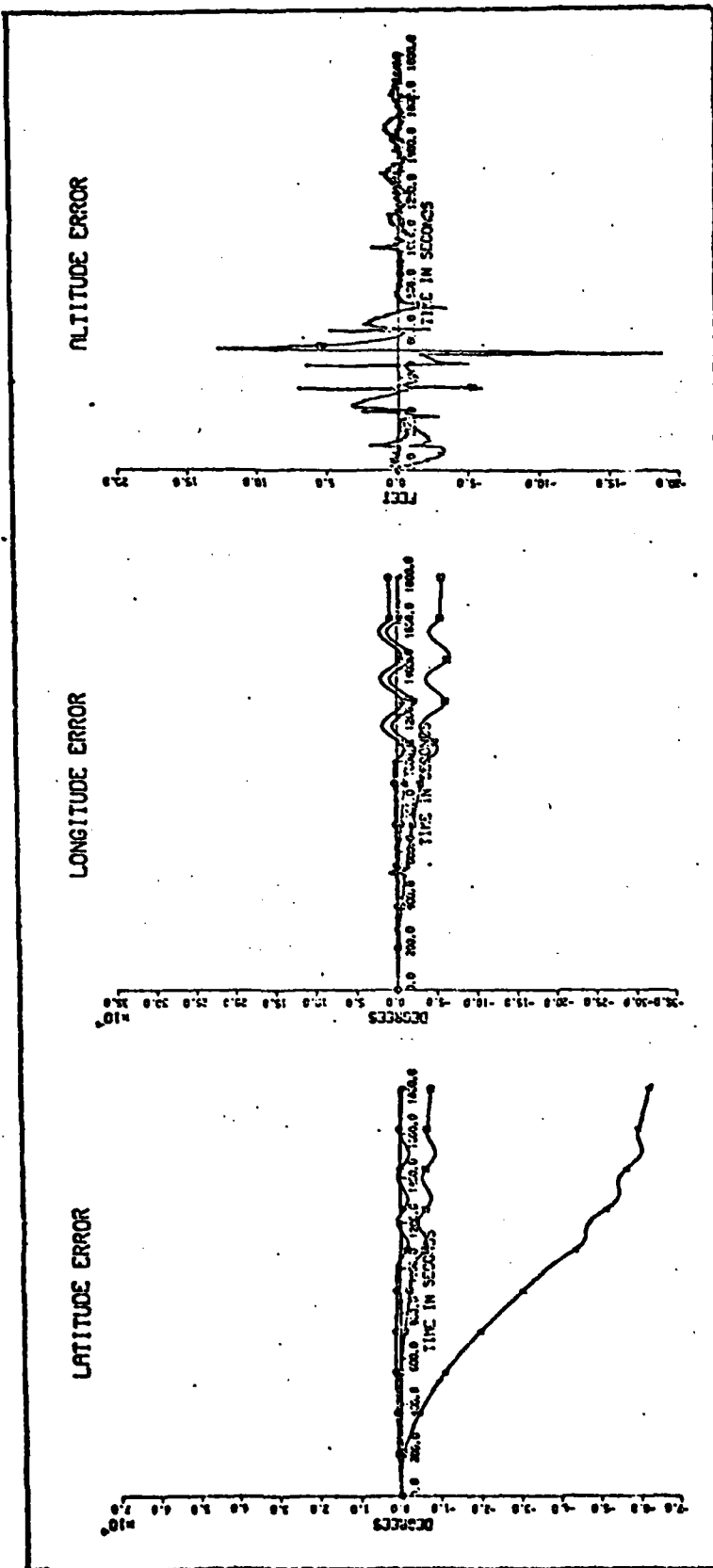


Figure 16a. Comparison of Position Errors for Case of Accelerometer Misalignment Error only, all Accelerometer Errors, and Ideal Sensors

- Case with accelerometer misalignment only.
- Case with ideal sensors.
- △ Case with all accelerometer errors present.

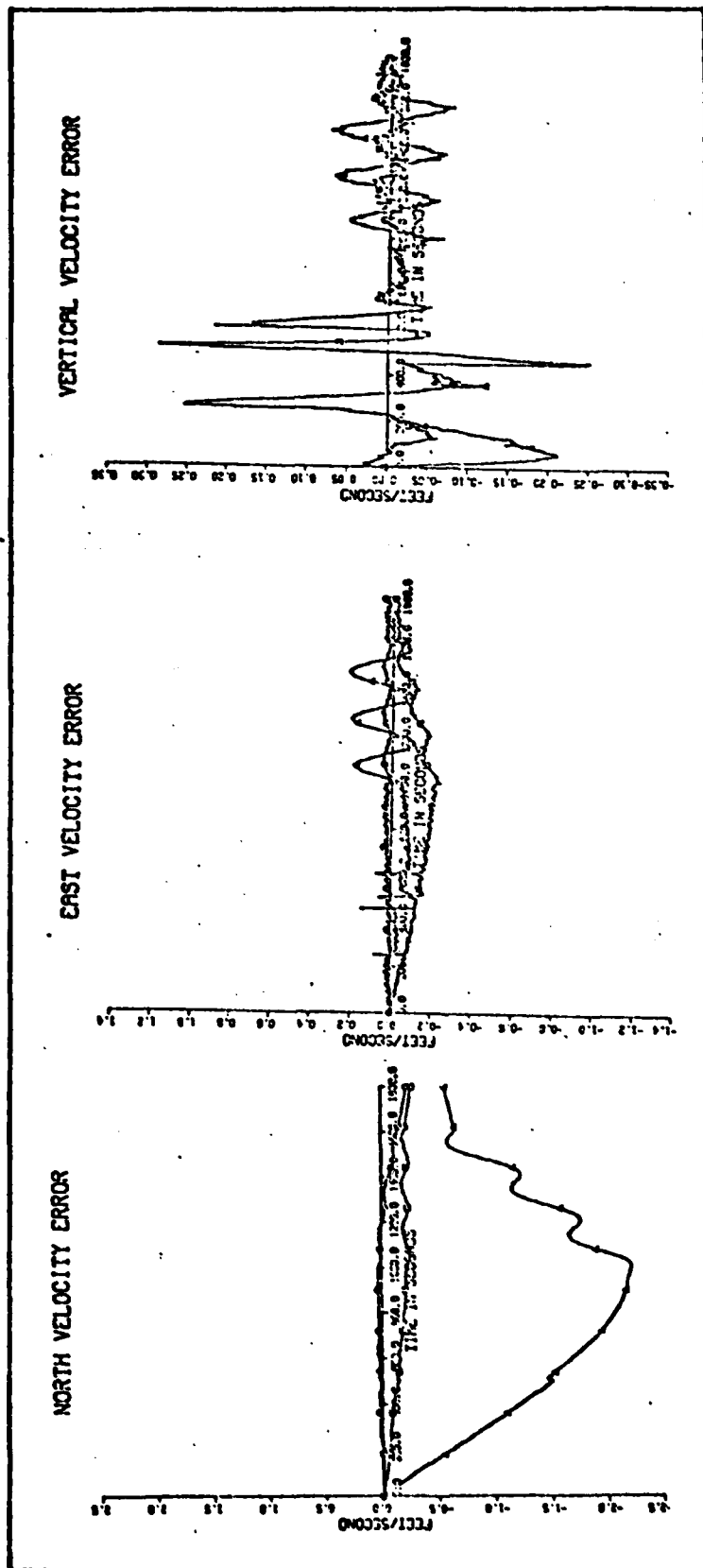


Figure 1bb. Comparison of Velocity Errors for Case of Accelerometer Misalignment Error only, all Accelerometer Errors, and Ideal Sensors

- Case with accelerometer misalignment error only.
- Case with ideal sensors.
- △ Case with all accelerometer errors present.

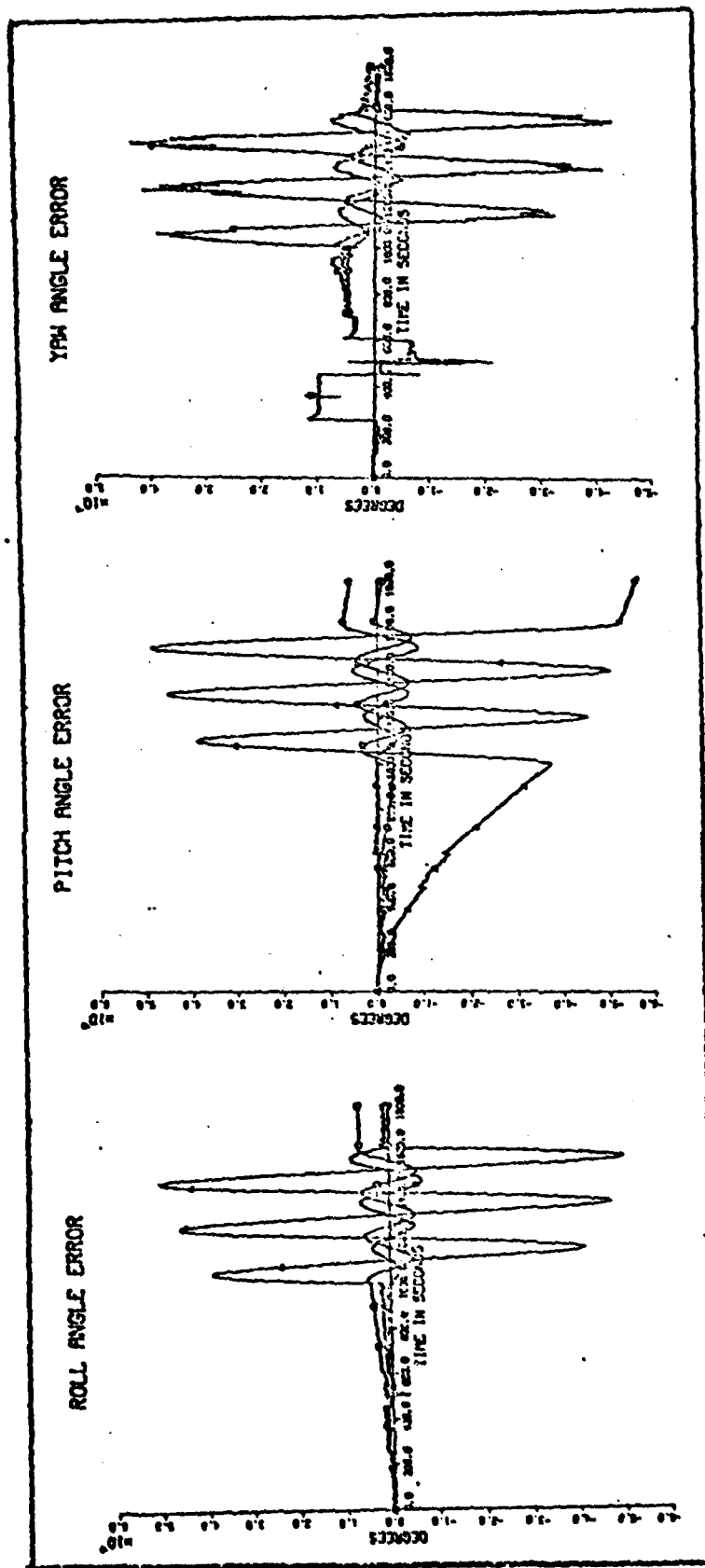


Figure 16c. Comparison of Attitude Errors for Case of Accelerometer Misalignment Error only, all Accelerometer Errors, and Ideal Sensors

- Case with accelerometer misalignment error only.
- Case with ideal sensors.
- △ Case with all accelerometer errors present.

The evasive maneuver introduces a pulse that is about half the magnitude of the pulse produced when all accelerometer errors are present. Pitch and yaw angles show negligible effects from the misalignment error.

Accelerometer Scale Factor Error. The effects of the accelerometer scale factor error on the INS parameter is illustrated in Figure 17. The north velocity error is only slightly effected by the accelerometer by the accelerometer scale facotr error. Likewise the scale factor error produces negligible error in latitude. However, in regards to east velocity error, the scale factor error accounts for a large portion of this error during the period before the second snap roll and during the loiter maneuver. The reason for the decreased effect of the scale factor error between the second snap roll and the loiter results because the error in the east velocity due to the scale factor error is in the opposite direction from a similar step error caused by some other source. The longitude error exhibited similar characteristics as the east velocity error. The large spike that occurs at the evasive maneuver which appeared as if it may be caused by the scale factor error, is much clearer in the longitude error. Since it is present for the case of an ideal accelerometer, it must be caused by some source other than accelerometer errors. The Euler angles are all relatively unaffected by the scale factor error.

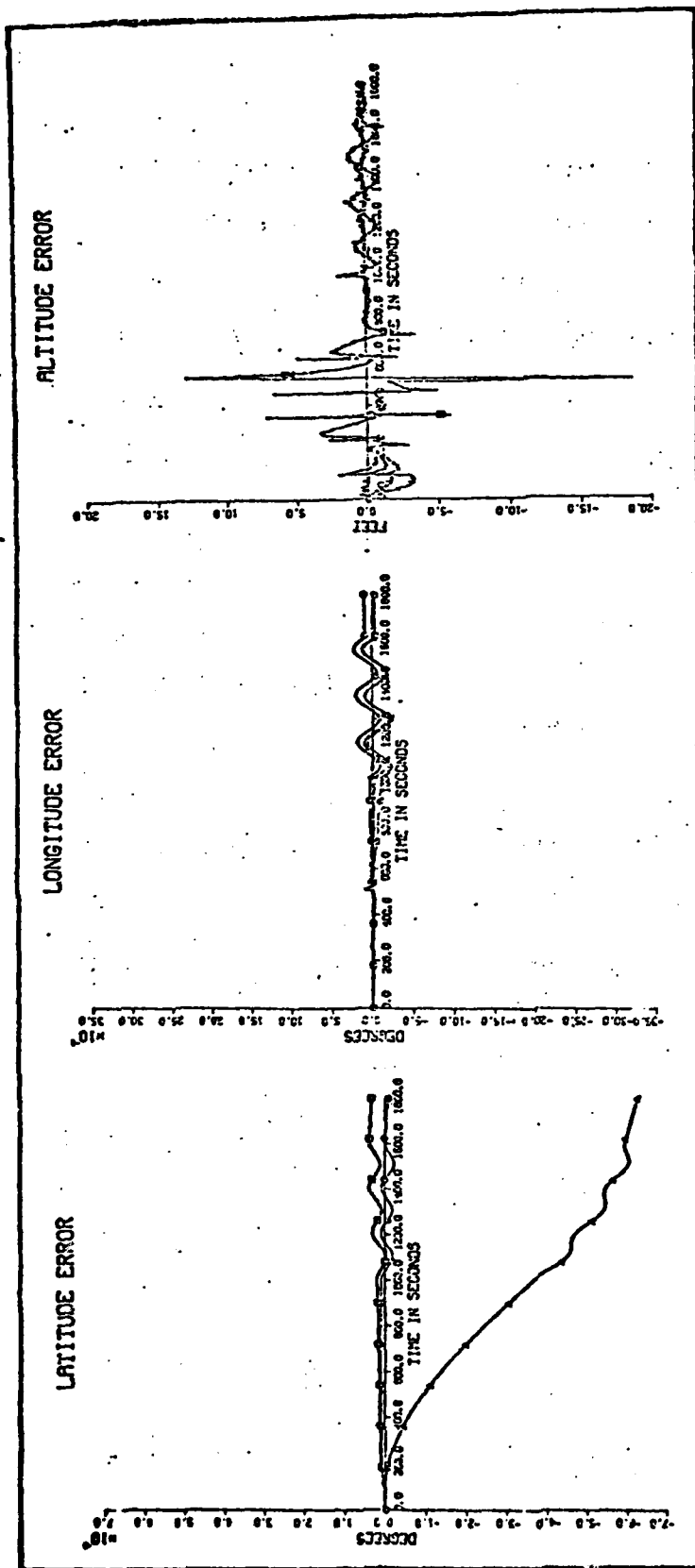


Figure 17a. Comparison of Position Errors for Case of Accelerometer Scale Factor Error only, all Accelerometer Errors, and Ideal Sensors

- Case with accelerometer scale factor error only.
- Case with ideal sensors.
- △ Case with all accelerometer errors present.

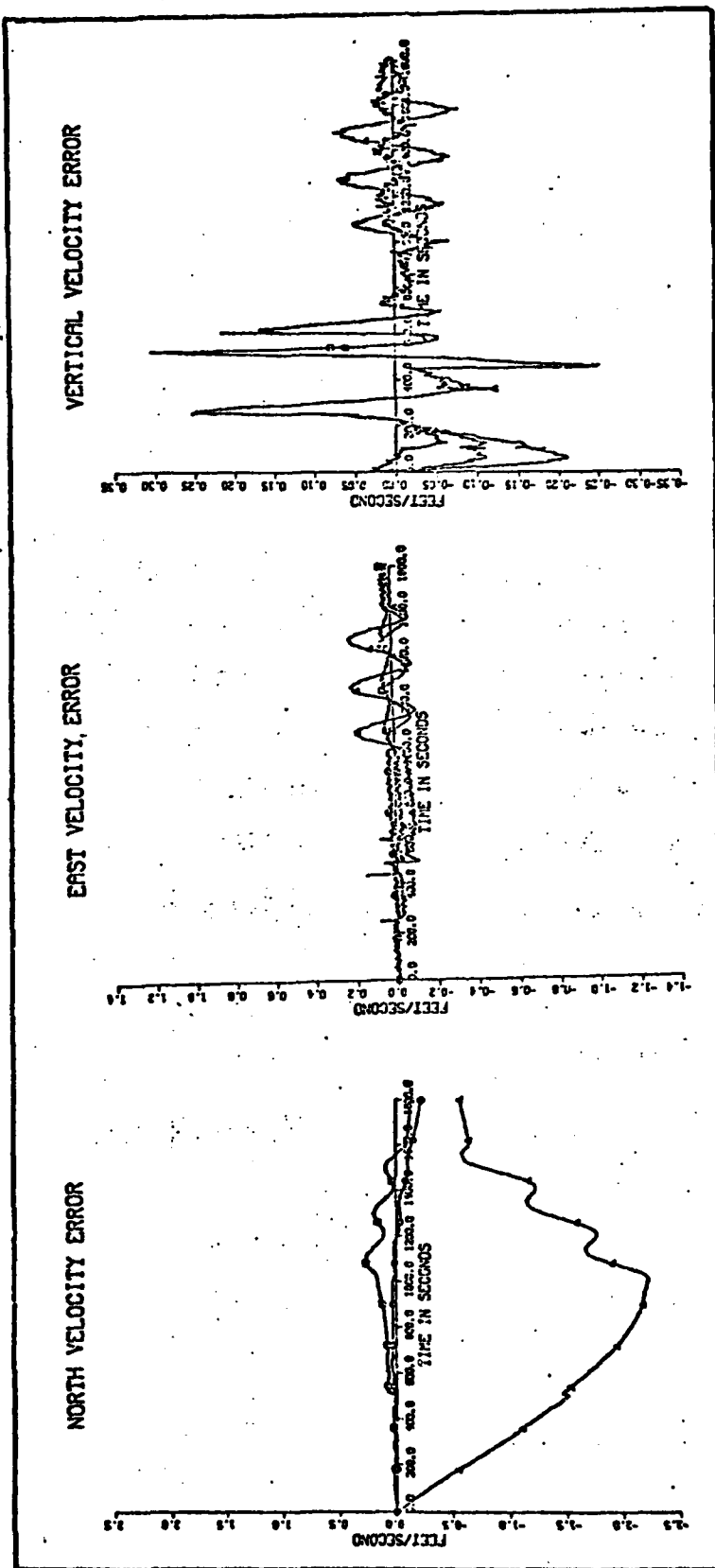


Figure 17b. Comparison of Velocity Errors for Case of Accelerometer Scale Factor Error only, all Accelerometer Errors, and Ideal Sensors

- Case with accelerometer scale factor error only.
- Case with ideal sensors.
- △ Case with all accelerometer errors present.

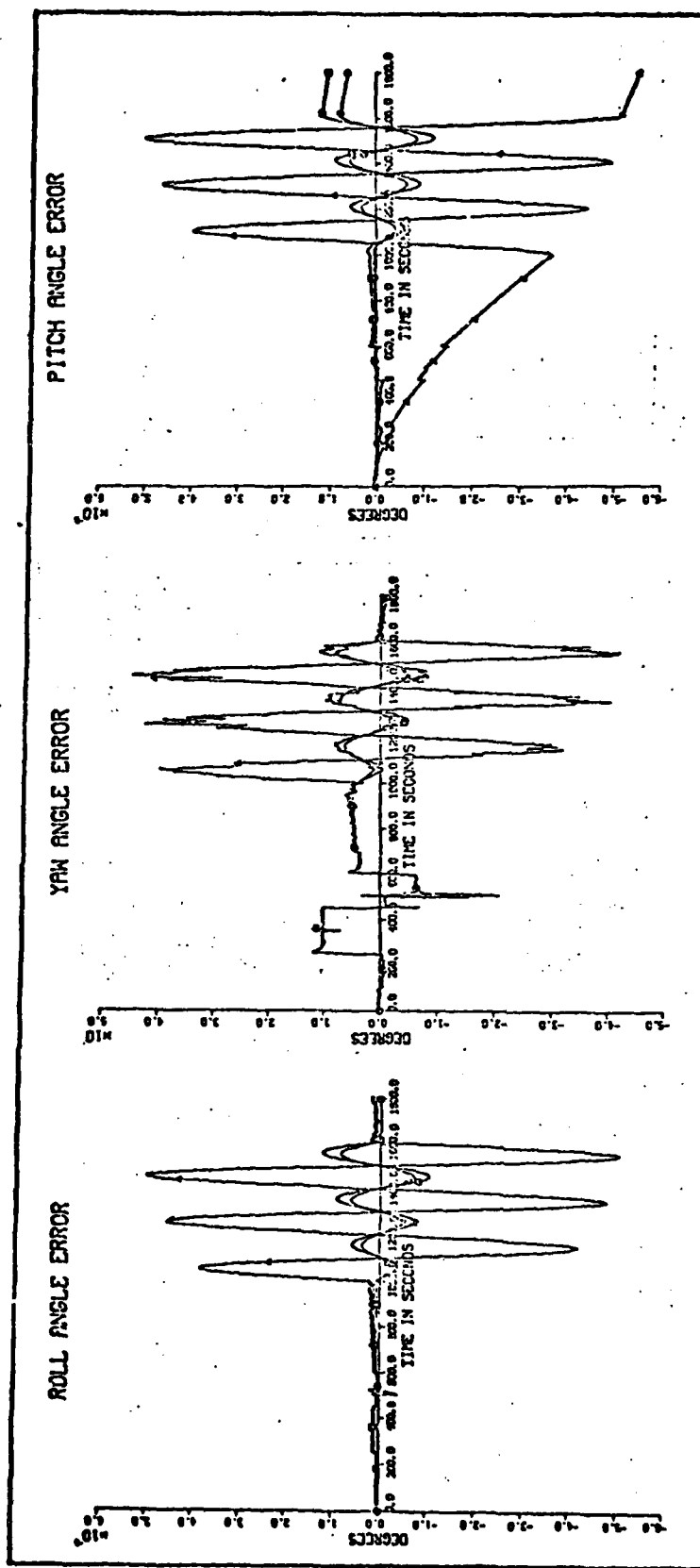


Figure 17c. Comparison of Attitude Errors for Case of Accelerometer Scale Factor Error only, all Accelerometer Errors, and Ideal Sensors

- Case with accelerometer scale factor error only.
- Case with ideal sensors.
- △ Case with all accelerometer errors present.

Other Accelerometer Errors. The other two error sources modeled for the quartz-flexure accelerometer are the non-linearity and cross-coupling error. Figures 18 and 19 show the plots obtained for each of these cases. The only noticeable effect either error source has on the INS errors is the effect of the nonlinearity error on the east velocity error during the period from the last snap roll until the loiter. During this period, the east velocity error due to accelerometer non-linearity subtracts from the velocity error that results when no sensor errors are present. This creates a small reduction in the overall error in east velocity and thus the longitude error during this phase of the flight.

Summary. The overall errors in the INS parameters caused by the accelerometer errors are somewhat smaller than those resulting from laser gyro errors. The bias and misalignment error dominate the effect of the accelerometer errors. A reduction in the accelerometer errors should result in a direct reduction of the velocity errors since the accelerometer errors are coupled into the velocities in an additive fashion. Since the position and attitude errors are driven by the velocity errors, reduction in the velocity errors should result in reductions in both position and attitude errors.

As is done for the case of laser gyro errors, an 84 minute simulation is made to illustrate the effects of the accelerometer errors over one Schuler period. Figure 20

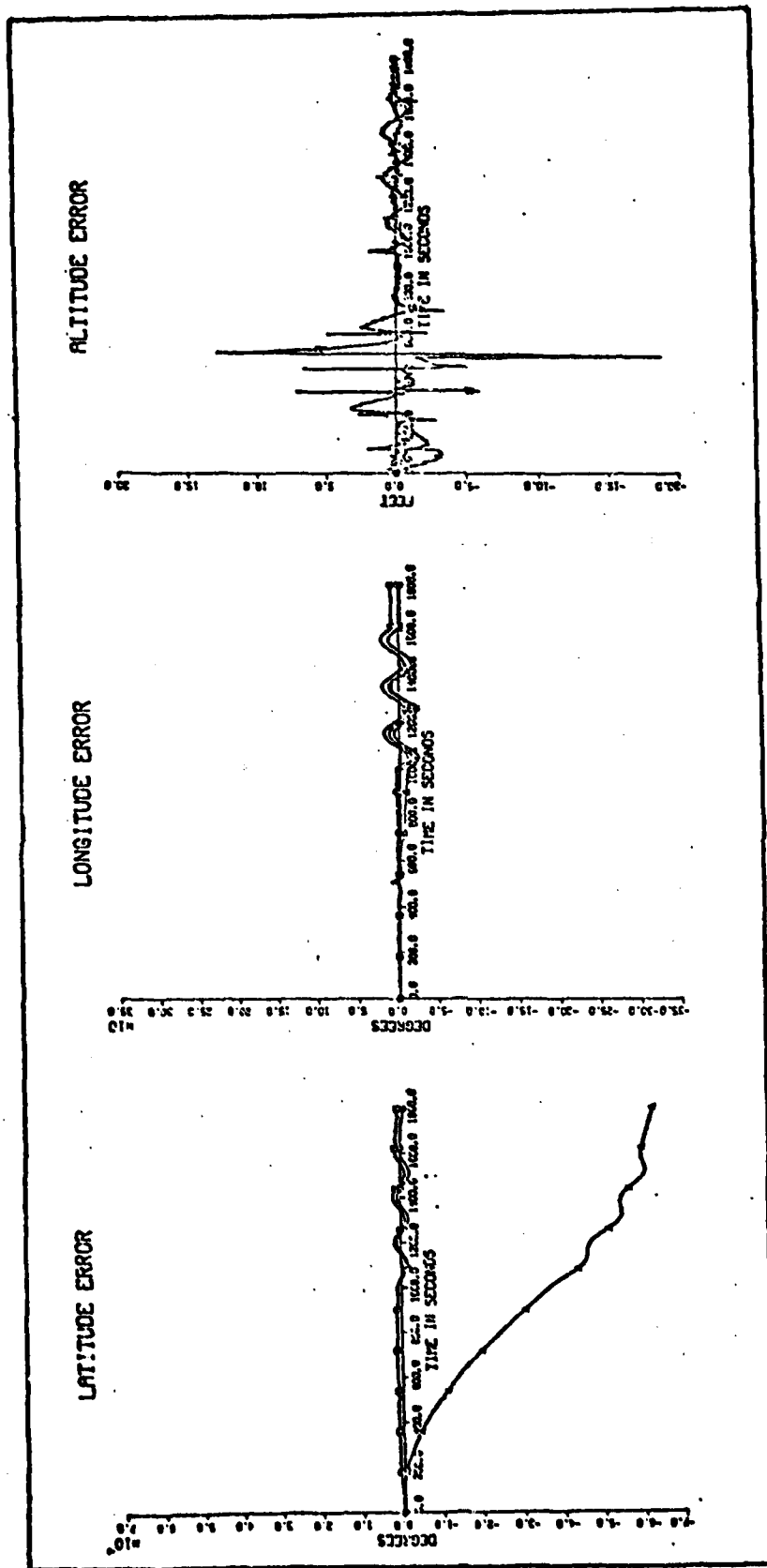


Figure 18a. Comparison of Position Errors for Case of Accelerometer Nonlinearity Error only, all Accelerometer Errors, and all Ideal Sensors

- Case with accelerometer nonlinearity error only.
- Case with all ideal sensors.
- △ Case with all accelerometer errors.

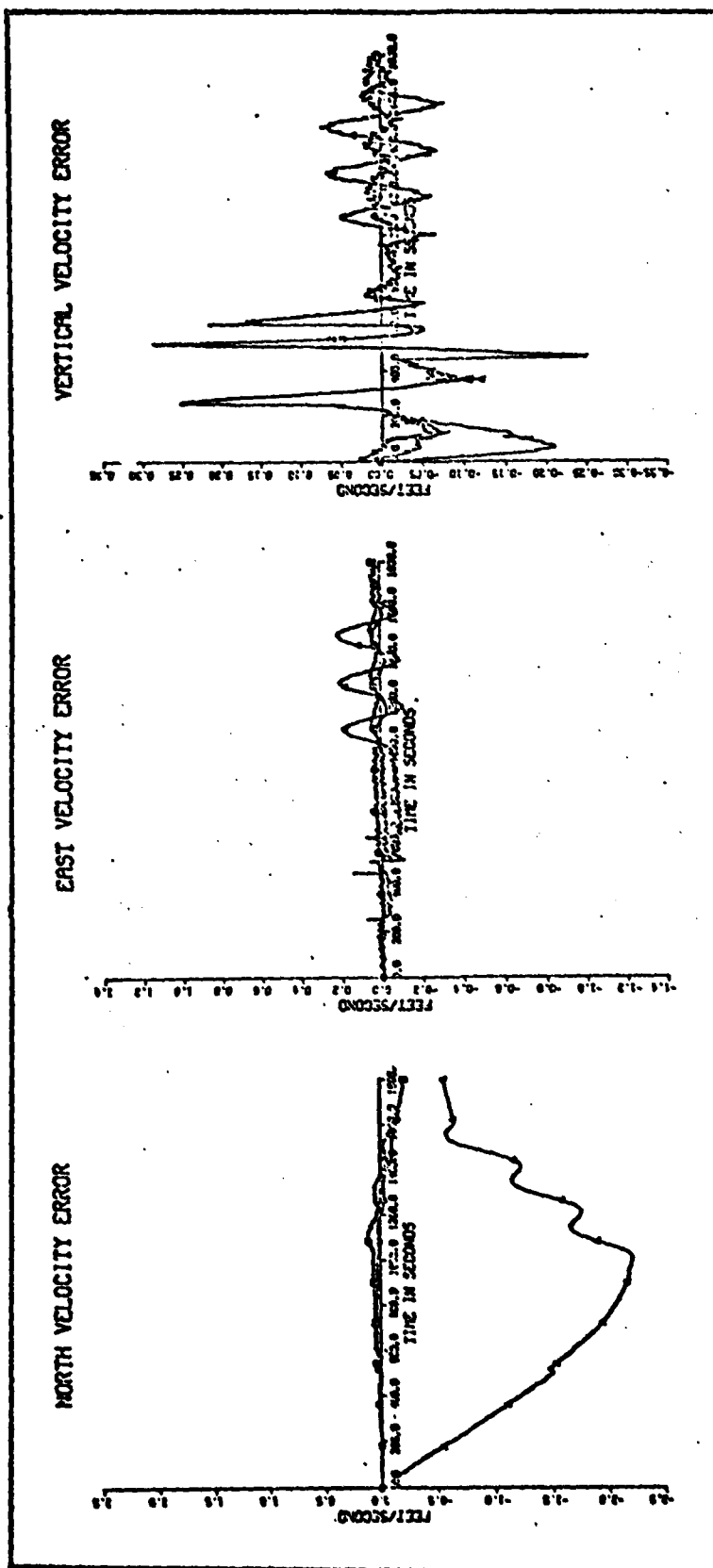


Figure 18b. Comparison of Velocity Errors for Case of Accelerometer Nonlinearity Error only, all Accelerometer Errors, and Ideal Sensors

- Case with accelerometer scale factor error only.
- Case with ideal sensors.
- △ Case with all accelerometer errors present.

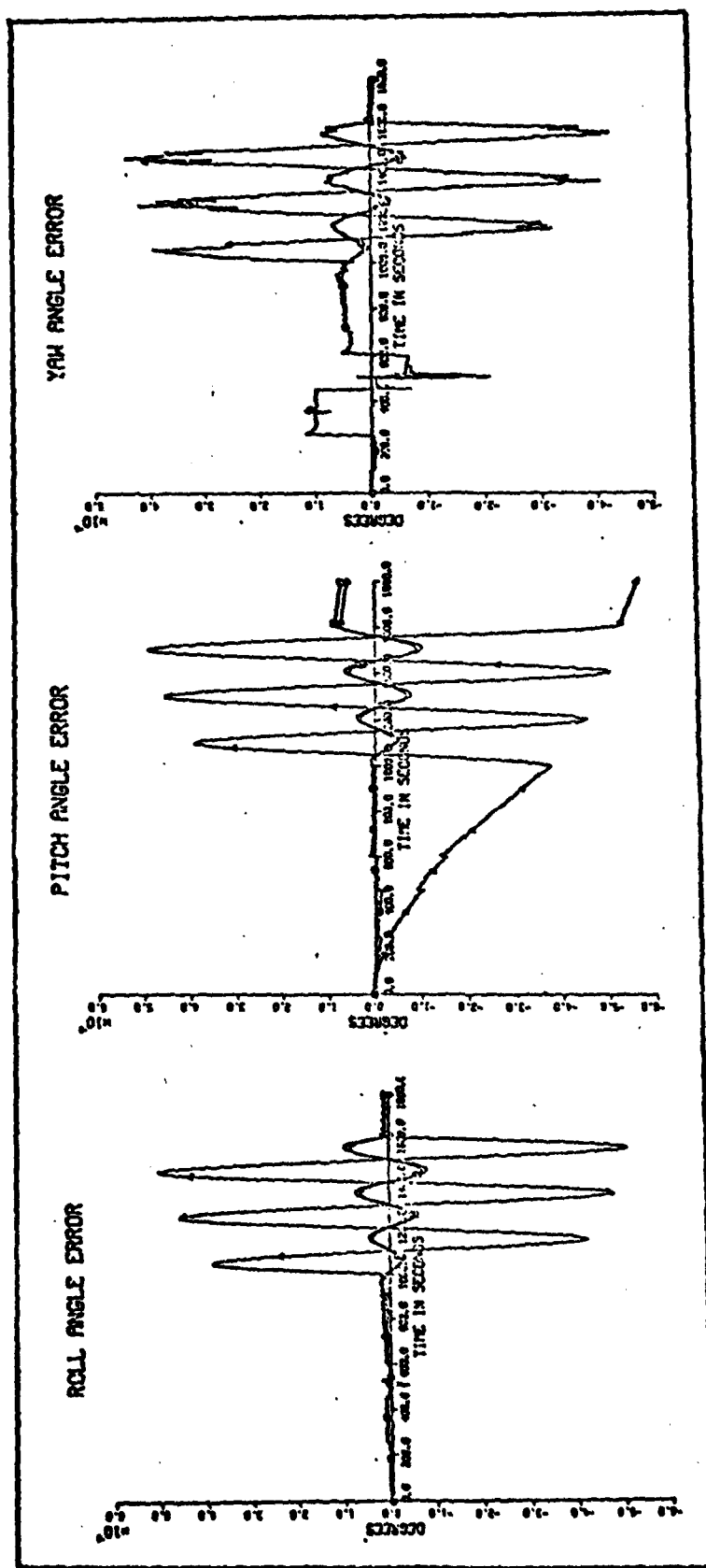


Figure 18c. Case of Attitude Errors for Case of Accelerometer Nonlinearity Error only all Accelerometer Errors, and all Ideal Sensors

- *□ Case with accelerometer nonlinearity error only.
- *○ Case with all ideal sensors.
- *△ Case with all accelerometer errors.

*These are so close in magnitude as to be indistinguishable.

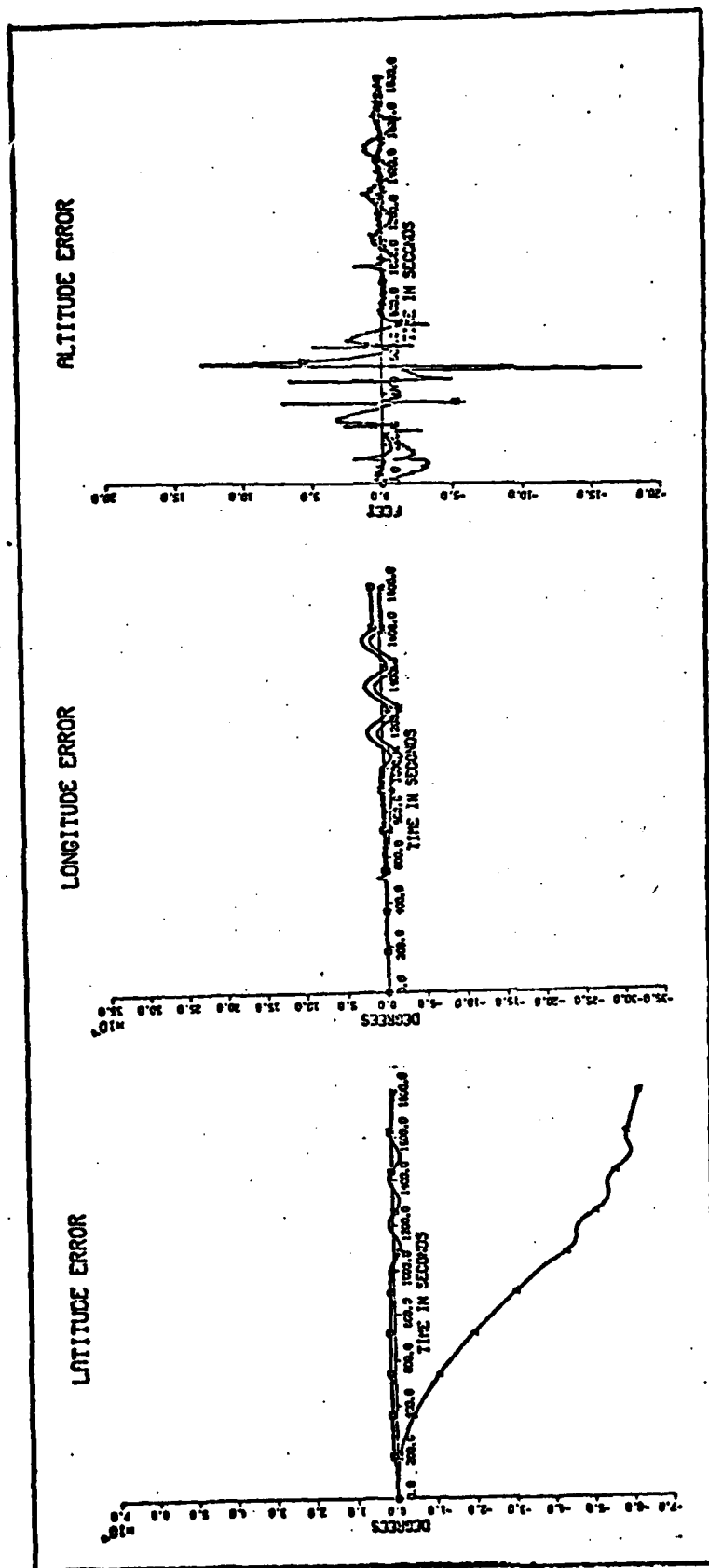


Figure 19a Comparison of Position Errors for Case of Accelerometer Cross-Coupling Error only, all Accelerometer Errors, and all Ideal Sensors

- * □ Case with accelerometer cross-coupling error only.
- * ○ Case with ideal sensors.
- * △ Case with all accelerometer errors present.

*These are so close in magnitude as to be indistinguishable.

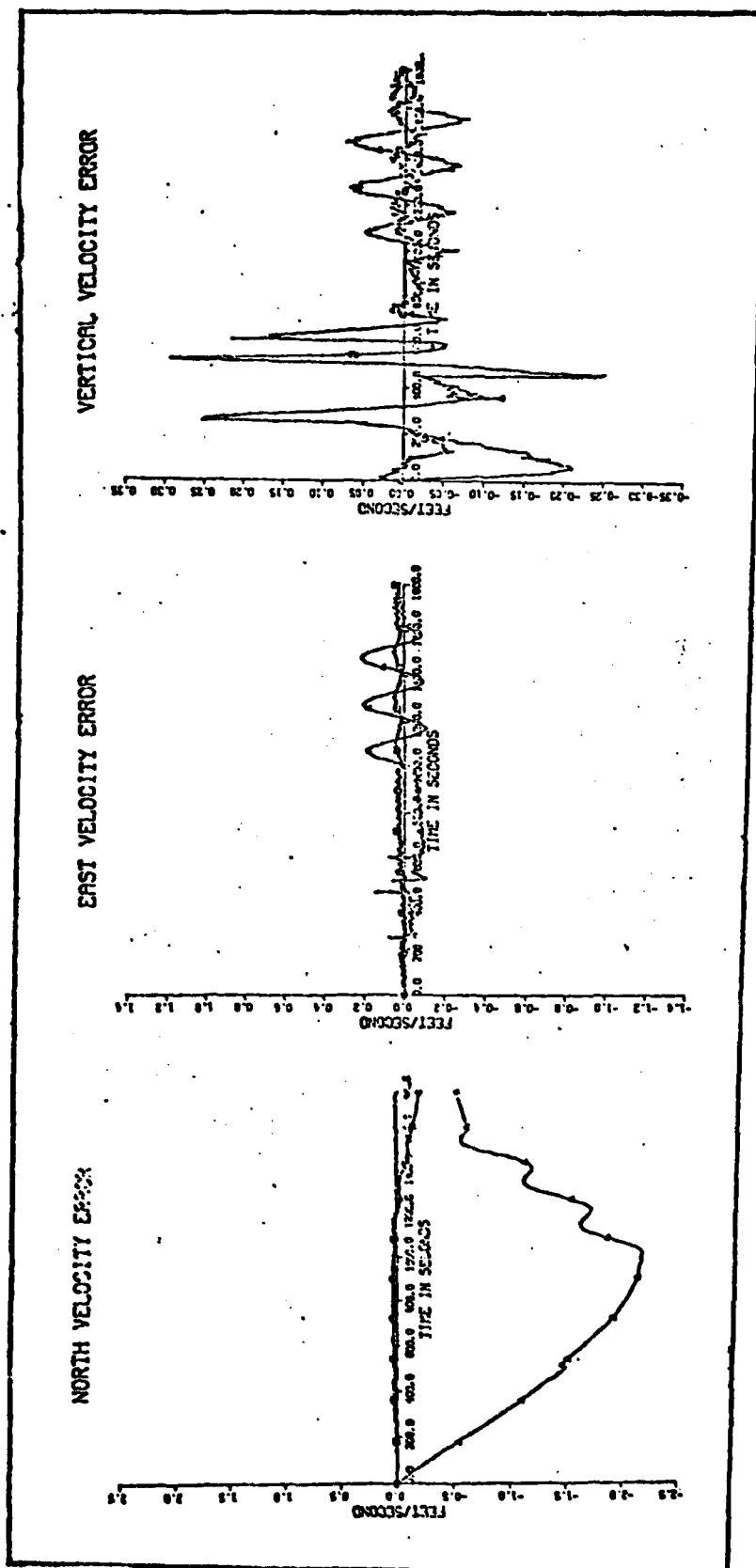


Figure 19b. Comparison of Velocity Errors for Case of Accelerometer Cross-Coupling Error only, all Accelerometer Errors, and all Ideal Sensors

- *□ Case with accelerometer cross-coupling error only.
- *○ Case with ideal sensors.
- *△ Case with all accelerometer errors.
- *These are so close in magnitude as to be indistinguishable.

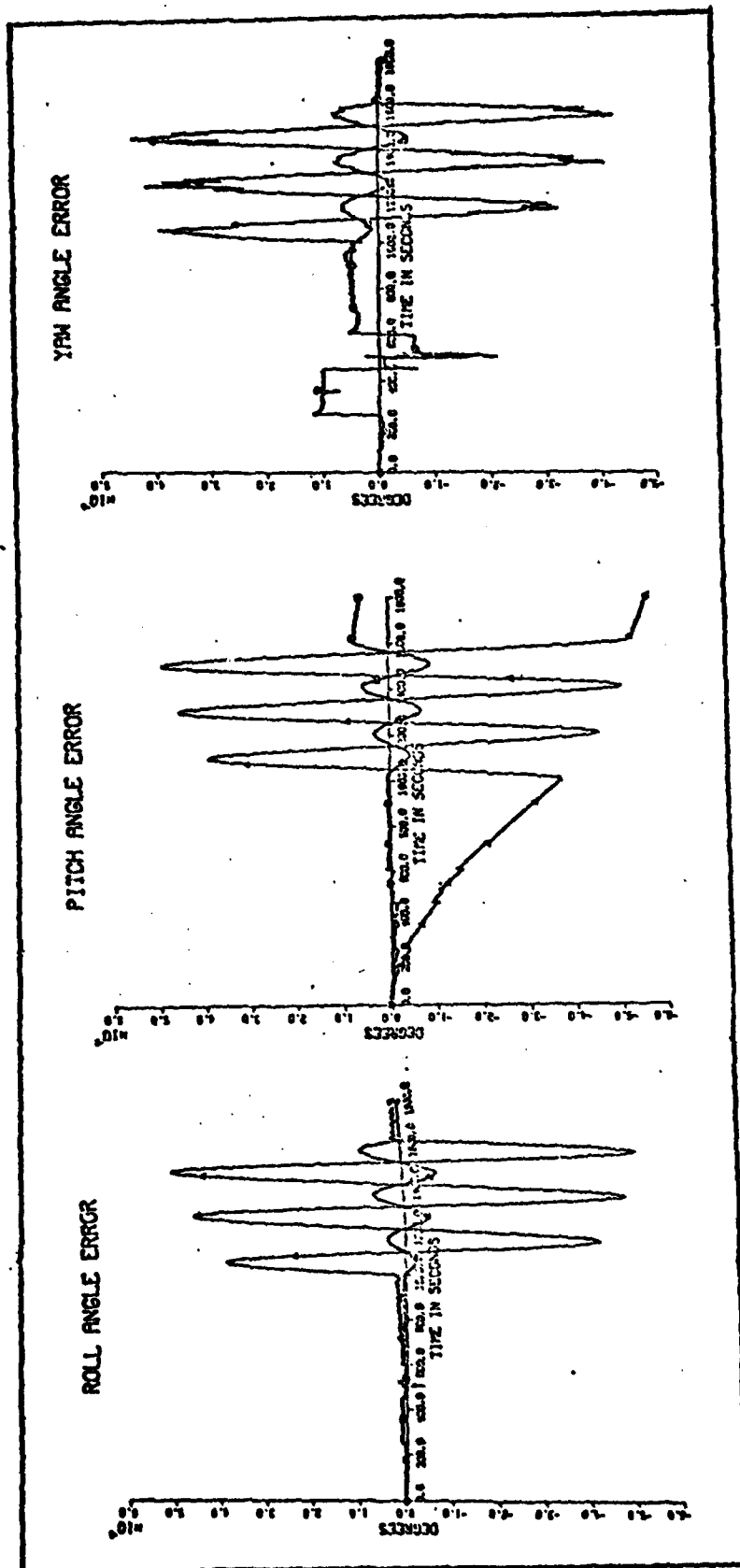


Figure 19c. Comparison of Attitude Errors for Case of Accelerometer Cross-Coupling
Error only, all Accelerometer Errors, and all Ideal Sensors

- * □ Case with accelerometer cross-coupling error only.
- * ○ Case with ideal sensors.
- * △ Case with all accelerometer errors only.

*These are so close in magnitude as to be indistinguishable.

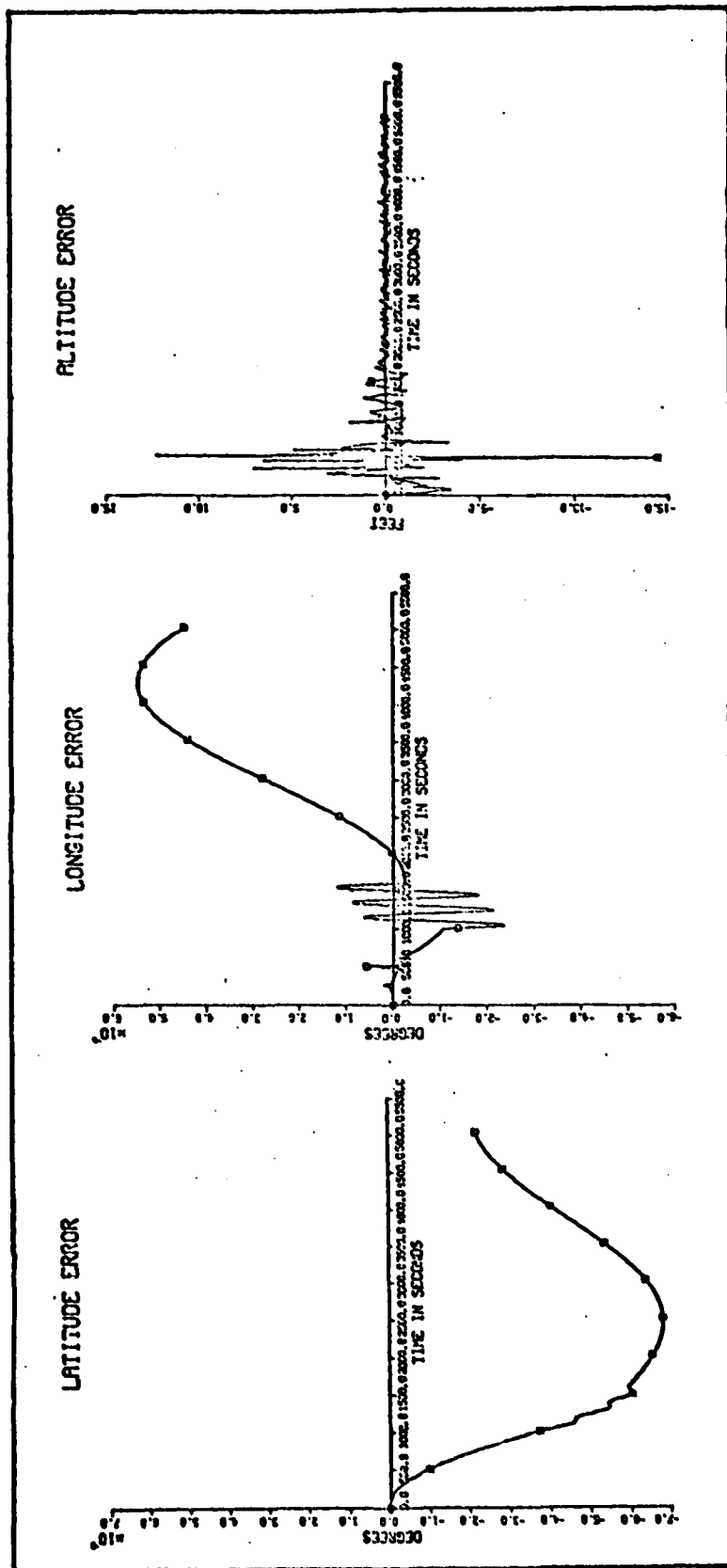


Figure 20a. Simulation Results Obtained Over one Schuler Period for Case of all Accelerometer Errors.

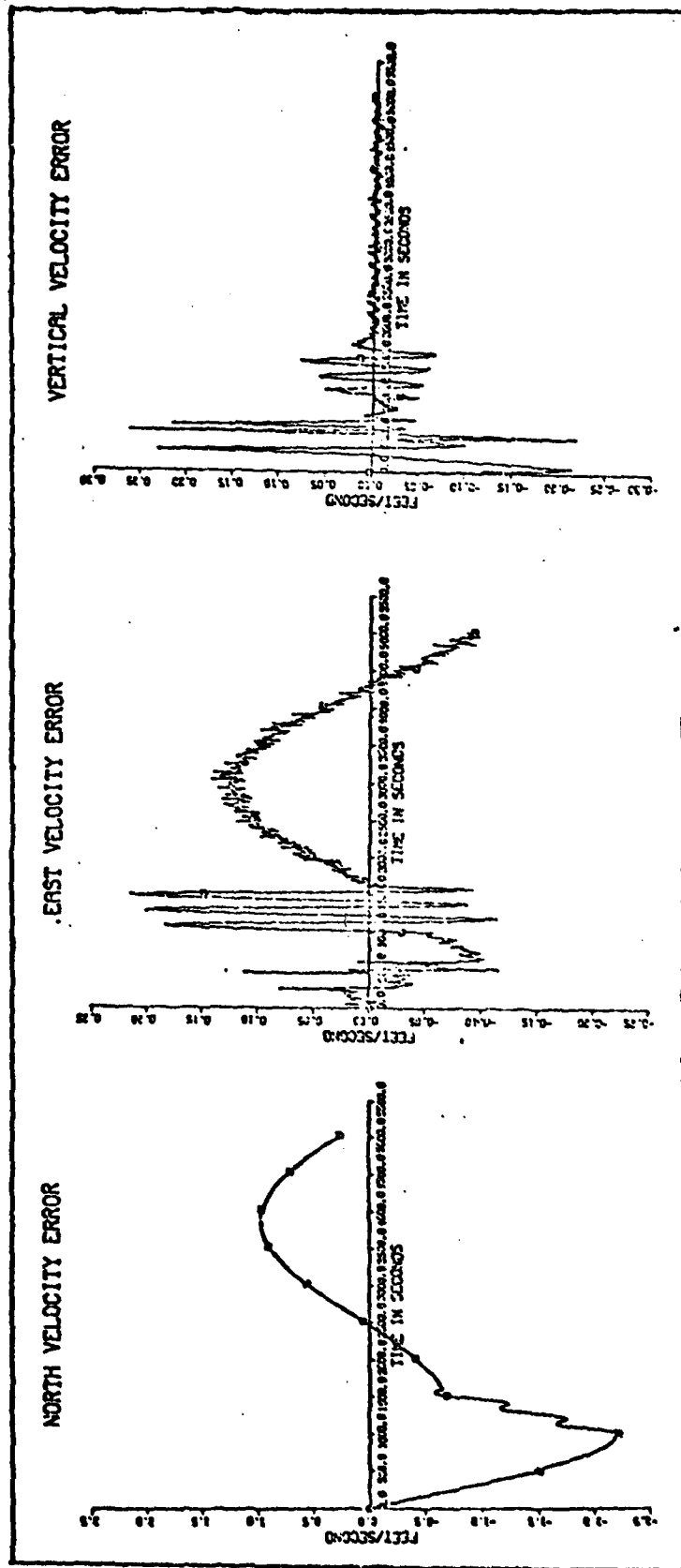


Figure 20b. Simulation Results Obtained Over one Schuler Period for Case of all Velocity Errors

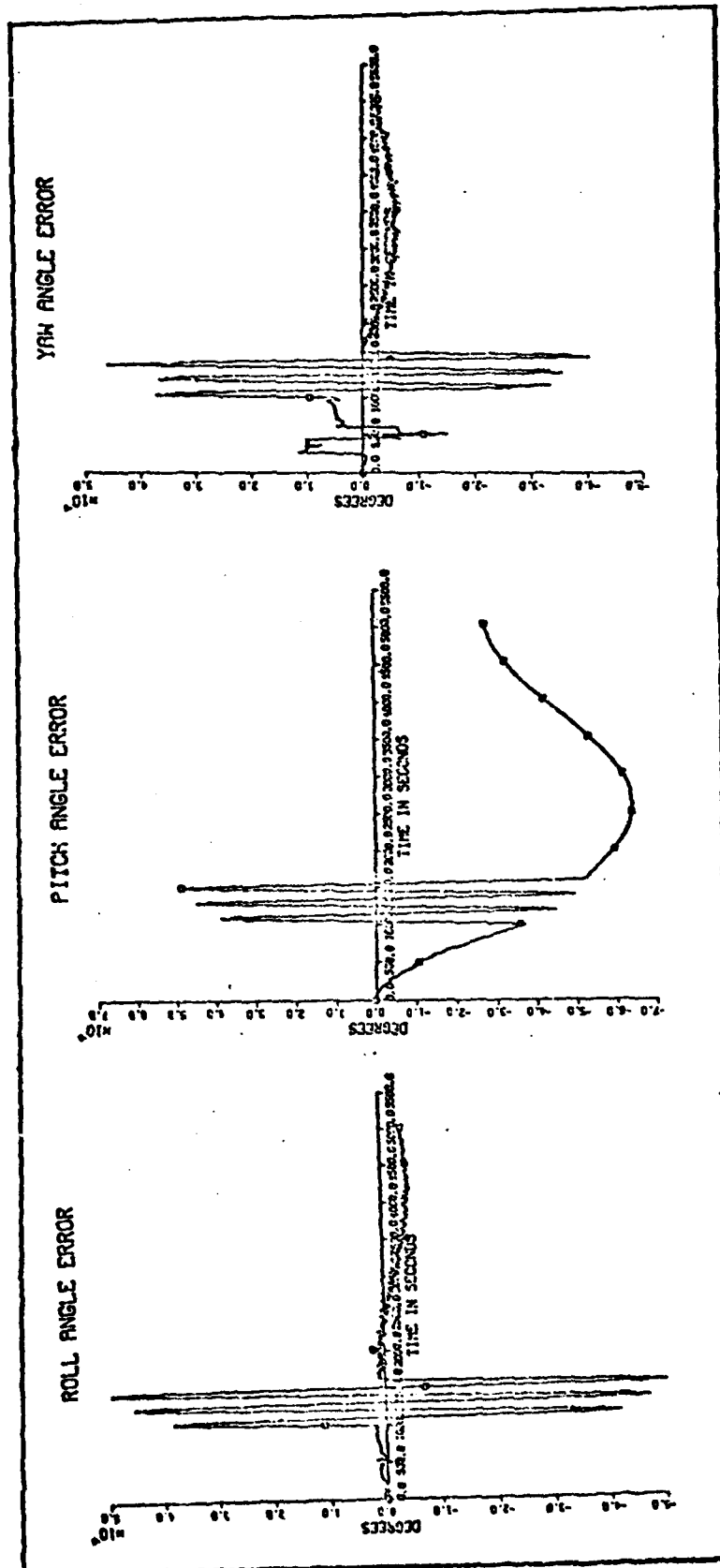


Figure 20c. Simulation Results Obtained Over one Schuler Period for Case of all Attitude Errors.

shows the error time histories that are obtained from this simulation. Once again, as is true for the case of laser gyro errors, the major portion of the errors is a result of the effects of the high dynamic maneuvers performed during the first 30 minutes of flight. However, The values of the INS errors due to accelerometer errors are much smaller than those caused by the laser gyro errors. Also, both east and north velocity errors are within the specification as is the position errors. This indicates that reducing the laser gyro errors should be more beneficial than reducing accelerometer errors.

Effect of Structural Modes

The simulations discussed in the previous sections do not account for structural mode effects. This section presents simulations obtained with structural modes sensed and provides an analysis of their effects on the INS errors.

Figure 21 shows the time histories of the INS errors with structural modes sensed plotted against those with no structural modes sensed. In both cases the sensors are assumed ideal.

The structural modes produce a definite degradation in the overall INS performance. The roll angle is effected less than the other attitude errors. With structural modes present, the roll and evasive maneuvers produce some large pulse transients into the roll angle. The one from the evasive maneuver is nearly twice as large as those from the rolls. Also, a sinusoid results during the loiter.

AD-A080 373

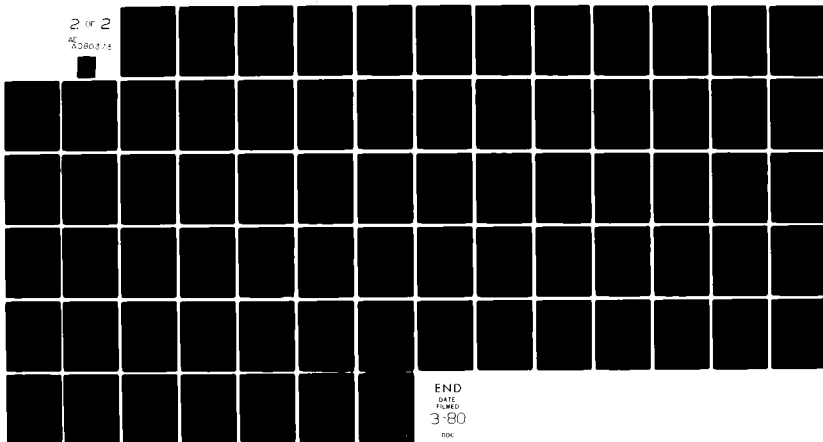
AIR FORCE INST OF TECH WRIGHT-PATTERSON AFB OH SCH00--ETC F/8 17/7
DETERMINISTIC ANALYSIS OF THE EFFECTS OF SENSOR ERRORS ON STRAP--ETC(U)
DEC 79 R H REYNOLDS
AFIT/6E/EE/79-30

UNCLASSIFIED

NL

2 of 2

AD-A080373



END

DATE

FILED

3-80

DOC

Part of the cause of this sinusoid is the coupling of the latitude error into the roll angle error. The coupling of the other attitude errors also adds to the sinusoid.

The presence of the structural modes causes the pitch angle to be quite sensitive to the aircraft maneuvers. The pitch angle exhibits a ramp during the initial descent. At each of the snap rolls, the pitch angle error experiences steps on the order of 0.03° . Even though one of the rolls is in the opposite direction of the other two, the steps caused by the snap rolls have an additive effect. The evasive maneuver produces a negative step error that is about twice as large as that of the snap roll. The pitch angle error is also sensitive to the weapon delivery. A pulse transient results from this maneuver. Although much smaller than the one at the weapon delivery, the ascent produces a transient in the pitch angle error, also. These transients reflect the shape of the longitudinal structural modes. During the periods of flight where the pitch angle error is not experiencing steps or transients, it exhibits a ramp-like nature. Also, as in the roll angle error, the latitude error couples back into the pitch angle error during the loiter.

The yaw angle also has significant errors induced into it by the aircraft maneuvers when the structural modes are sensed. However, the yaw angle error that results is negative. This should have the effect of reducing the yaw angle

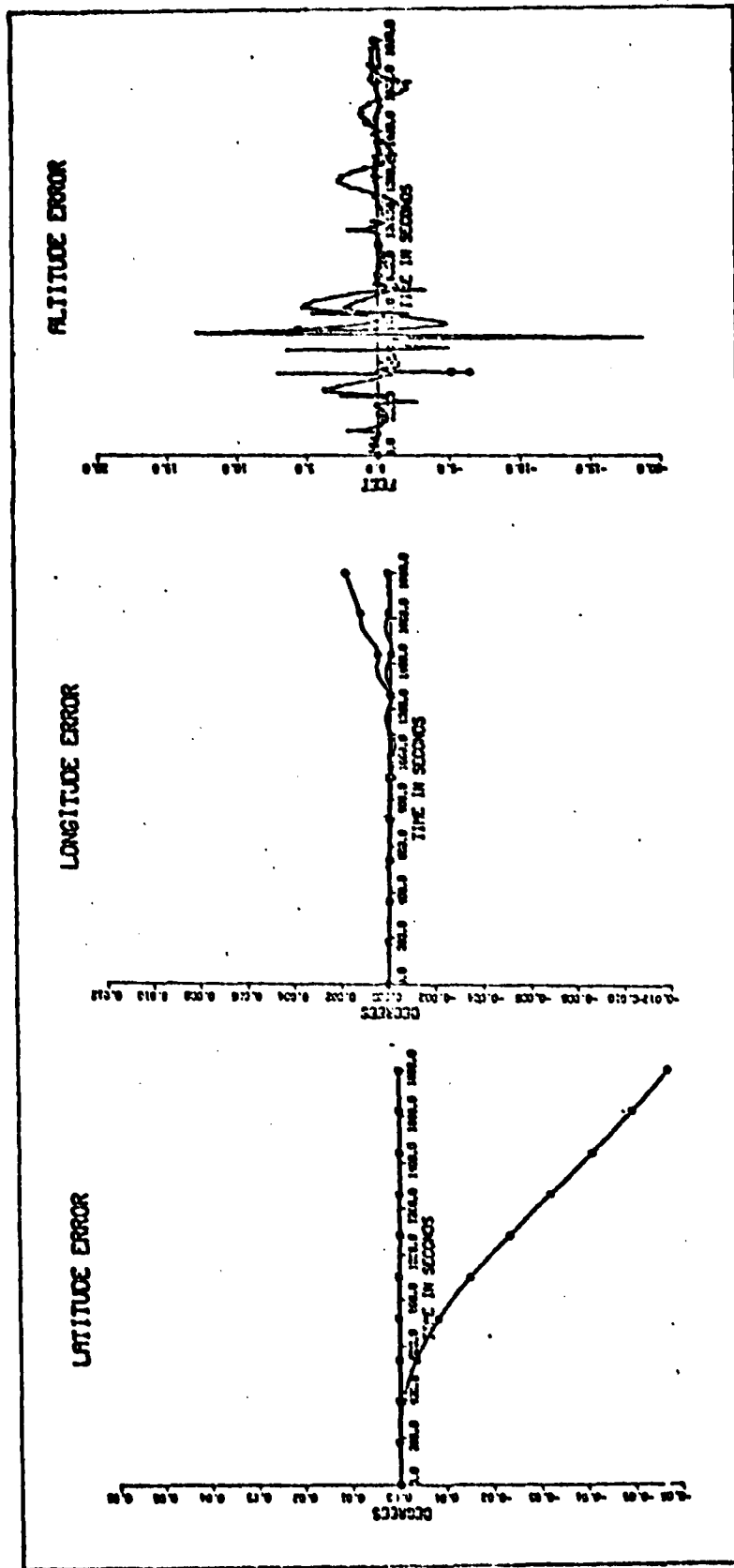


Figure 21a. Comparison of Position Errors for Case of Structural Modes and No Structural Modes. Both are With Ideal Sensors.

- Case without structural modes.
- Case with structural modes.

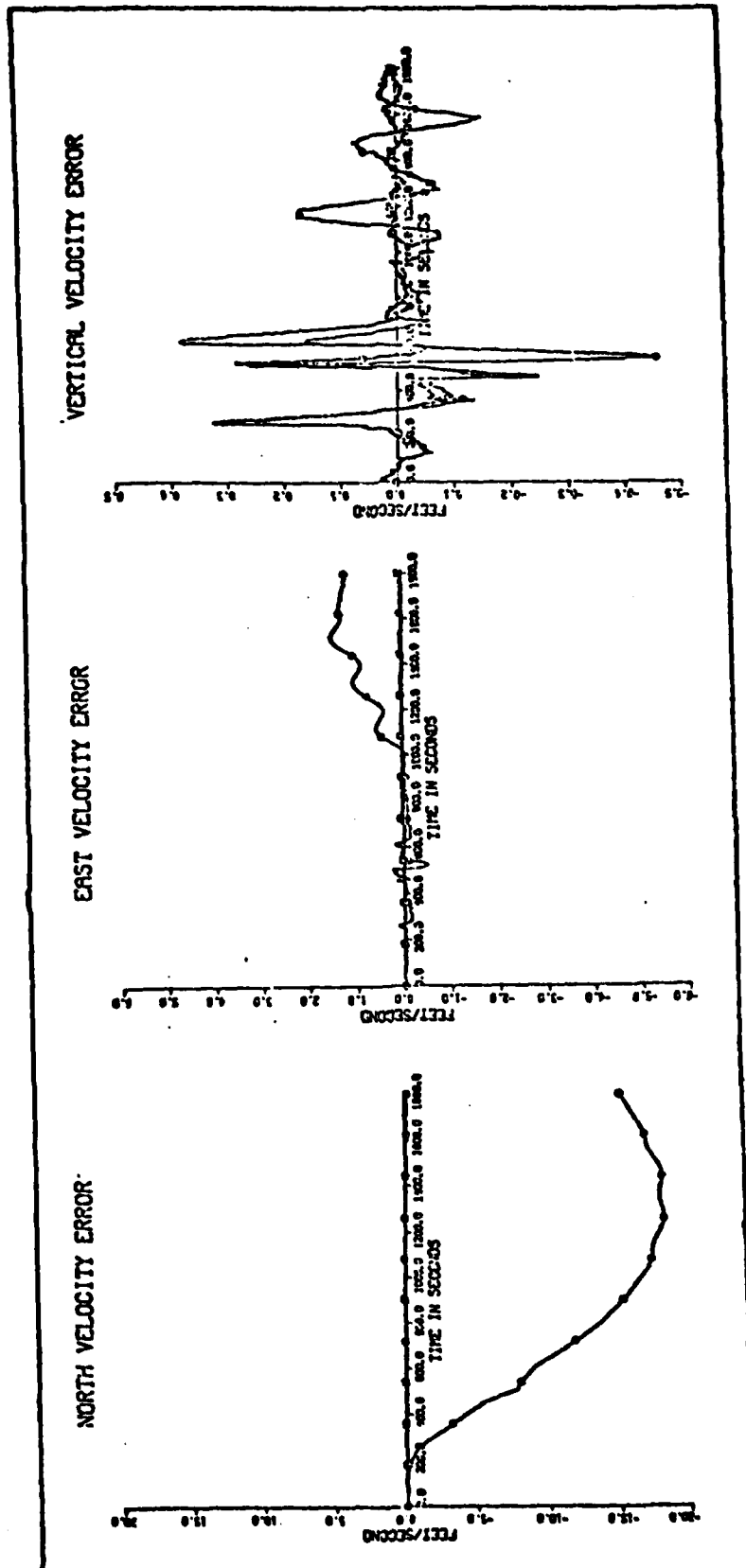


Figure 21b. Comparison of Velocity Errors for Case of Structural Modes and No Structural Modes. Both are With Ideal Sensors.

- Case without structural modes.
- Case with structural modes.

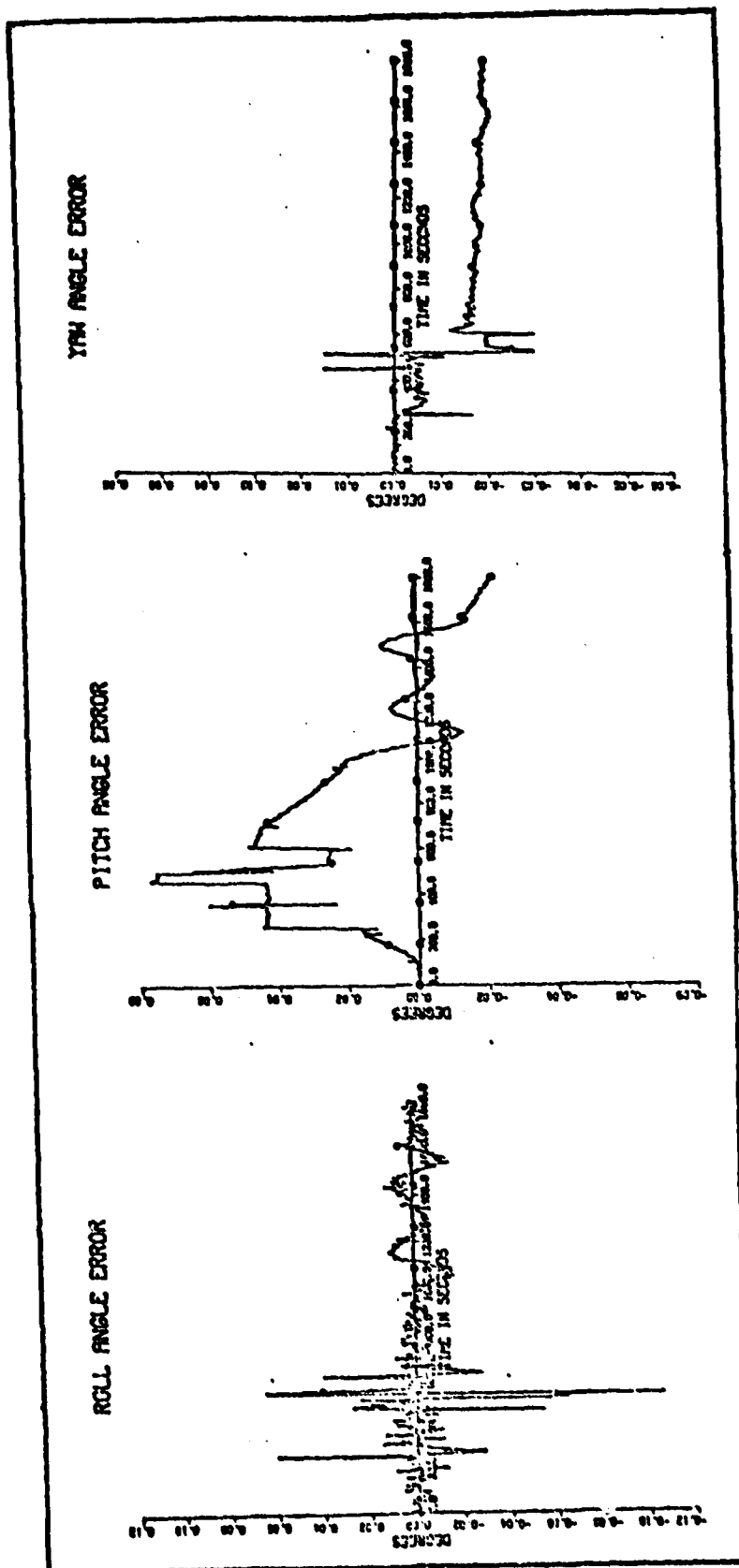


Figure 21c. Comparison of Attitude Errors for Case of Structural Modes and No Structural Modes. Both are With Ideal Sensors.

- Case without structural modes.
- Case with structural modes.

error when the laser gyro misalignment error is present. The roll angle error couples into the yaw angle error resulting in large transients at each snap roll. The evasive maneuver results in a large negative step error. After the final snap roll has taken place, the yaw angle becomes quite benign. There is only a small sinusoid during the loiter, therefore, there must be a small amount of coupling from the latitude errors.

One of the most significant effects of the structural modes is in the north velocity error. The north velocity reaches a value of -18 ft/sec. The steps that result in the attitude angle errors during the aircraft maneuvers integrate into the north velocity error causing the ramp-like behavior. As a result of this velocity error, the latitude error is also driven to exhibit a ramp-like nature and is quite large (3.6 nm) by the end of the 30 minute flight.

The east velocity error is less effected by the structural modes. Until the loiter, the only significant effect of the structural modes occurs when the aircraft performs the evasive maneuver. Here a transient occurs that has a peak value of about 0.5 ft/sec. However, during the loiter, the east velocity error begins to ramp off, settling again after completion of the loiter. The peak error during this period is less than 2 ft/sec. The longitude error then follows the same characteristics as the east velocity error, but the transients are more benign due to the integration.

The structural modes also have some interesting effects on the vertical channel of the INS. The vertical velocity error experiences much larger transients from the maneuvers when structural modes are present. The largest ones are at the snap rolls and evasive maneuver. Also, during the loiter the amplitude of the transients are quite large when structural modes are present as opposed to when they are not. The vertical velocity error does however remain fairly small, with the largest transient being smaller than $\frac{1}{2}$ ft/sec. The transients of the attitude error never exceeded 20 feet while the mean remains nearly zero.

Summary. The overall effects of the structural modes on the INS performance are not good. The most significant effect of the structural modes occurs in the north velocity error. Here the structural modes cause an error of nearly 20 ft/sec. This then results in a position error of close to 4nm. These errors are much larger than the position and velocity errors caused by sensor errors. Thus, no matter how much improvement is made on the effects of the sensor errors, the sensors must be located such that the structural mode effects are minimized before a desirable level of performance can be achieved from the strapped-down INS in a high dynamic environment.

Conclusions

In this chapter, the effects of the sensor errors and the structural modes on INS performance have been assessed. The analysis reveals that the high dynamic environment results in significant degradation in the INS performance. The INS errors in local level position and velocity caused by laser gyroerrors are found not to meet the specifications of ≤ 3 ft/sec velocity error, while those caused by the accelerometer errors are within the specifications. This indicates that improvements must be made in the laser gyros and/or the methods used to sense the rotation rates. A change of gyro configuration, for example, could result in less effect from the coupling of the roll angle error into the east velocity error.

From examining the effect that structural modes have on the INS errors it is found that they produce additional degradation to that of the sensors. The most significant effect of the structural modes is the large pitch angle errors that coupled into the north velocity causing a severe error there. Also, since the errors caused by the structural modes basically added to those caused by the sensor errors, and since the gyro induced errors were larger, the location of the gyro is more critical than that of the accelerometers.

CHAPTER IV

Sensitivity of INS Errors to Sensor Errors

The sensitivity of the INS errors to changes in the values of the sensor errors are determined in this chapter. A simulation is made with each sensor error reduced to 50% of the value used for that parameter in the error analysis presented in Chapter 3. The results are then plotted against the simulation made with all sensor errors present with the parameter values as defined in Chapter two. These plots are then compared to determine the sensitivity of the INS errors to determine the sensitivity of the INS errors to each sensor error.

The results of this analysis pertaining to the laser gyro errors are presented first. Following this, the same type of analysis is presented for the quartz-flexure accelerometer.

Sensitivity to Laser Gyro Errors

The plots in Figure 22 show the effects of reducing the laser gyro bias error by 50%. The curve labeled with a circle represents simulation results with all laser gyro errors present, while the curve labeled with a triangle represents the results with no laser gyro errors. The third curve, labeled with a square, is the results obtained with all laser gyro errors present, but the bias error at a value of 50% less than the one used in previous simulations ($0.005^\circ/\text{hr}$).

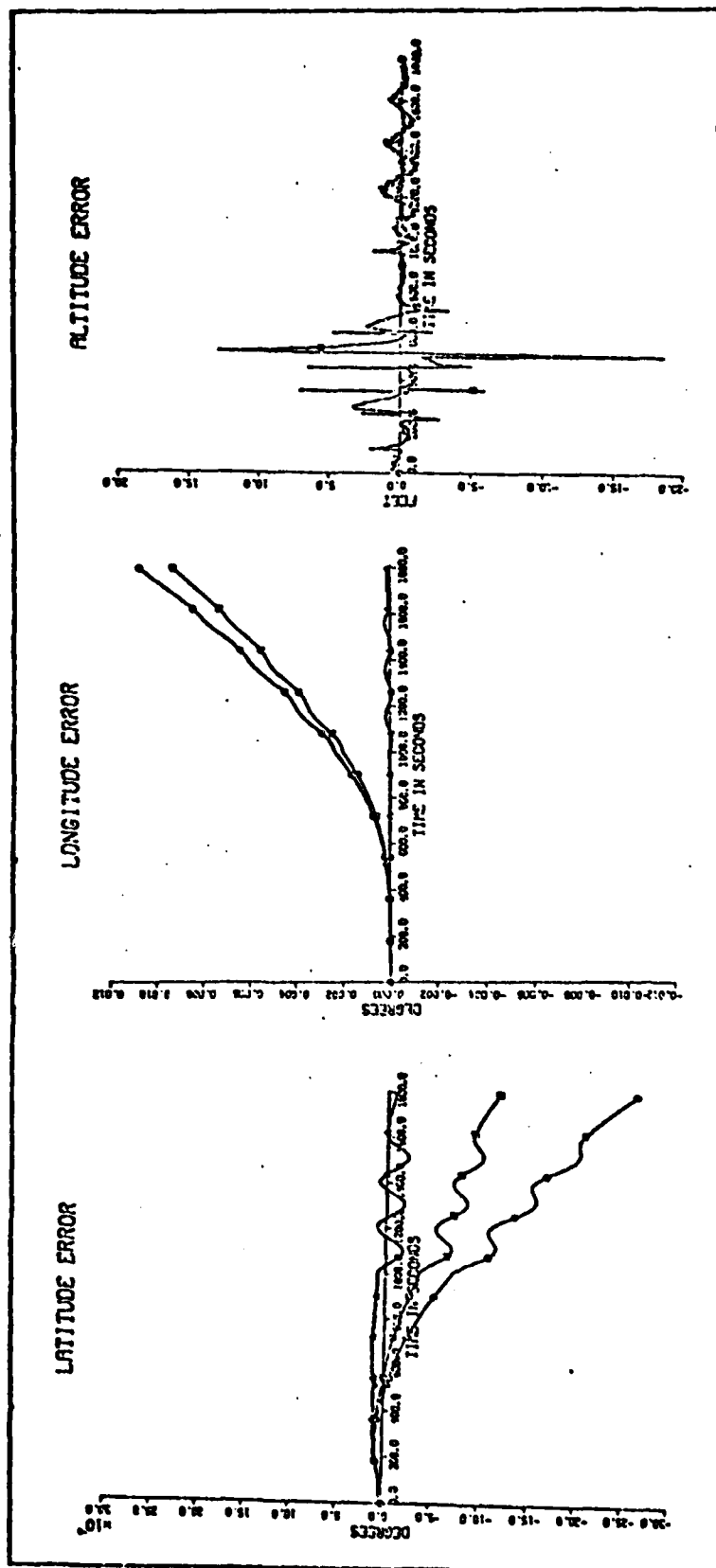


Figure 22a. Comparison of Position Errors for Cases of All Laser Gyro Errors at Full Value, Gyro Bias Error at 50% Value, and all Ideal Sensors

- Case with only bias error at 50% value.
- Case with gyro errors at full value.
- △ Case with all ideal sensors.

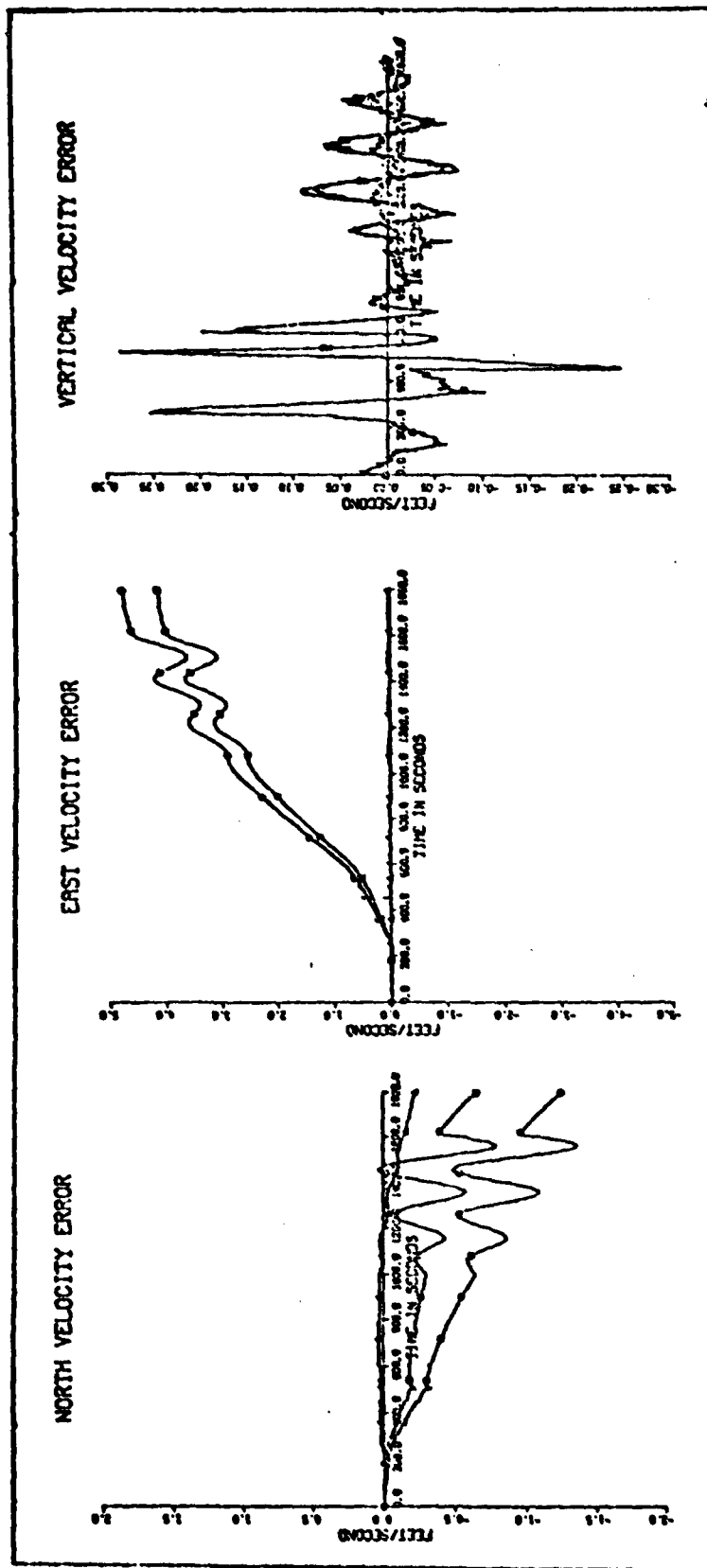


Figure 22b. Comparison of Velocity Errors for Cases of All Laser Gyro Errors at Full Value, Gyro Bias Error at 50% Value, and all Ideal Sensors

- Case with only bias error at 50% value.
- Case with gyro errors at full value.
- △ Case with all ideal sensors.

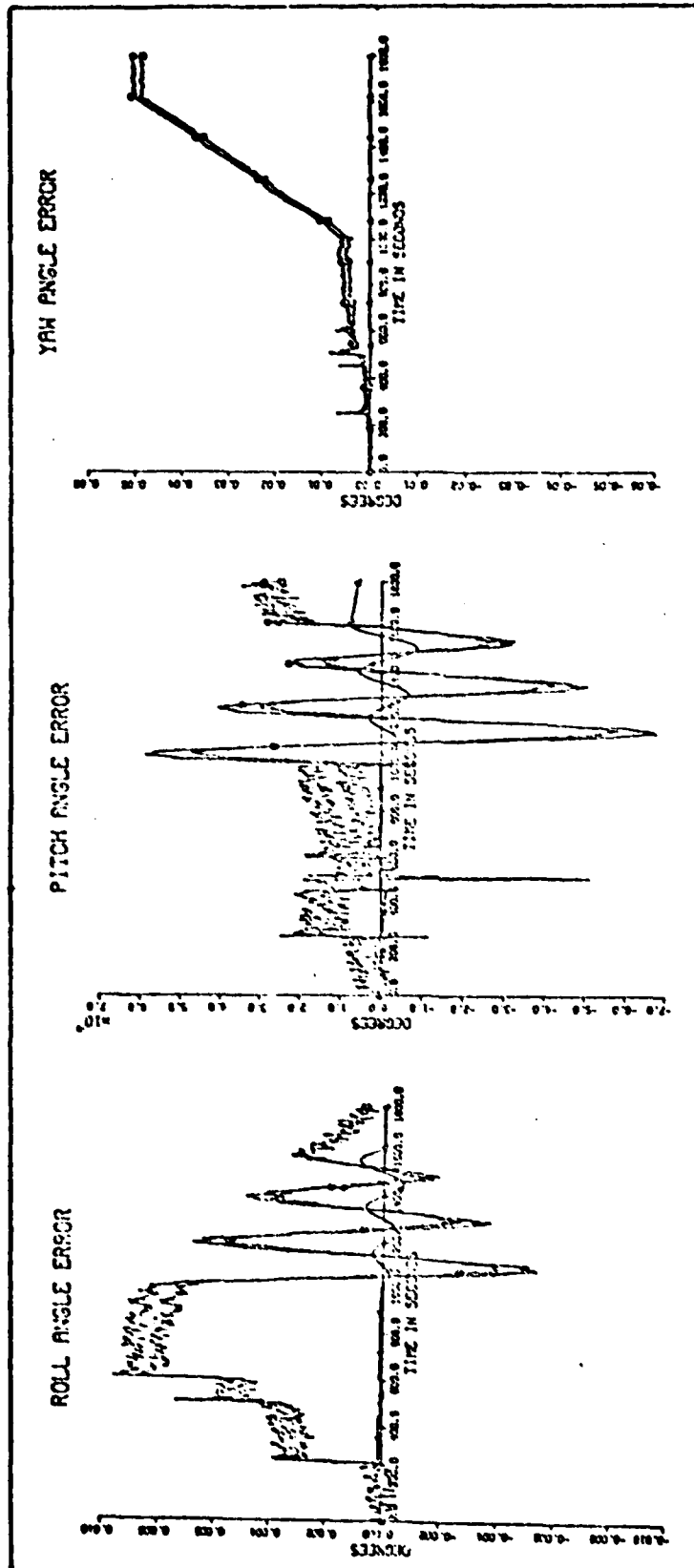


Figure 22c. Comparison of Attitude Errors for Case of All Laser Gyro Errors at Full Value, Gyro Bias Error at 50% Value, and all Ideal Sensors

- Case with only bias error at 50% value.
- Case with gyro errors at full value.
- △ Case with all ideal sensors.

THIS PAGE IS NOT QUALITY PHOTOGRAPHED
FROM THE ORIGINAL, AND IS NOT TO BE USED

Recalling the analysis of chapter three in regards to the bias error, it should be expected that a change in the value of bias error should have little effect on the yaw angle error. This, indeed, is the case. The 50% reduction in bias error resulted in a nearly negligible reduction in yaw angle error. However, the step errors in the roll angle are slightly reduced and since the steps are additive, additional improvement over the results obtained with the $0.01^{\circ}/\text{hr}$ bias error are obtained at each snap roll and the evasive maneuver. This results in about a 10% improvement in the roll angle error at the point where the loiter begins. During the loiter, the effects of misalignment became dominant and negligible improvement is gained by a 50% reduction in bias error. The pitch angle error shows the most improvement of all the Euler angles with the reduction in bias error. It too however, is not greatly improved, except during climb. During this phase of the flight the 50% reduction in bias error results in a 50% reduction in pitch angle error.

This is a good illustration of the fact that the effects of the bias error are less sensitive to high dynamic maneuvers than those of the other gyro errors.

With the yaw and roll angle errors being only slightly reduced, the east velocity error has a small reduction in the value of its slope. By the end of the 30 minute flight, this has resulted in a reduction of the error by 0.6 ft/sec. This indicates that the specification of ± 3 ft/sec position error could not be reached by simply reducing the bias error.

This small improvement in east velocity error results in an improvement in the longitude error of 0.0018° , which is not enough to bring it to within the specification $\pm 1\text{nm/hr}$.

As is found in the analysis of chapter three, the bias error results in most of the north velocity error when all errors of the laser gyro are present. This indicates that the north velocity error should be quite sensitive to bias error changes. As seen in Figure 22, this is indeed the case. The slope of the north velocity error is reduced such that, by the end of the 30 minute flight, it is almost half of the value that is achieved with a $0.01^{\circ}/\text{hr}$ bias error. This brought the value of the error down to about -0.6 ft/sec after 30 minutes of flight, therefore the 3 ft/sec velocity error specification should easily be reached.

This improvement in the north velocity error is passed on to the latitude error. After 30 minutes of flight, the latitude error is -0.0012 degrees or 0.072 nm . This, too, should easily remain within the specification of 1 nm/hr position error.

Since the vertical channel proved to be relatively unaffected by sensor errors, improvements in the sensor errors have little or no effect on the altitude and altitude rate errors.

Laser Gyro Misalignment Error

From the analysis of chapter three, the misalignment error is found to effect the yaw and roll angle errors and the east velocity error more than the other sensor errors.

Figure 23 compares the INS time histories achieved with the misalignment error at 5×10^{-5} radians. The yaw angle error is reduced by nearly 50%, while the pitch angle is hardly effected. The roll angle experiences improvements at the points where the misalignment error introduces steps into it. This occurs at the snap rolls and the evasive maneuver. The improvement that results is about a 50% reduction in the amount of step error caused by the misalignment error. This results in the roll angle error being reduced by this amount at each of the snap rolls, and while, at the evasive maneuver, the roll angle error is cut in half. However, during the loiter, this improvement is reduced such that by the end of the flight there is no more improvement. Once again, this illustrates the fact that the misalignment error is much more sensitive to aircraft maneuvers than the bias error.

Since the yaw and roll angle errors couple into the east velocity, by the end of the 30 minute flight, the slope change has resulted in the velocity error being reduced by about 2 ft/sec. This puts it just within the specification that is used for this study. The east velocity improvement integrates into an improvement in the longitude error. This improvement is about 0.005 degrees or 0.3 nautical miles. This should be enough of an improvement to keep the latitude error less than 1 nm/hr.

Since the misalignment error is found to have little effect on north velocity and latitude errors, little sensitivity to gyro misalignment error is expected. The simulation

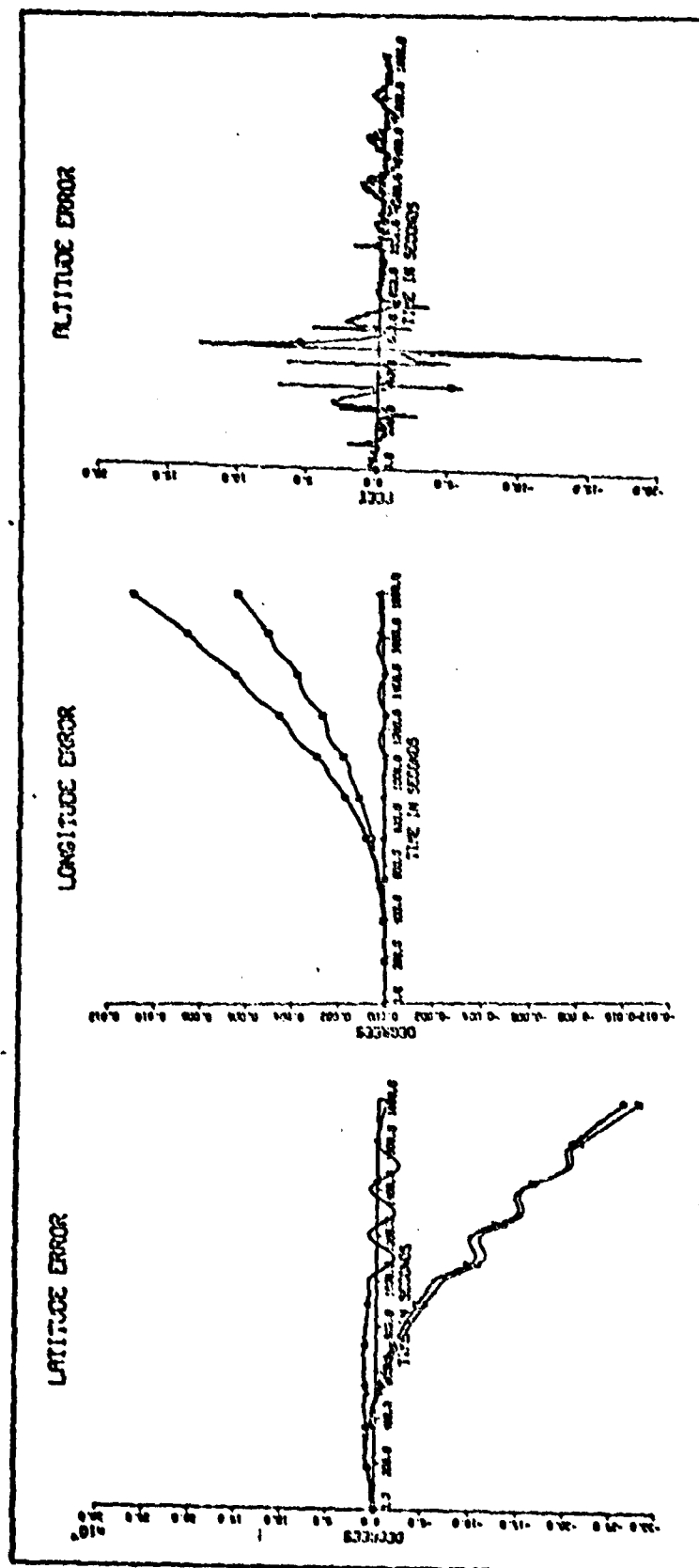


Figure 23a. Comparison of Position Errors for Cases of All Laser Gyro Errors at Full Value, Gyro Misalignment at 50% Value, and all Ideal Sensors

- Case with misalignment error reduced 50%.
- Case with laser gyro errors at full value.
- △ Case with all ideal sensors.

THIS PAGE IS NOT QUALITY PRINTED

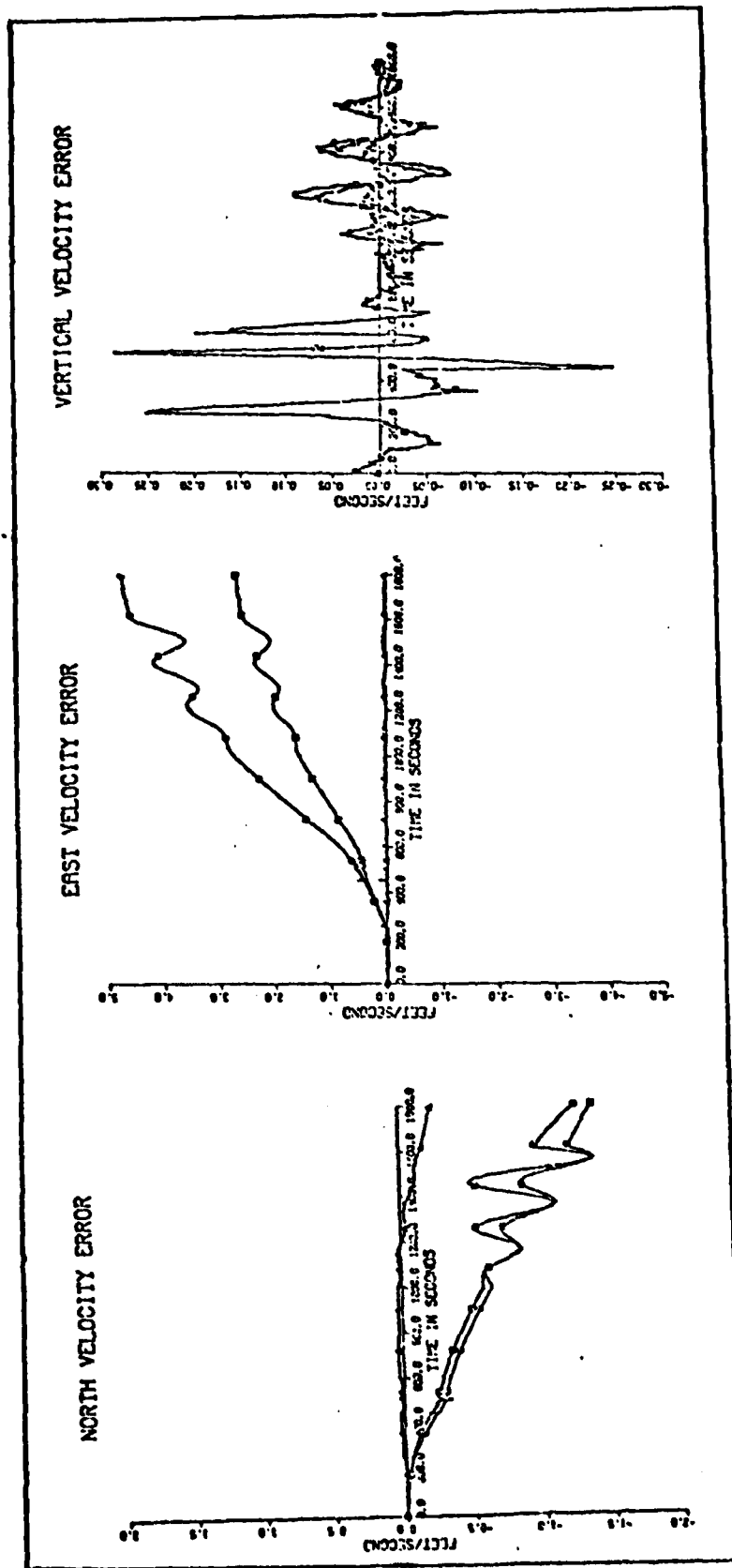


Figure 23b. Comparison of Velocity Errors for Cases of All Laser Gyro Errors at Full Value, Gyro Misalignment at 50% Value, and all Ideal Sensors

- Case with misalignment error reduced 50%.
- Case with laser gyro errors at full value.
- △ Case with all ideal sensors.

THIS PAGE IS BEST QUALITY PRINTING
 THE QUALITY OF THIS PAGE IS BEST QUALITY PRINTING

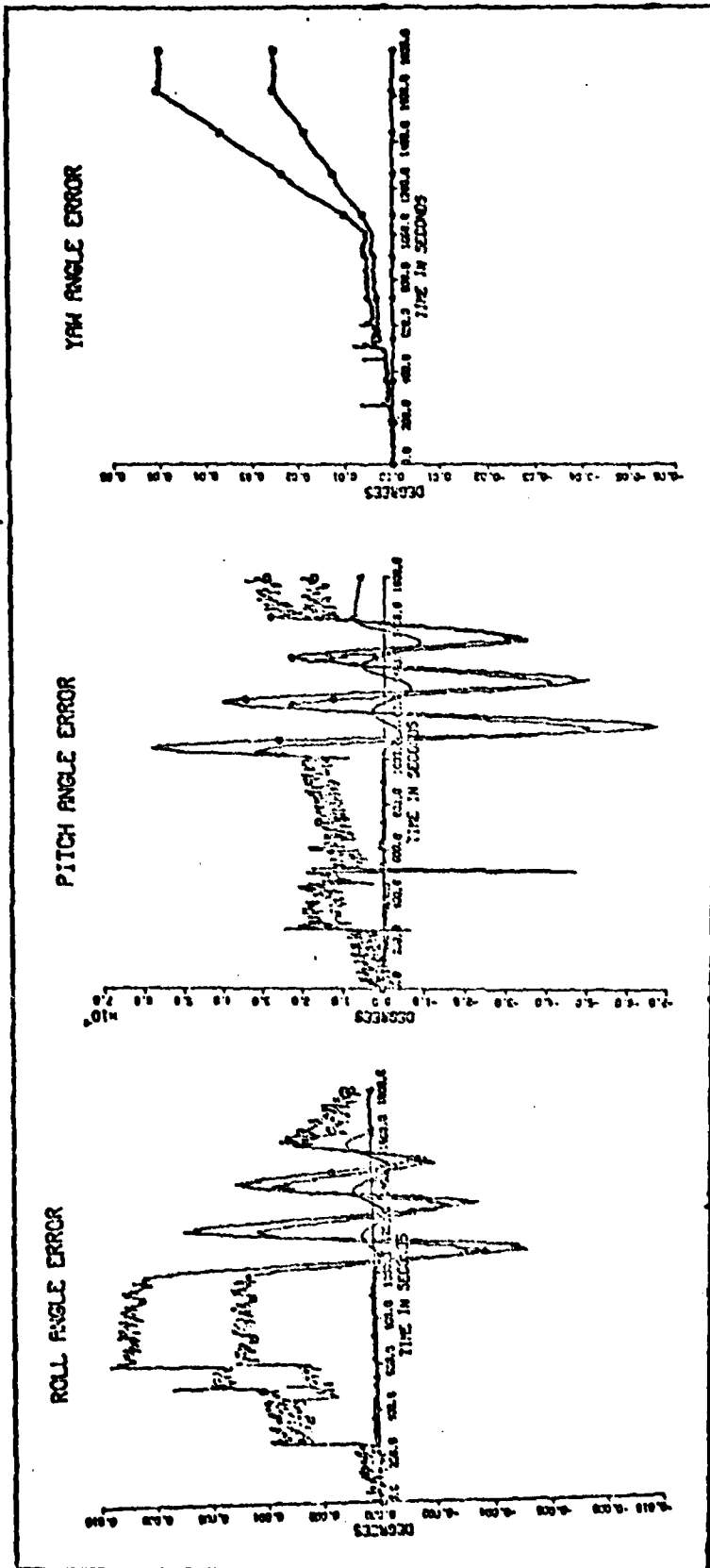


Figure 23c. Comparison of Attitude Errors for Cases of All Laser Gyro Errors at Full Value, Gyro Misalignment at 50% Value, and all Ideal Sensors.

- Case with misalignment error reduced 50%.
- Case with laser gyro errors at full value.
- △ Case with all ideal sensors.

THIS PAGE IS BEST QUALITY PRINTING

results obtained with the misalignment error reduced 50% verify this idea. The improvement in north velocity error is less than 0.25 ft/sec, while the latitude error is only reduced by 10^{-4} degrees (6×10^{-3} nautical miles).

Laser Gyro Scale Factor Error

Unlike the bias and misalignment errors, the scale factor error is not a dominant force in any of the INS errors. However, it does account for about $\frac{1}{3}$ of the step error size in the roll angle error and has about the same effect as the bias error or yaw angle error. These effects couple into local level velocity and position errors, with more effect being on the east than the north velocity. As can be seen in Figure 24, when the scale factor error is reduced by 50%, improvements are noticable in both the yaw and roll angles and these improvements help to reduce the local level velocity and position errors.

The improvements in the yaw angle error are small when compared with the overall yaw angle error, but the improvements in roll angle error are substantial during the snap rolls and evasive maneuvers. Since both the roll and yaw angle errors couple into the east velocity error, the reduction of scale factor error results in almost 2 ft/sec improvement in east velocity error by the end of the 30 minute flight. This translates into a longitude error of 0.004 degrees (0.24 nautical miles).

The improvements in the north velocity and latitude errors are not as substantial since the roll angle does

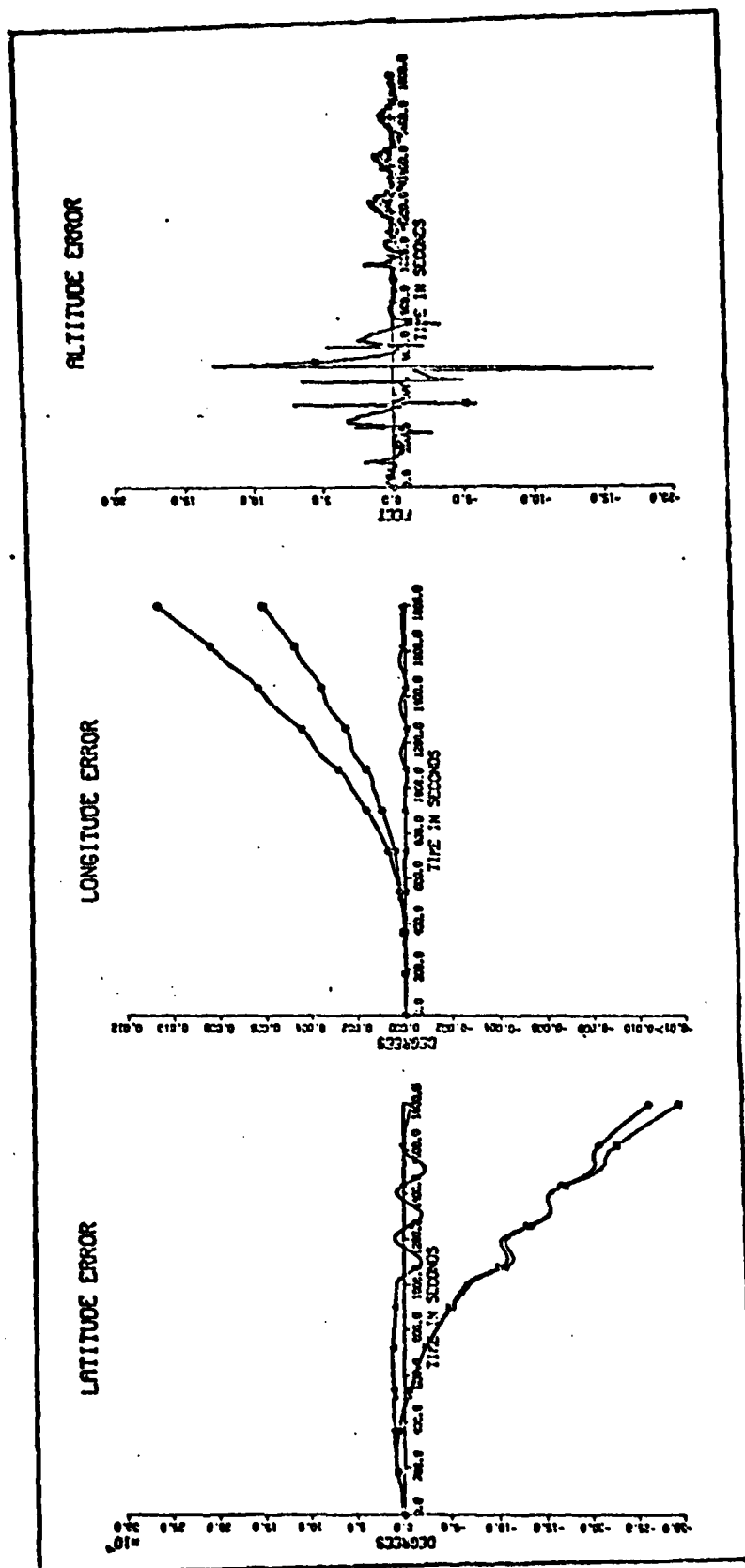


Figure 24a. Comparison of Position Errors for Cases of All Laser Gyro Errors at Full Value, Gyro Scale Factor Reduced 50%, and All Ideal Sensors.

- Case with gyro scale factor reduced 50%.
- Case with gyro errors at full value.
- △ Case with all ideal sensors.

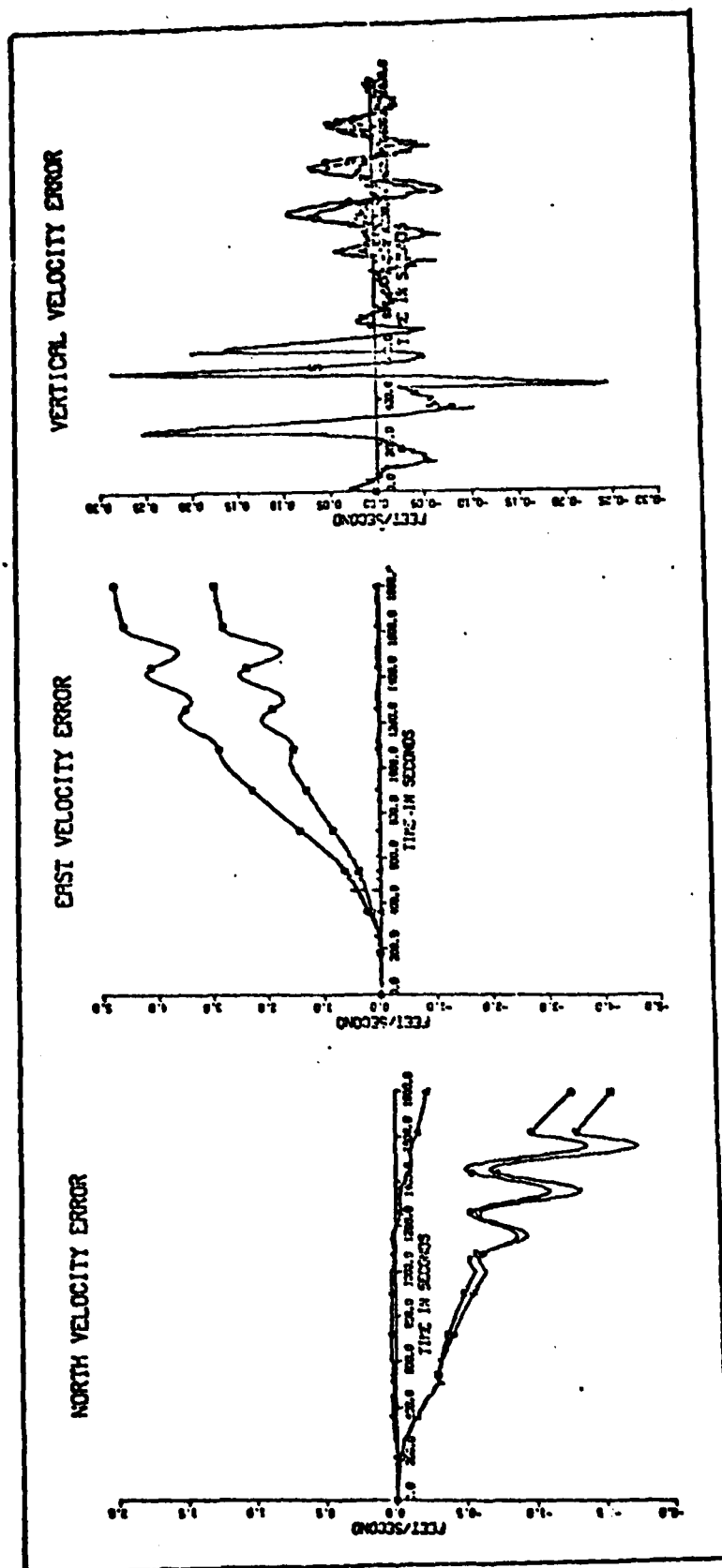


Figure 24b. Comparison of Velocity Errors for Cases of All Laser Gyro Errors at Full Value, Gyro Scale Factor Reduced 50%, and All Ideal Sensors.

- Case with gyro scale factor reduced 50%.
- Case with gyro errors at full value.
- △ Case with all ideal sensors.

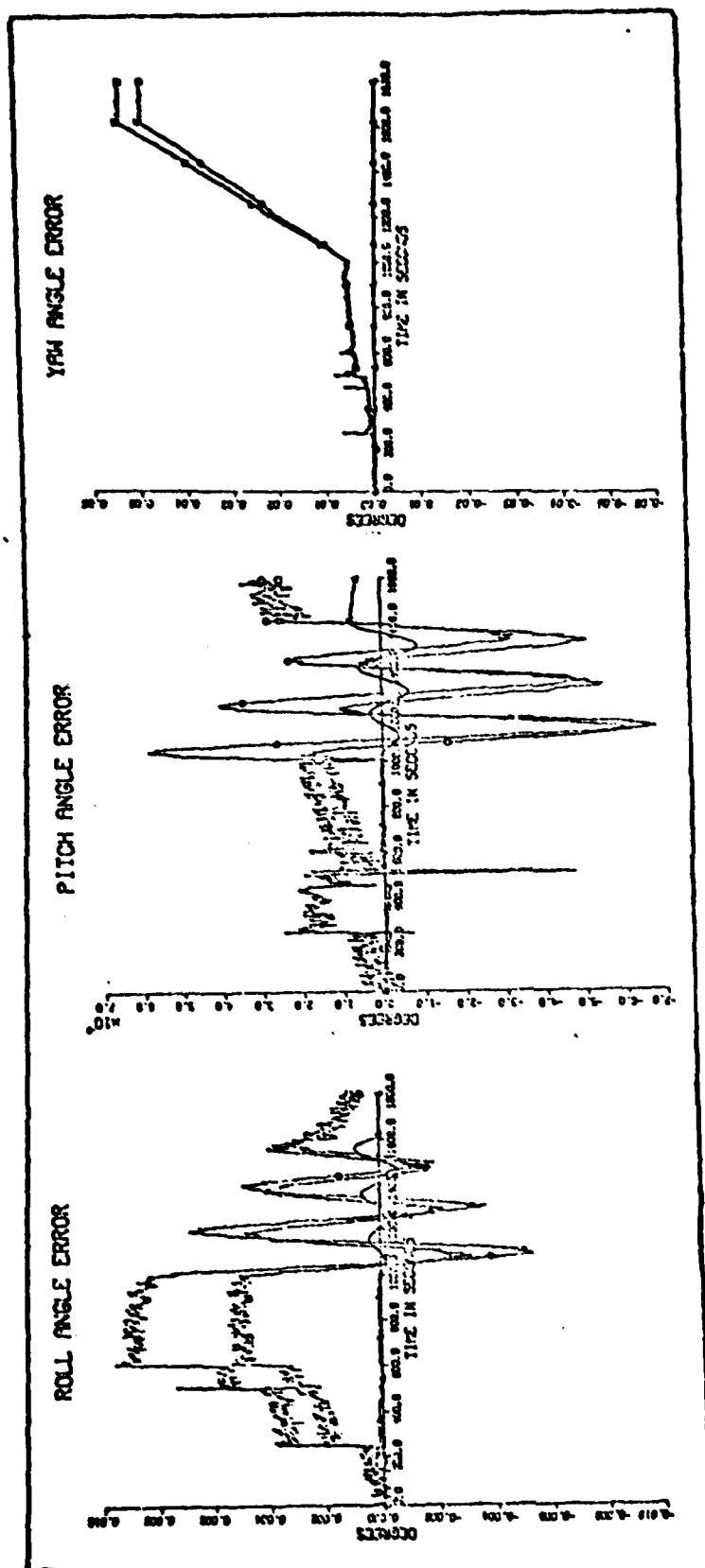


Figure 24c. Comparison of Attitude Errors for Cases of All Laser Gyro Errors at Full Value, Gyro Scale Factor Reduced 50%, and All Ideal Sensors.

- Case with gyro scale factor reduced 50%.
- Case with gyro errors at full value.
- △ Case with all ideal sensors.

not couple into these errors. The slight decrease in yaw angle error, however, does reduce the slope of the north velocity error resulting in a 0.25 ft/sec reduction of its value. This improvement results in a 2.5×10^{-4} degree reduction in the latitude error.

Laser Gyro Random Walk Error

As should be expected after the analysis of Chapter three, improvement in the random walk error does little to improve the INS errors. Looking at the graphs in Figures 25, the curves plotted with all sensor errors at the values specified in Table 2 are not distinguishable from those obtained when the random walk was at 50% of this value (0.0025 degrees/hr).

Summary of Sensitivity to Laser Gyro Errors. Having determined the sensitivity of each individual laser gyro error, an 84 minute simulation is made with all gyro errors reduced 50%. Figure 26 shows the results that are obtained. As should be expected, since it has third order damping, the vertical channel is relatively insensitive to changes in the gyro error parameters. However, all other INS errors show about a 50% reduction as a result of reducing the sensor errors by 50%. Table 4 has a listing of the amount by which each INS error is reduced when a given gyro error is reduced by 50%. As can be seen, the results for the case of reducing all gyro errors is not the summation of the case of reducing all gyro errors is not the summation of the cases of reducing the gyro errors individually. This

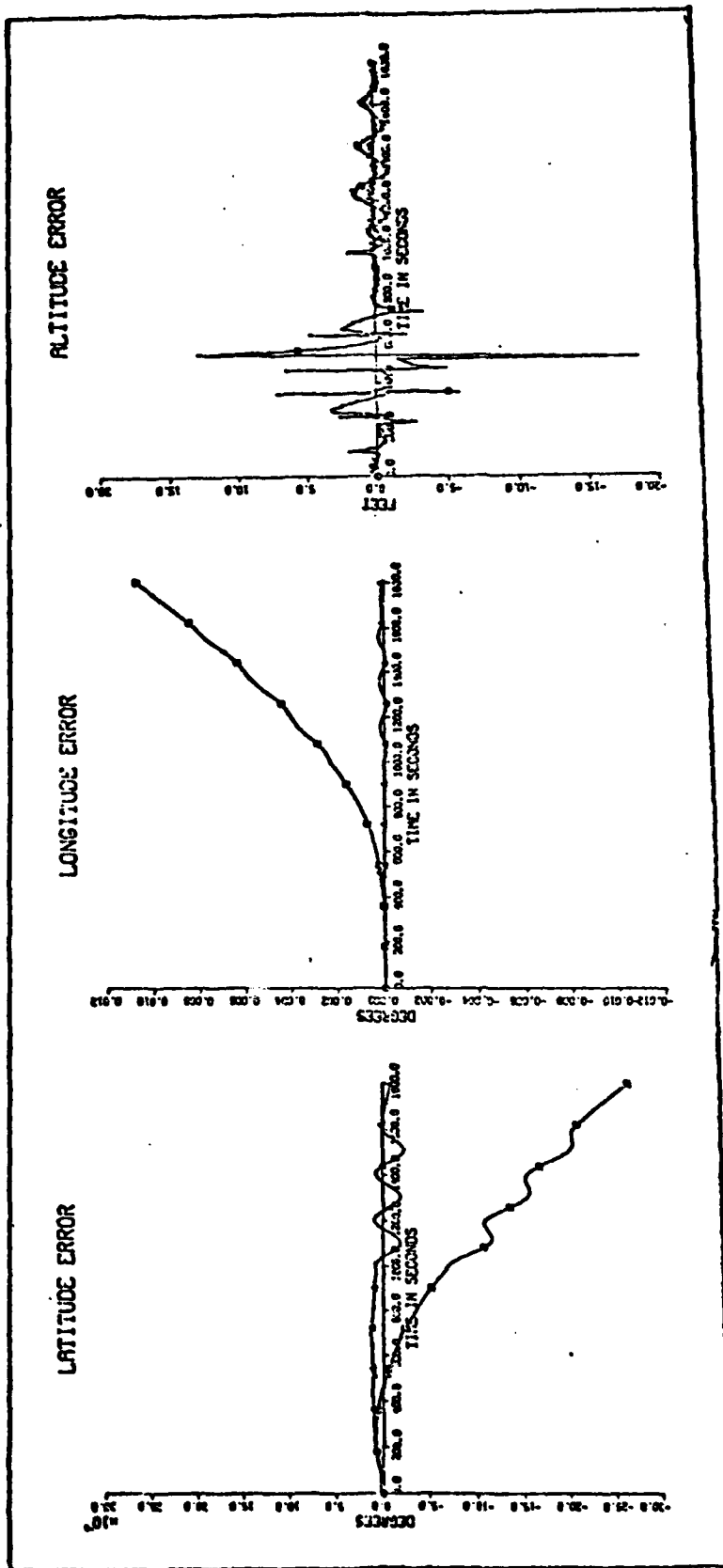


Figure 25a. Comparison of Position Error for Cases of All Laser Gyro Errors at Full Value, Gyro Random Walk Reduced 50%, and All Ideal Sensors

- Case with gyro random walk reduced 50%.
- Case with gyro errors at full value.
- △ Case with all sensors ideal.

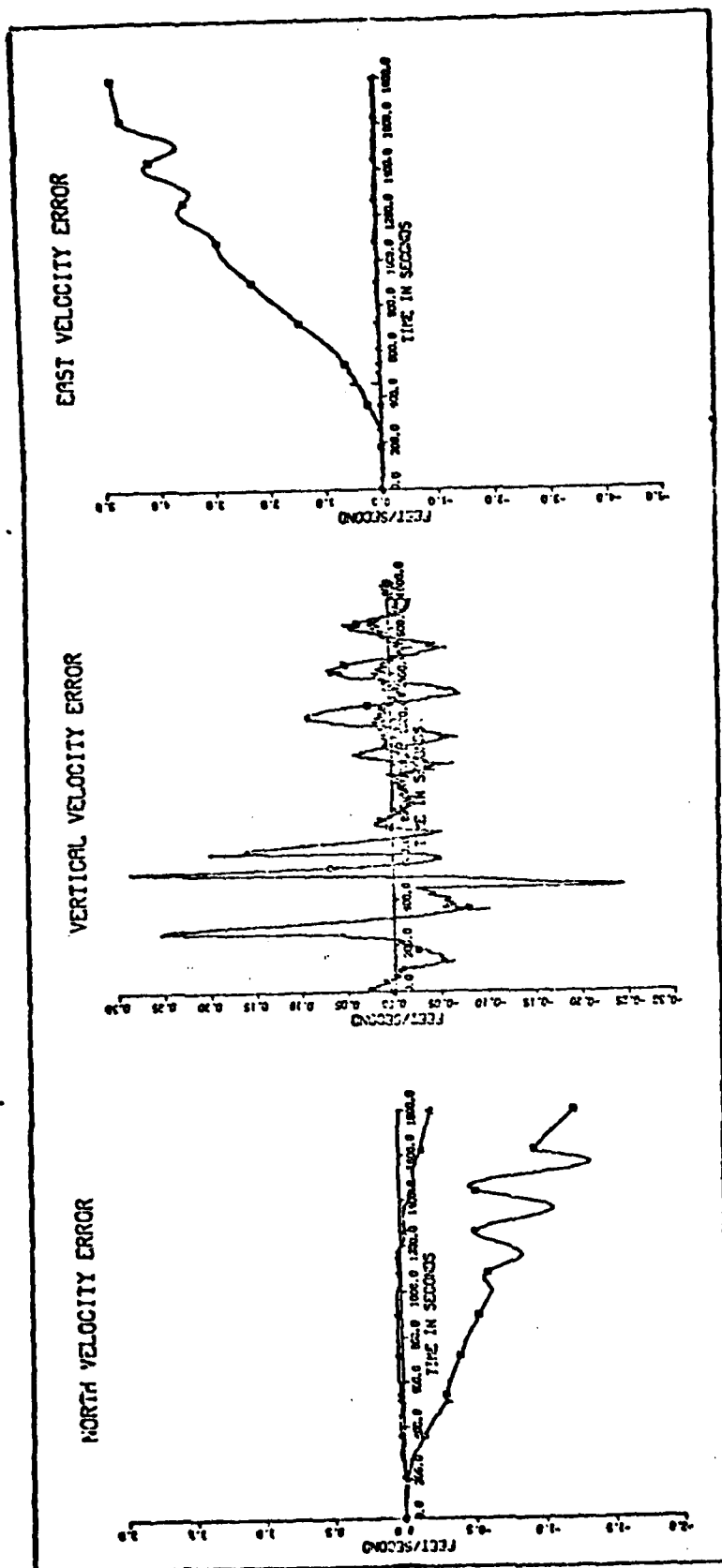


Figure 25b. Comparison of Velocity Error for Cases of All Laser Gyro Errors at Full Value, Gyro Random Walk Reduced 50%, and All Ideal Sensors

- Case with gyro random walk reduced 50%.
- Case with gyro errors at full value.
- △ Case with all sensors ideal.

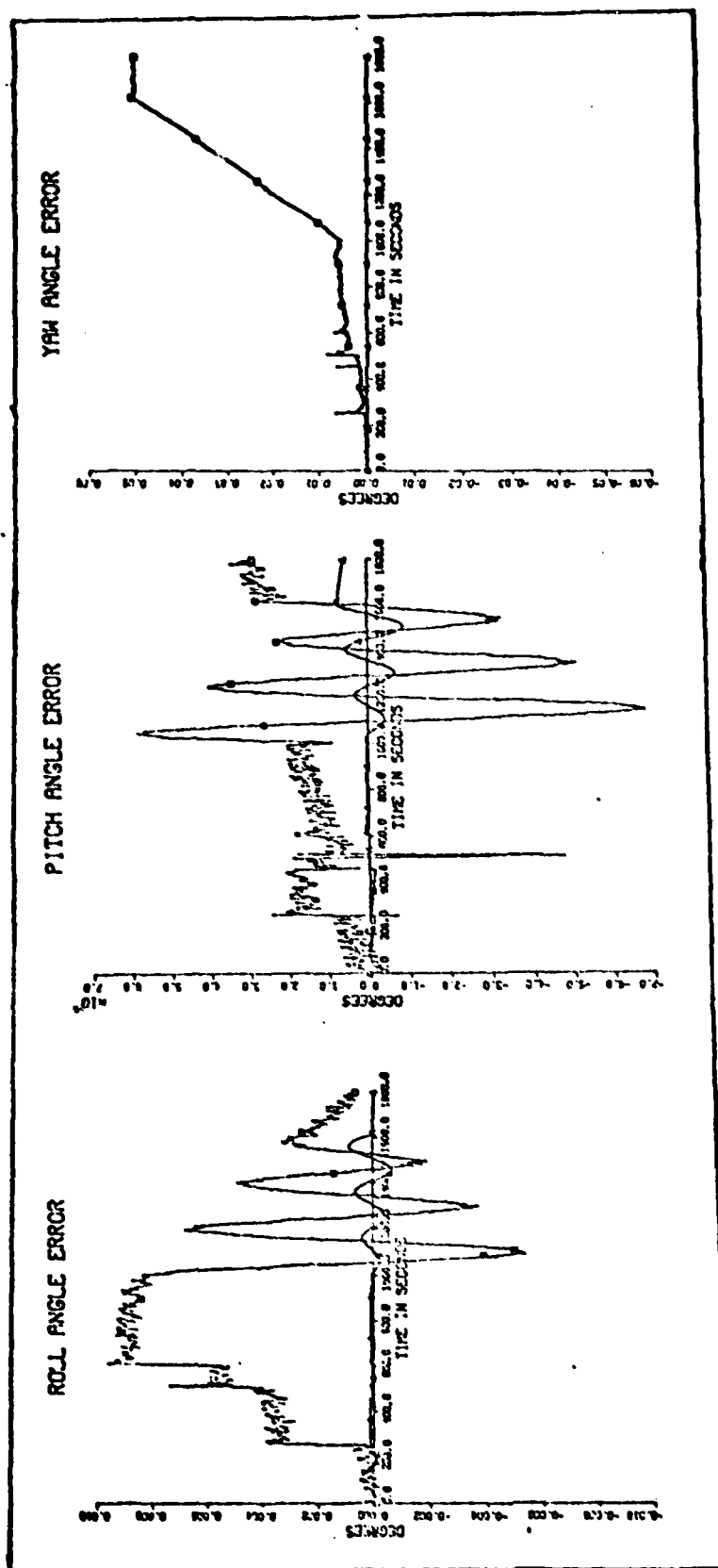


Figure 25c. Comparison of Attitude Error for Cases of All Laser Gyro Errors at Full Value, Gyro Random Walk Reduced 50%, and All Ideal Sensors

- Case with gyro random walk reduced 50%.
- Case with gyro errors at full value.
- △ Case with all sensors ideal.

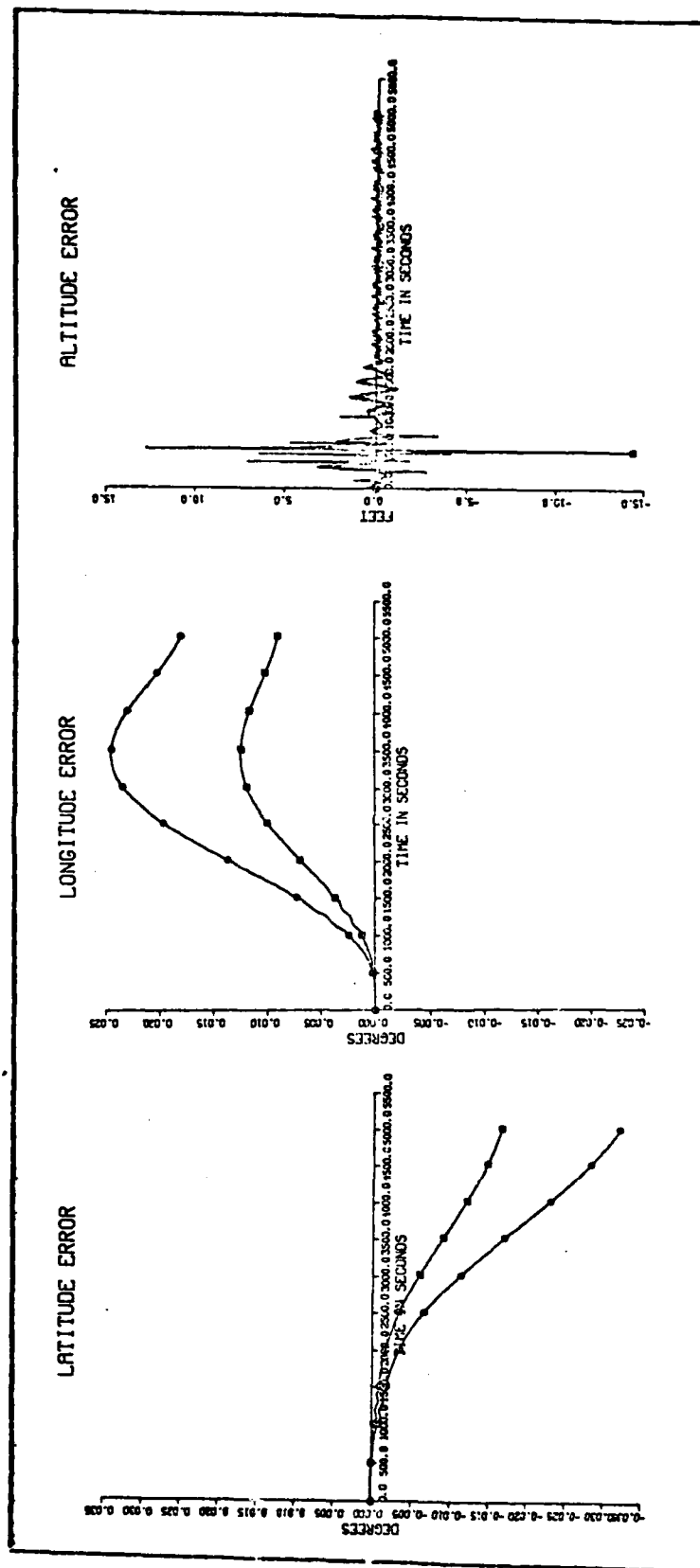


Figure 26a. Comparison of Position Error for Cases of All Laser Gyro Errors at Full Value, and All Reduced 50%.

☐ Case with all reduced 50%.
 Case with all at full value.

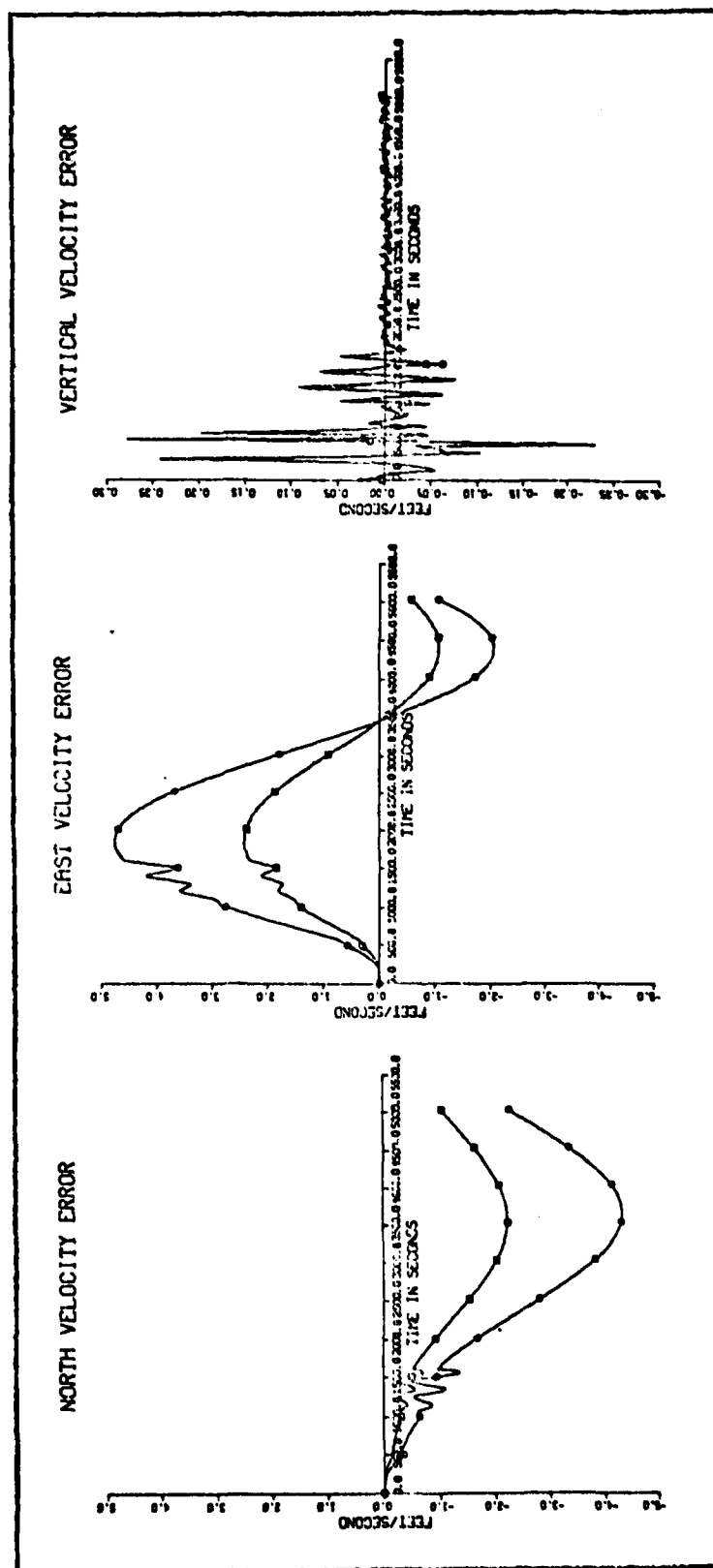


Figure 26b. Comparison of Velocity Error for Cases of All Laser Gyro Errors at Full Value, and All Reduced 50%

- Case with all reduced 50%.
- Case with all at full value.

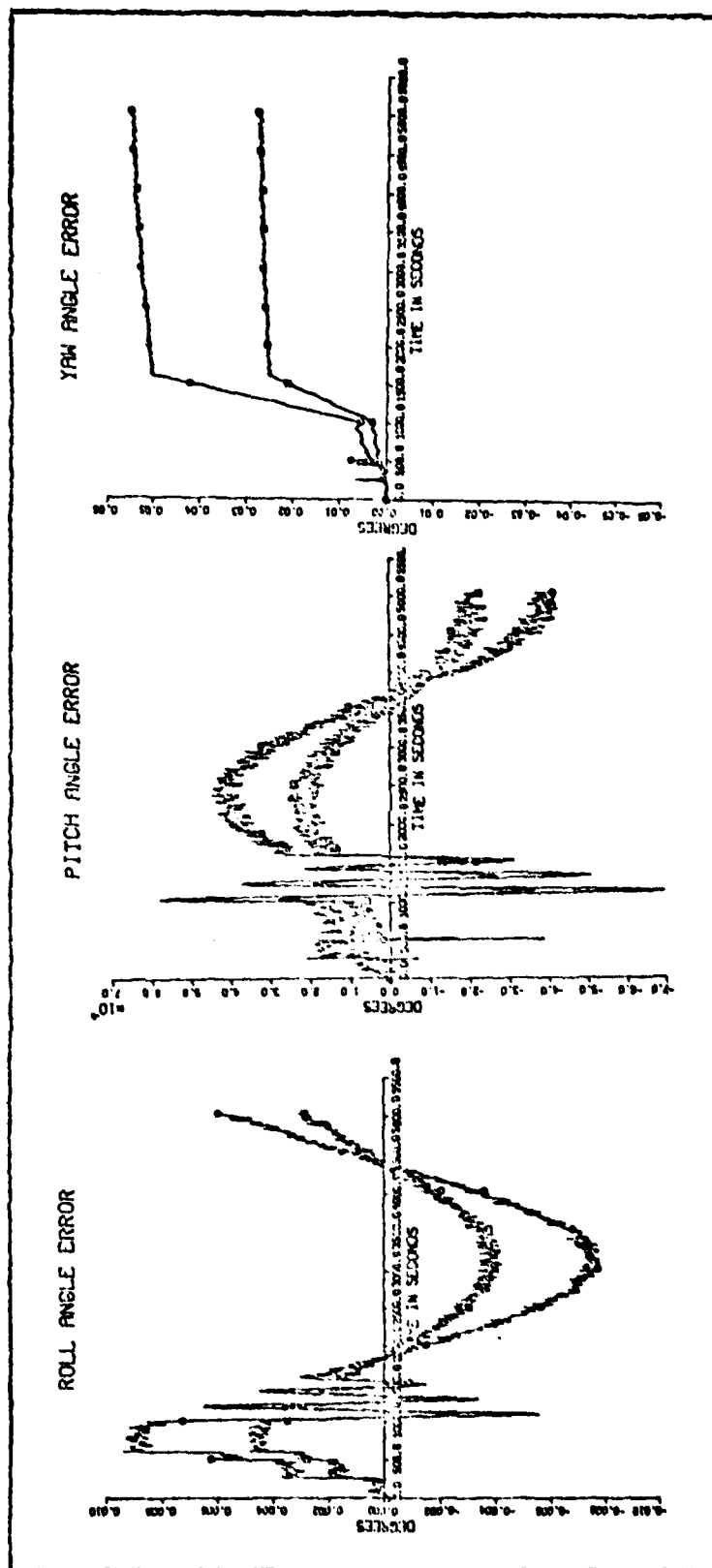


Figure 26c. Comparison of Attitude Error for Cases of All Laser Gyro Errors at Full Value, and All Reduced 50%

- ☐ Case with all reduced 50%.
- ☐ Case with all at full value.

TABLE IV

Sensitivity to Laser Gyro Error

INS Error	Bias	Misalignment	Scale Factor	Random Walk	All
Longitude	12.3%	41.3%	43.2%	0%	49.5%
Latitude	56.4%	5.5%	4.5%	0%	54.5%
Altitude	0%	0%	0%	0%	0%
North Velocity	51.1%	7.4%	7.4%	0%	44.4%
East Velocity	10.5%	42.0%	36.8%	0%	47.4%
Vertical Velocity	0%	0%	0%	0%	0%

The values shown are the percent change in the INS error for a 50% in the indicated Laser Gyro Error after 30 minutes of flight using the flight profile given in chapter 2.

to be expected since the Euler angle errors, which are directly related to gyro errors, create errors in the accelerometer measurements which do not necessarily have the same sign. This indicates that the effects of the gyro errors can be overlapping or offsetting to some extent depending upon the direction of the acceleration along a given axis.

The simulations presented in this chapter clearly show that the INS errors are quite sensitive to the laser gyro errors when structural modes are not sensed. Table 4 shows the results of the sensitivity tests. Examining the figures presented, it is seen that the east velocity and thus the longitude would be greatly reduced by a decrease in either the scale factor error or the misalignment error, while a reduction in north velocity and latitude requires an improvement in the bias error. Since the east velocity and longitude errors are found to be the worst, the misalignment and scale factor errors should be given more attention than the bias error.

Sensitivity to Accelerometer Errors

A similar analysis to that presented on the sensitivity of INS errors to laser gyro errors is now presented for the accelerometer.

Accelerometer Bias Error. The INS error time histories obtained with the accelerometer bias error reduced to 50% are shown in Figure 27. As is shown in Chapter three, the

accelerometer errors effect the velocity errors directly. When the bias error is reduced 50%, the north velocity error, after the 30 minute flight, is reduced by only a small amount. However, just before the loiter maneuver is begun the smaller bias error provides a noticable decrease in the north velocity error, (about 27%), which is passed on to the latitude error in the form of a ramp of reduced slope. This results in a reduction in the latitude error of about the same amount. About the same amount of improvement in the pitch angle error should be expected and indeed this is the case.

Since the bias error causes a large east velocity and longitude error that is offset by the effects of the misalignment and scale factor error, reducing the bias error by 50% results in a large error (10 times that with all errors at full value for the east velocity and 8 times that with all errors for longitude) in these two INS parameters. However, this error is the negative of that produced when only the bias error is present since it is due to the other accelerometer gyro errors. This indicates that if the accelerometer errors are to be reduced, the reduction in the bias error must be a comparable reduction in the other accelerometer errors.

Accelerometer Misalignment Error. The misalignment error has the same type of effect on the INS errors as the bias error except that the effect on the east velocity and longitude are opposite in sign and about 1/6 of the magnitude as those of the bias error. As seen in Figure 28, this results in the north velocity and latitude errors having about the same sensitivity to misalignment error as they do to bias error, 27%. The east velocity and longitude errors are

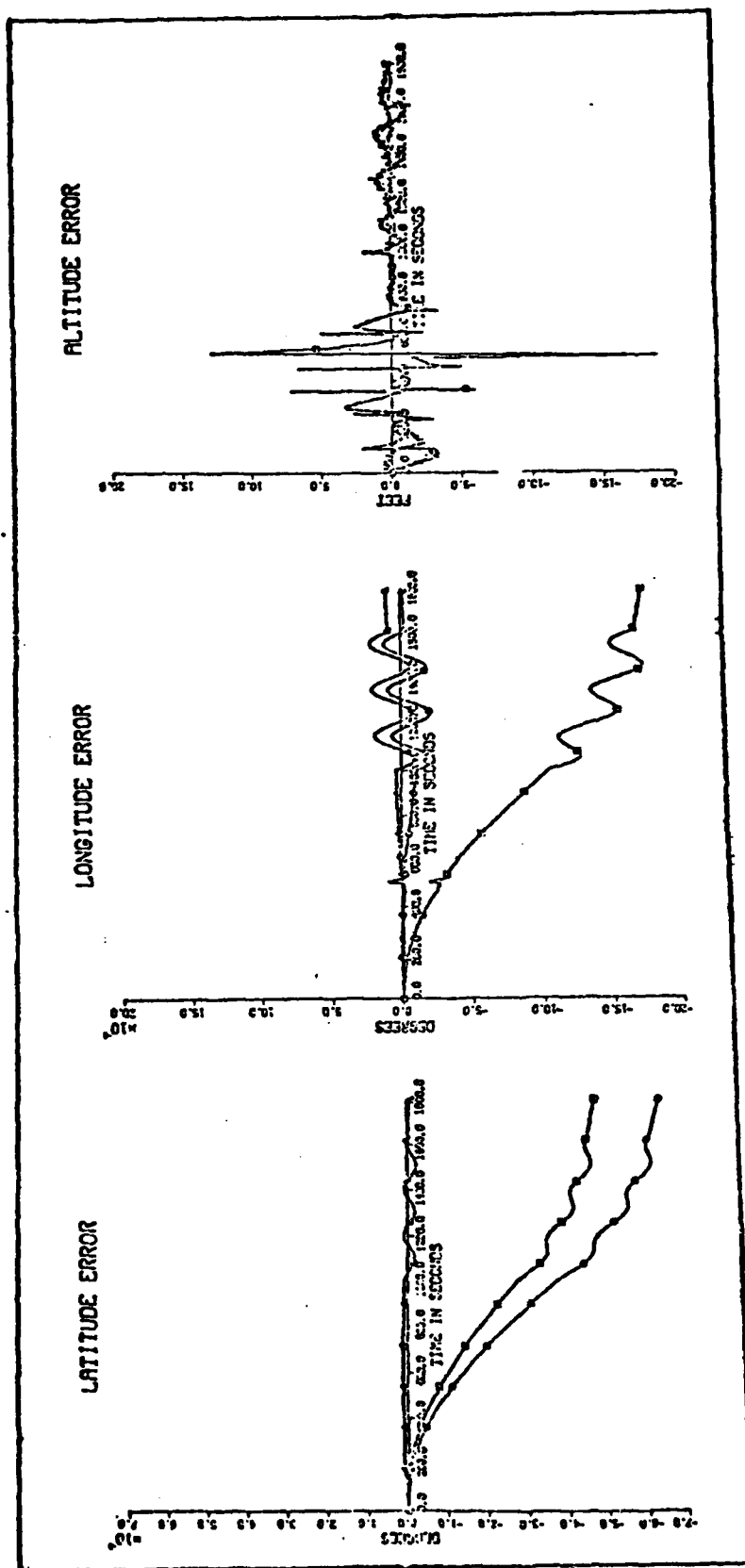


Figure 27a. Comparison of Position Errors for Cases of All Accelerometer Errors at Full Value, Accelerometer Bias Reduced 50%, and All Ideal Sensors

- Case with accelerometer bias error reduced 50%.
- Case with accelerometer errors at full value.
- △ Case with all ideal sensors.

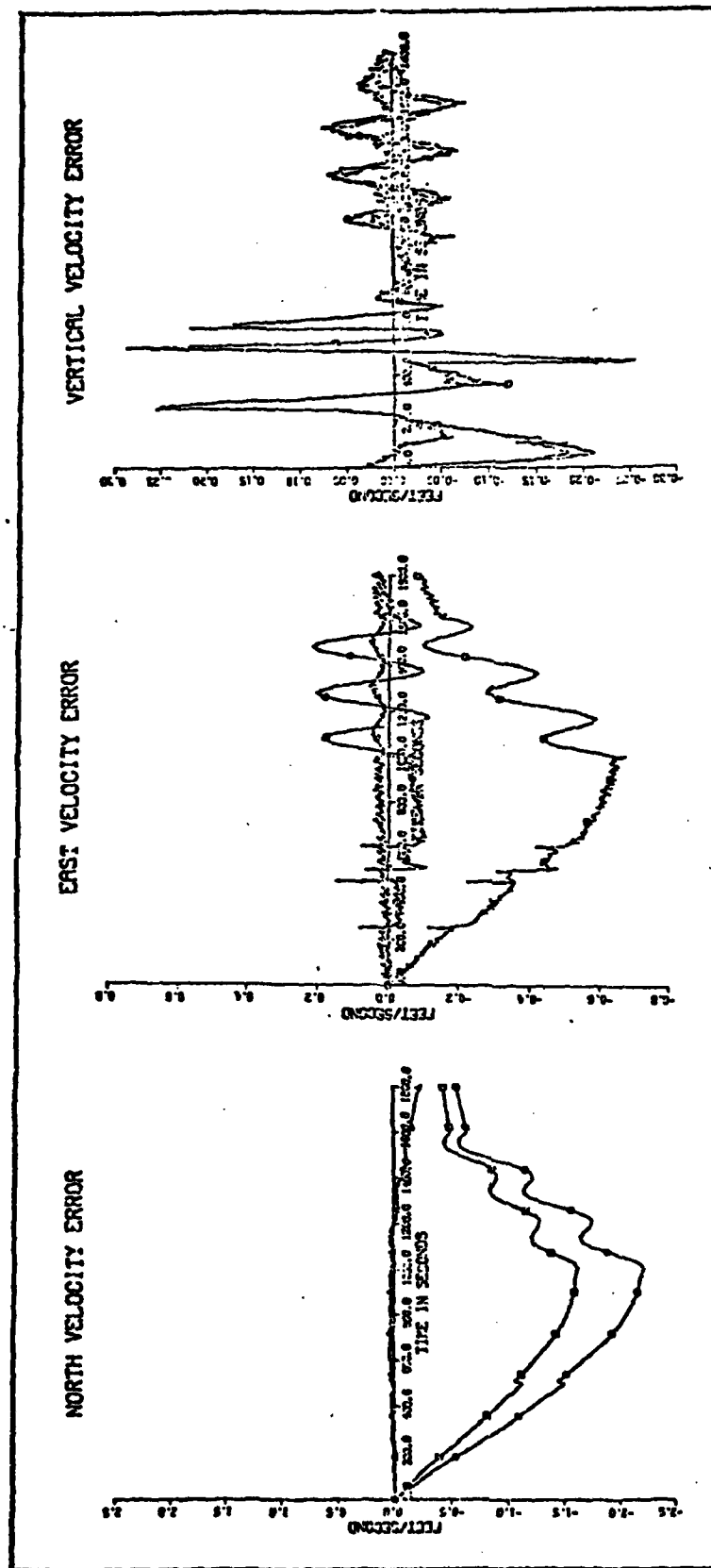


Figure 27b. Comparison of Velocity Errors for Cases of all Accelerometer Errors at Full Value, Accelerometer Bias Reduced 50%, and all Ideal Sensors

- Case with accelerometer bias error reduced 50%.
- Case with accelerometer errors at full value.
- △ Case with ideal sensors.

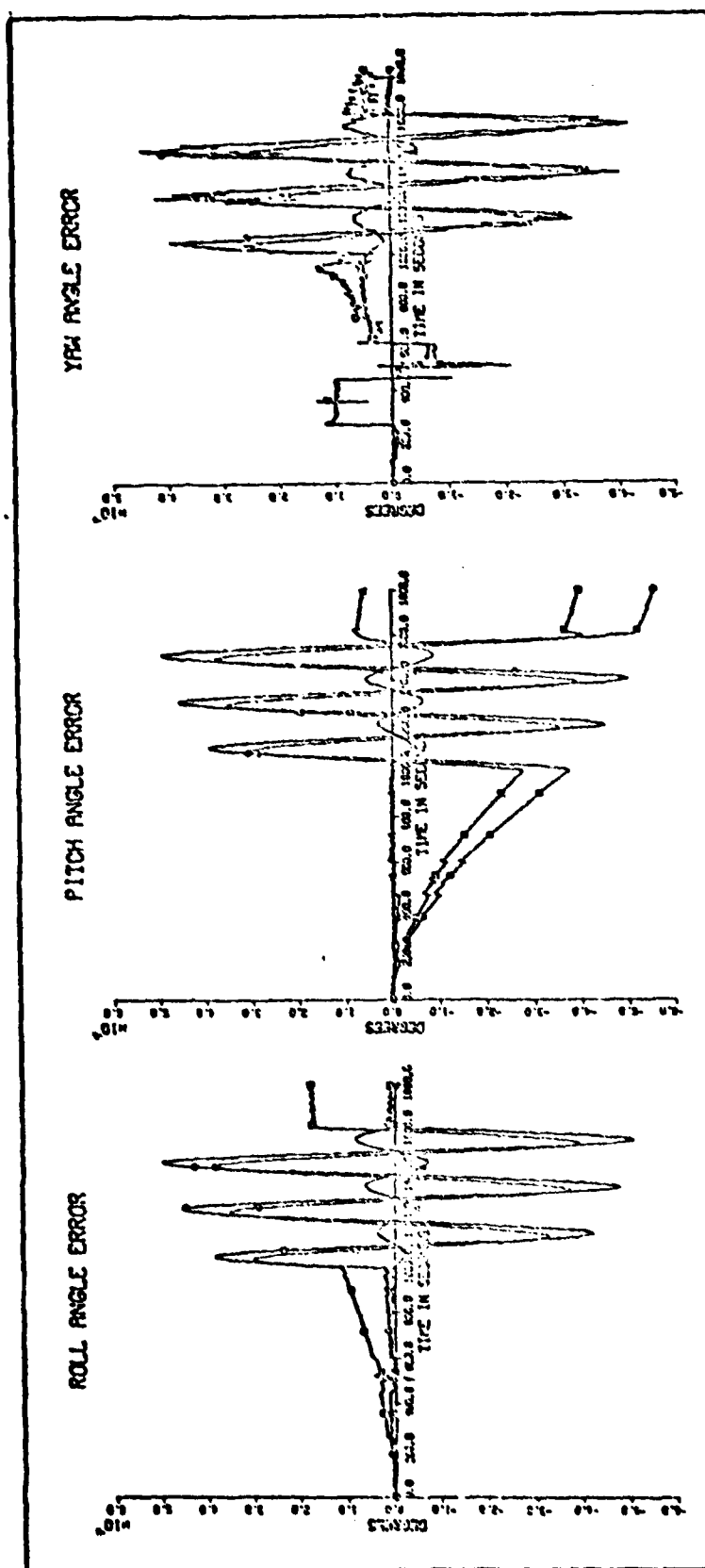


Figure 27c. Comparison of Attitude Errors for Cases of all Accelerometer Errors at Full Value, Accelerometer Bias Reduced 50%, and all Ideal Sensors

- Case with accelerometer bias error reduced 50%.
- Case with accelerometer errors at full value.
- △ Case with ideal sensors.

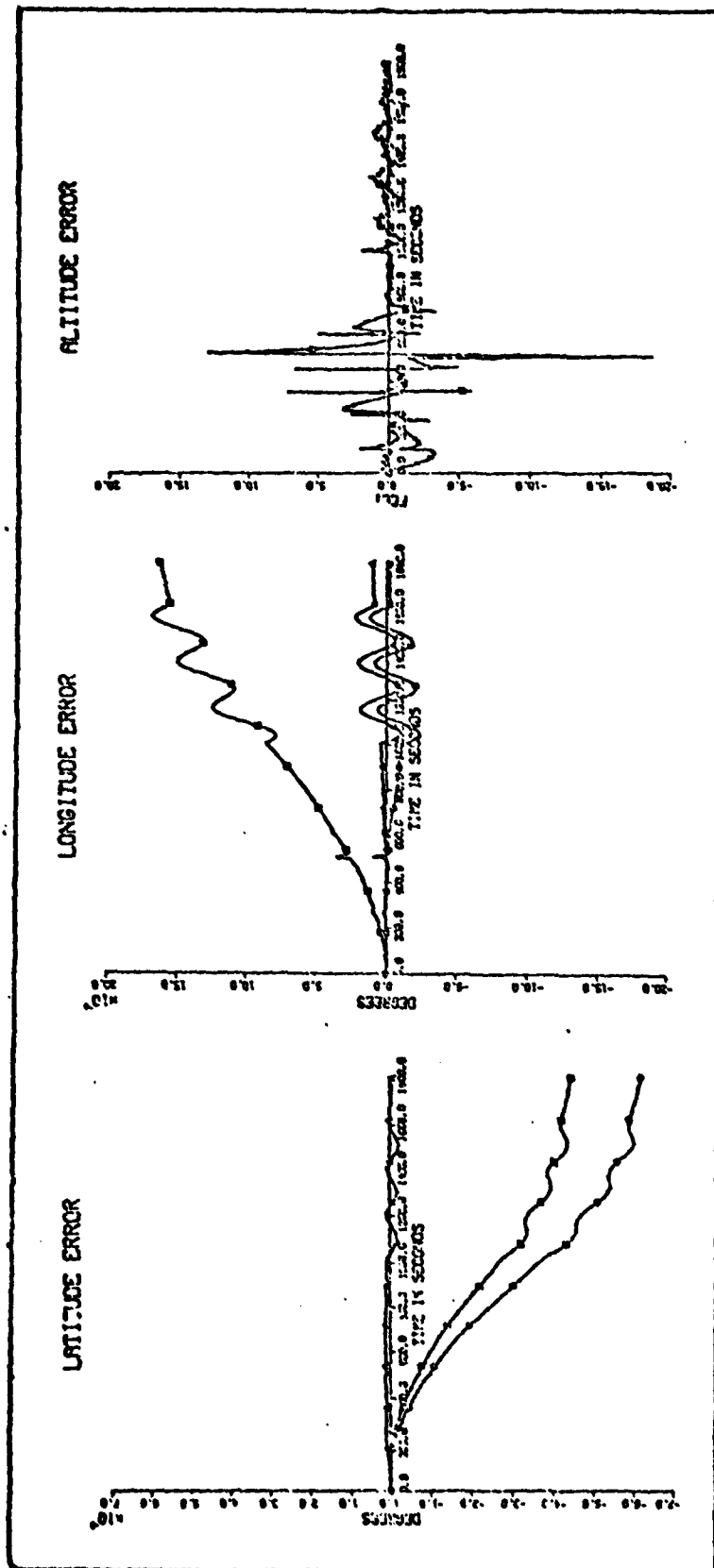


Figure 28a. Comparison of Position Errors for Cases of all Accelerometer Errors at Full Value, Accelerometer Misalignment Reduced 50%, and Ideal Sensors

- Case with accelerometer misalignment error reduced 50%.
- Case with accelerometer errors at full value.
- △ Case with ideal sensors.

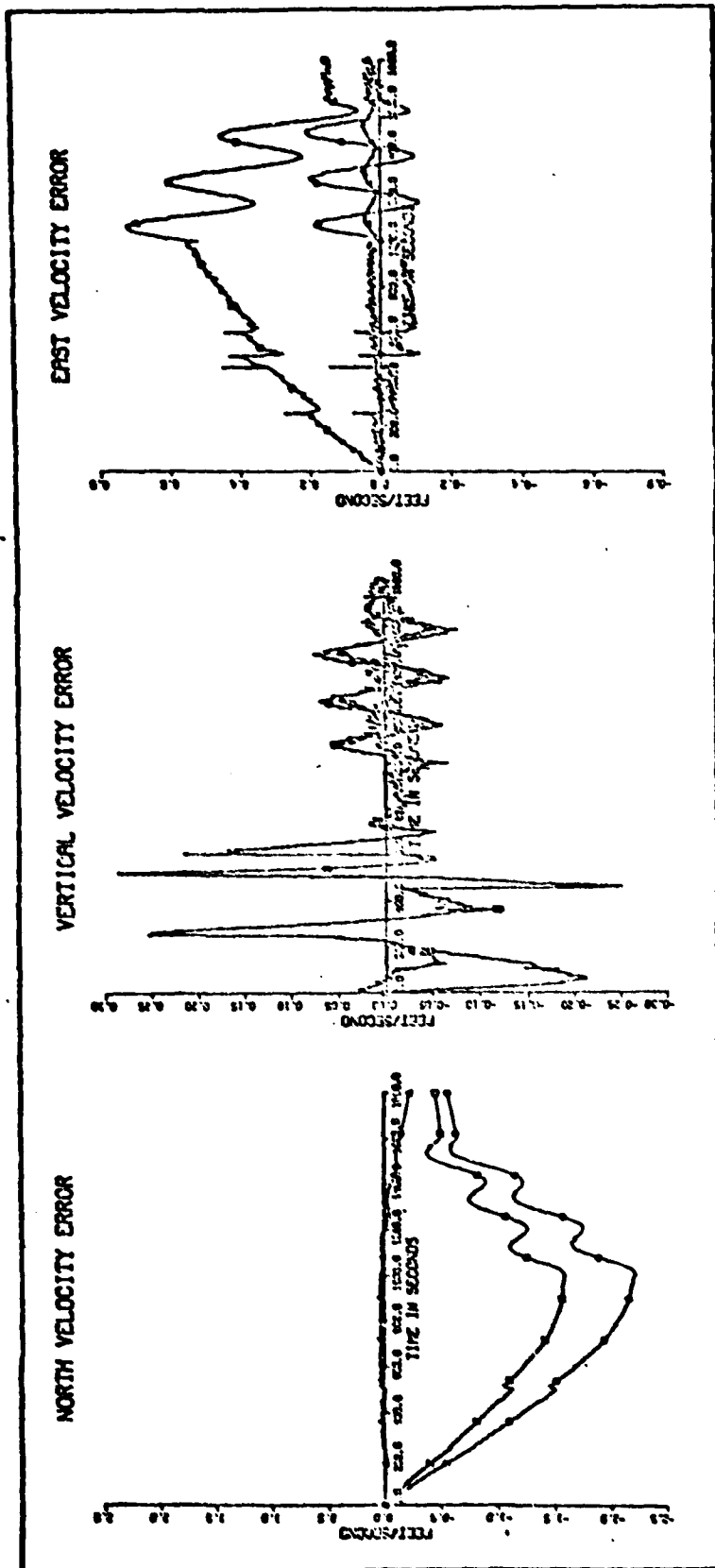


Figure 28b. Comparison of Velocity Errors for Cases of all Accelerometer Errors at Full Value, Accelerometer Misalignment Reduced 50%, and Ideal Sensors

- Case with accelerometer misalignment error reduced 50%.
- Case with accelerometer errors at full value.
- △ Case with ideal sensors.

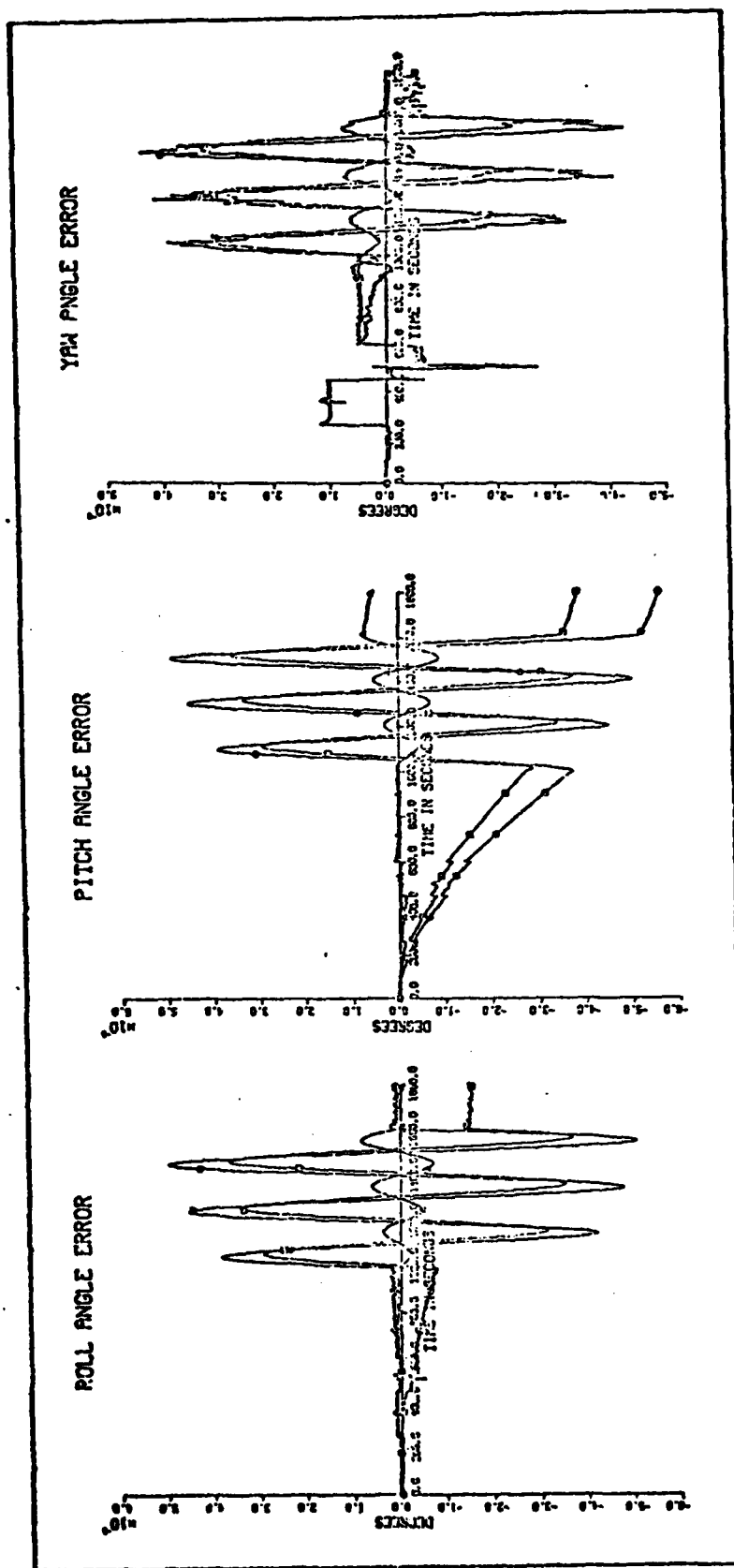


Figure 28c. Comparison of Attitude Errors for Cases of all Accelerometer Errors at Full Value, Accelerometer Misalignment Reduced 50%, and Ideal Sensors

- Case with accelerometer misalignment error reduced 50%.
- Case with accelerometer errors at full value.
- △ Case with ideal sensors.

effected about the same as when the bias is reduced, except that the errors are of opposite sign.

Other Accelerometer Errors. The other accelerometer errors, scale factor, cross-coupling, and nonlinearity, have little effect on INS errors and therefore the sensitivity of the INS errors to these errors is practically zero. The results obtained for these are shown in Figures 29, 30, and 31.

Summary of Sensitivity to Accelerometer Error. The most notable effect of the sensitivity of the INS errors to the accelerometer errors is in the way the bias and misalignment errors offset each others effects on the east velocity and longitude errors increasing 10 times and 8 times respectively when either the bias or misalignment error is reduced. This indicates that it is desirable to make comparable changes in both accelerometer errors at the same time rather than just one or the other.

The north velocity and latitude errors are equally sensitive to changes in bias and misalignment error. However, the effective change is only 27% for each. (Figure 32 shows a comparison of the results obtained when all accelerometer errors were reduced 50% and those obtained with the original values for an 84 minute simulation). Meanwhile, the east velocity and longitude errors are increased when the accelerometer bias and misalignment errors are reduced separately, because these INS parameters are dependent upon the difference in these two errors rather than the sum.

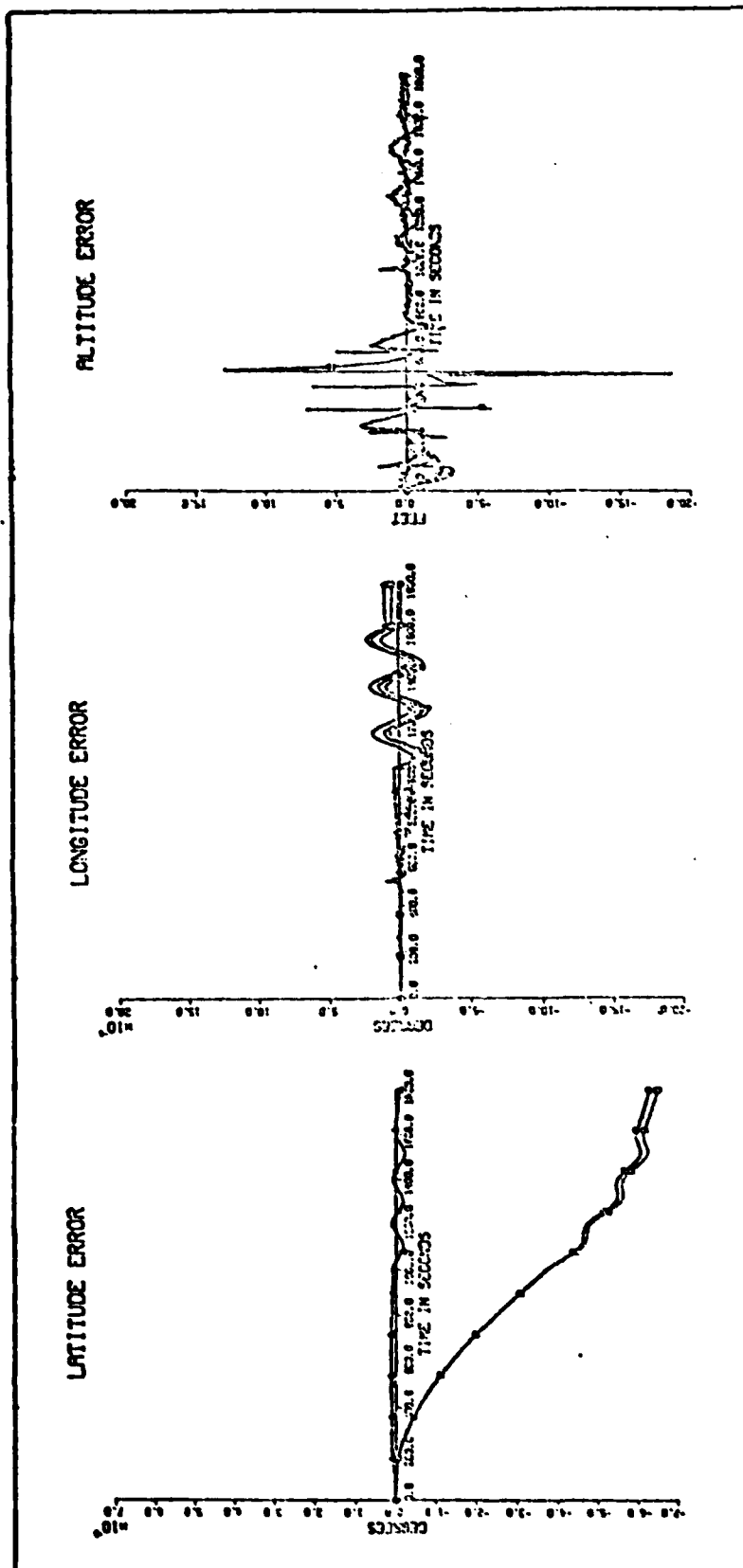


Figure 29a. Comparison of Position Errors for Cases of all Accelerometer Errors at Full Value, Accelerometer Scale Factor Reduced 50%, and Ideal Sensors

- Case with accelerometer scale factor error reduced 50%.
- Case with accelerometer errors at full value.
- △ Case with ideal sensors.

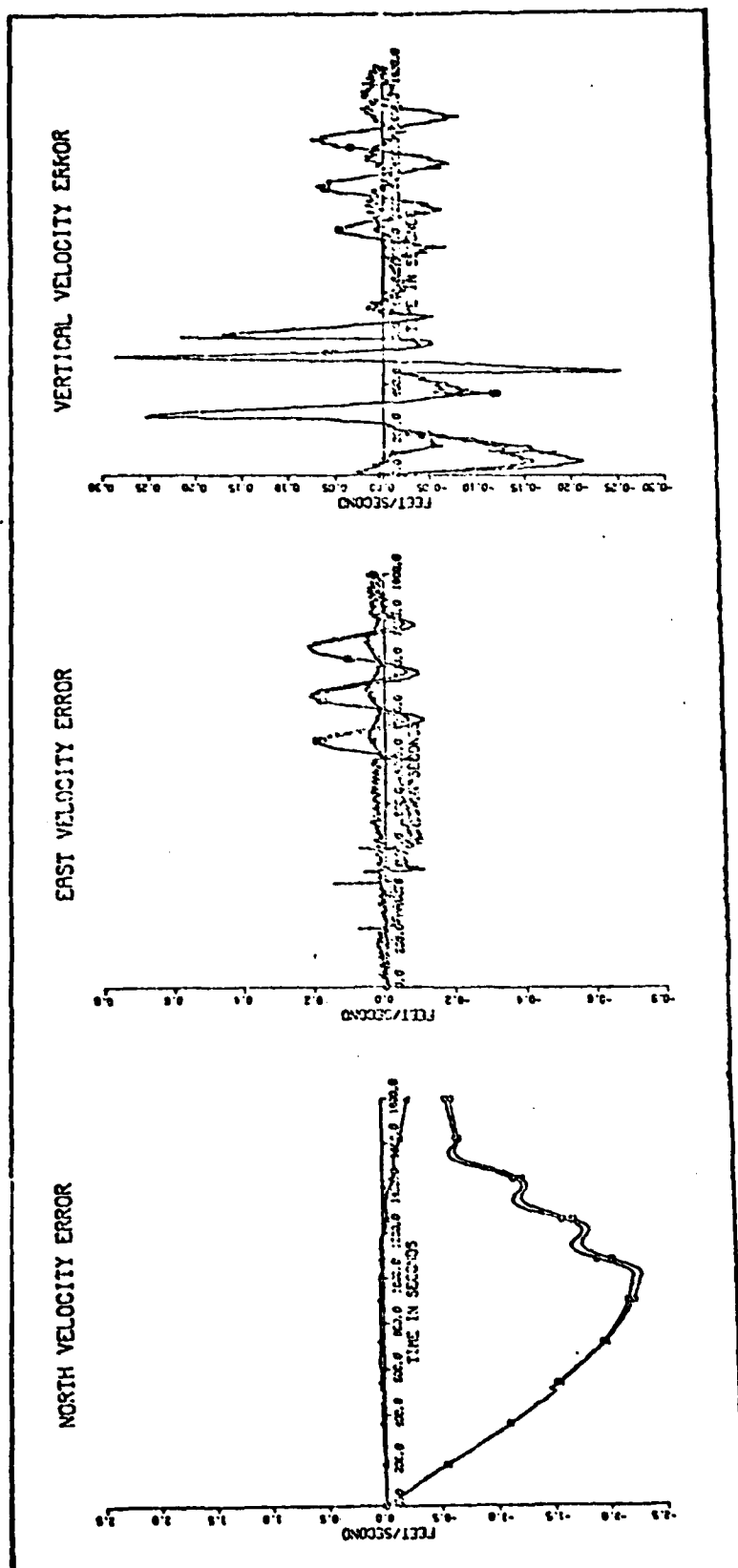


Figure 29b. Comparison of Velocity Errors for Cases of all Accelerometer Errors at Full Value, Accelerometer Scale Factor Reduced 50%, and Ideal Sensors

- Case with accelerometer scale factor error reduced 50%.
- Case with accelerometer errors at full value.
- △ Case with ideal sensors.

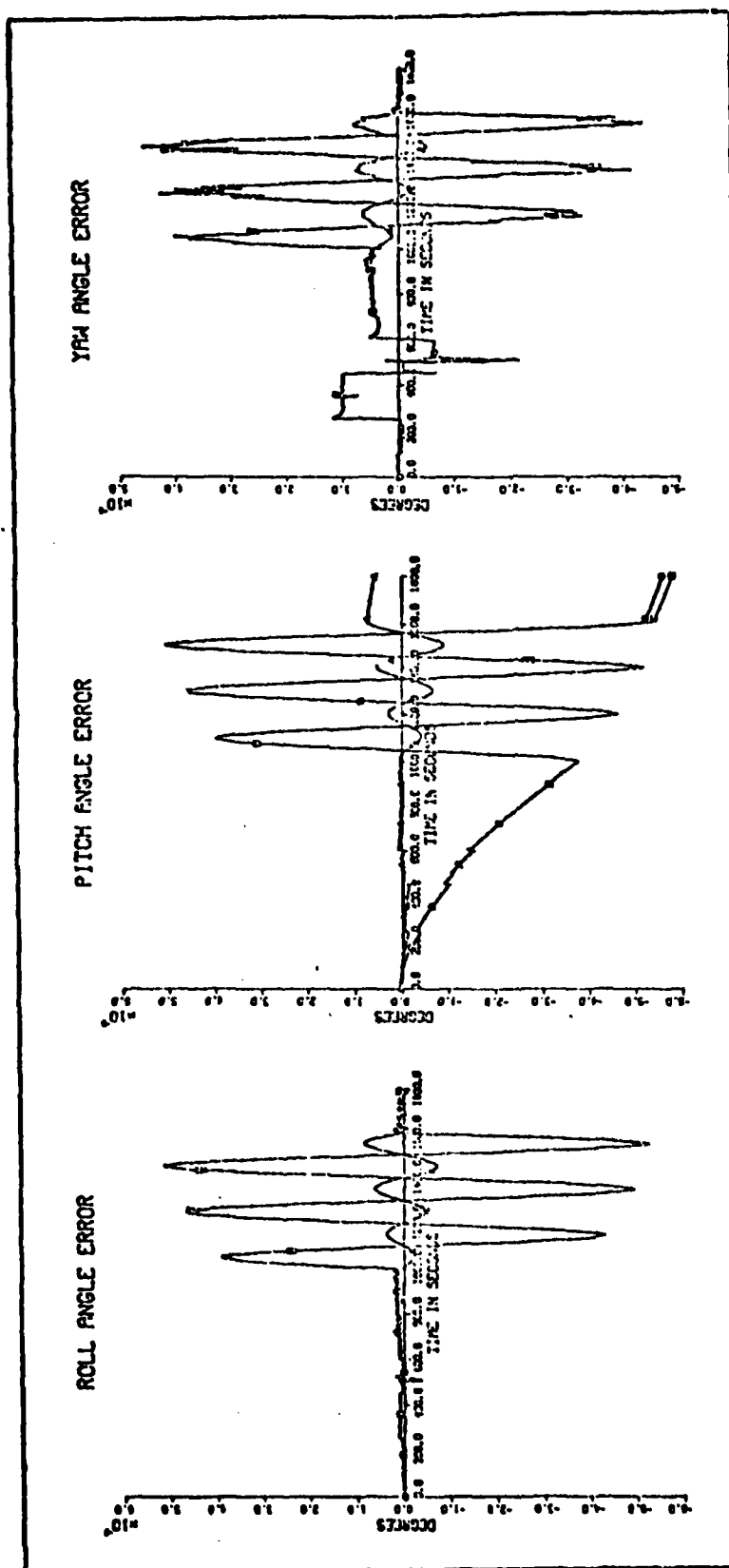


Figure 29c. Comparison of Attitude Errors for Cases of all Accelerometer Errors at Full Value, Accelerometer Scale Factor Reduced 50%, and Ideal Sensors

- Case with accelerometer scale factor error reduced 50%.
- Case with accelerometer errors at full value.
- △ Case with ideal sensors.

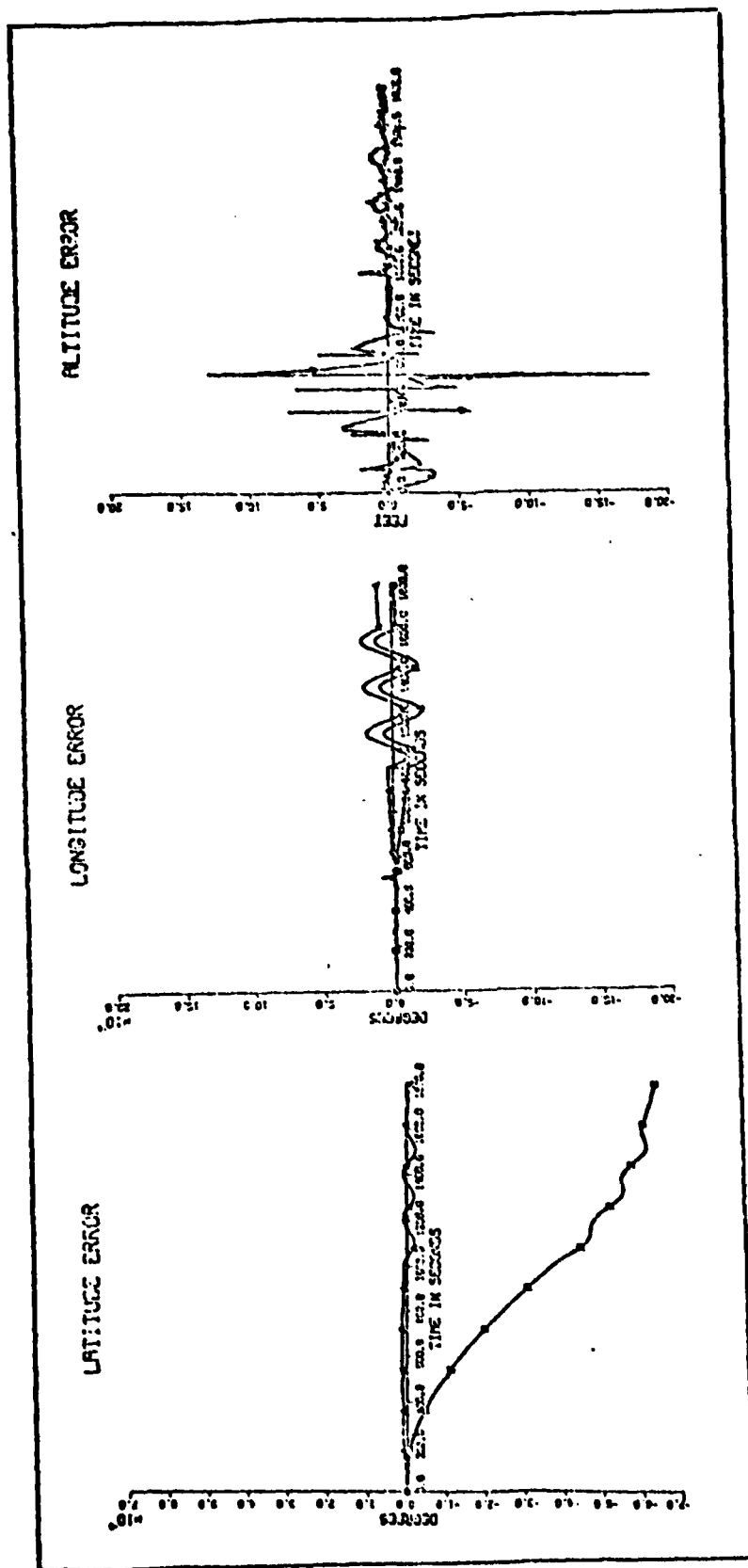


Figure 30a. Comparison of Position Errors for Cases of all Accelerometer Errors at Full Value, Accelerometer Cross-Coupling Reduced 50%, and Ideal Sensors

- *Case with accelerometer cross-coupling error reduced 50%.
 - *Case with accelerometer errors at full value.
 - △ *Case with ideal sensors.
- *These are so close in magnitude as to be essentially the same curve.

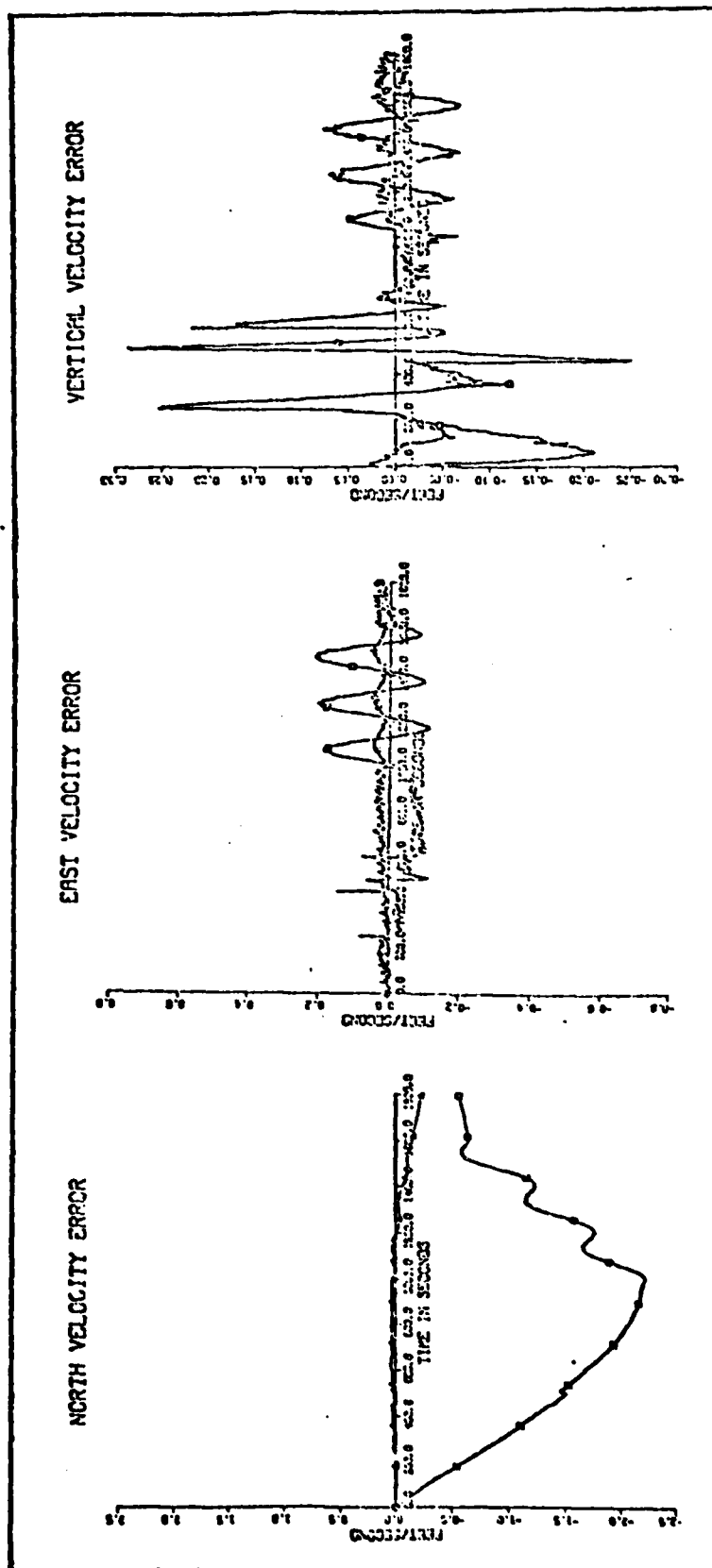


Figure 30b. Comparison of Velocity Errors for Cases of all Accelerometer Errors at Full Value, Accelerometer Cross-Coupling Reduced 50%, and Ideal Sensors

□ * Case with accelerometer cross-coupling error reduced 50%.

○ * Case with accelerometer errors at full value.

△ * Case with ideal sensors.

*These are so close in magnitude as to be essentially the same curves.

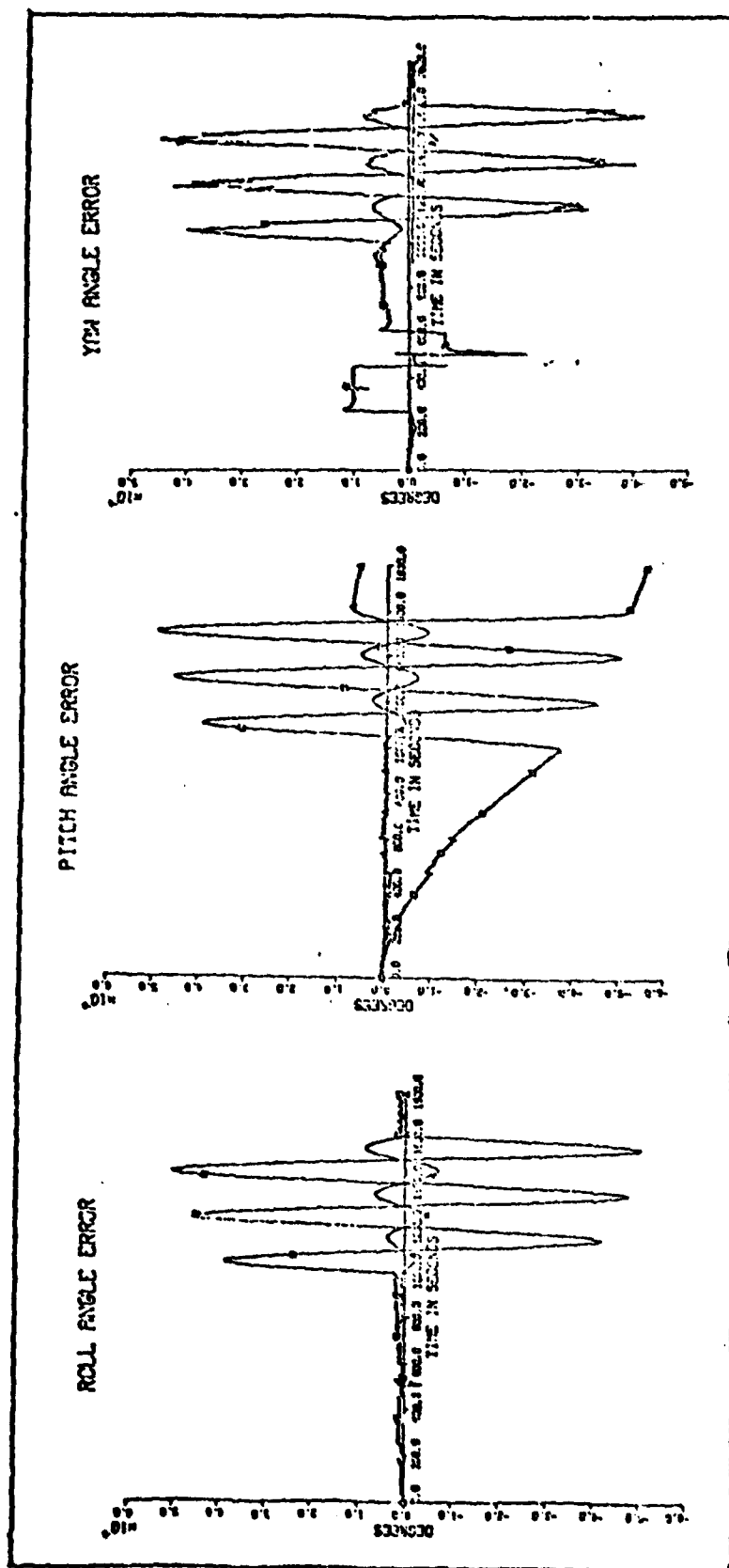


Figure 30c. Comparison of Attitude Errors for Cases of all Accelerometer Errors at Full Value, Accelerometer Cross-Coupling Reduced 50%, and Ideal Sensors

□ *Case with accelerometer cross-coupling error reduced 50%.

○ *Case with accelerometer errors at full value.

△ Case with ideal sensors.

*These are so close in magnitude as to be essentially the same curves.

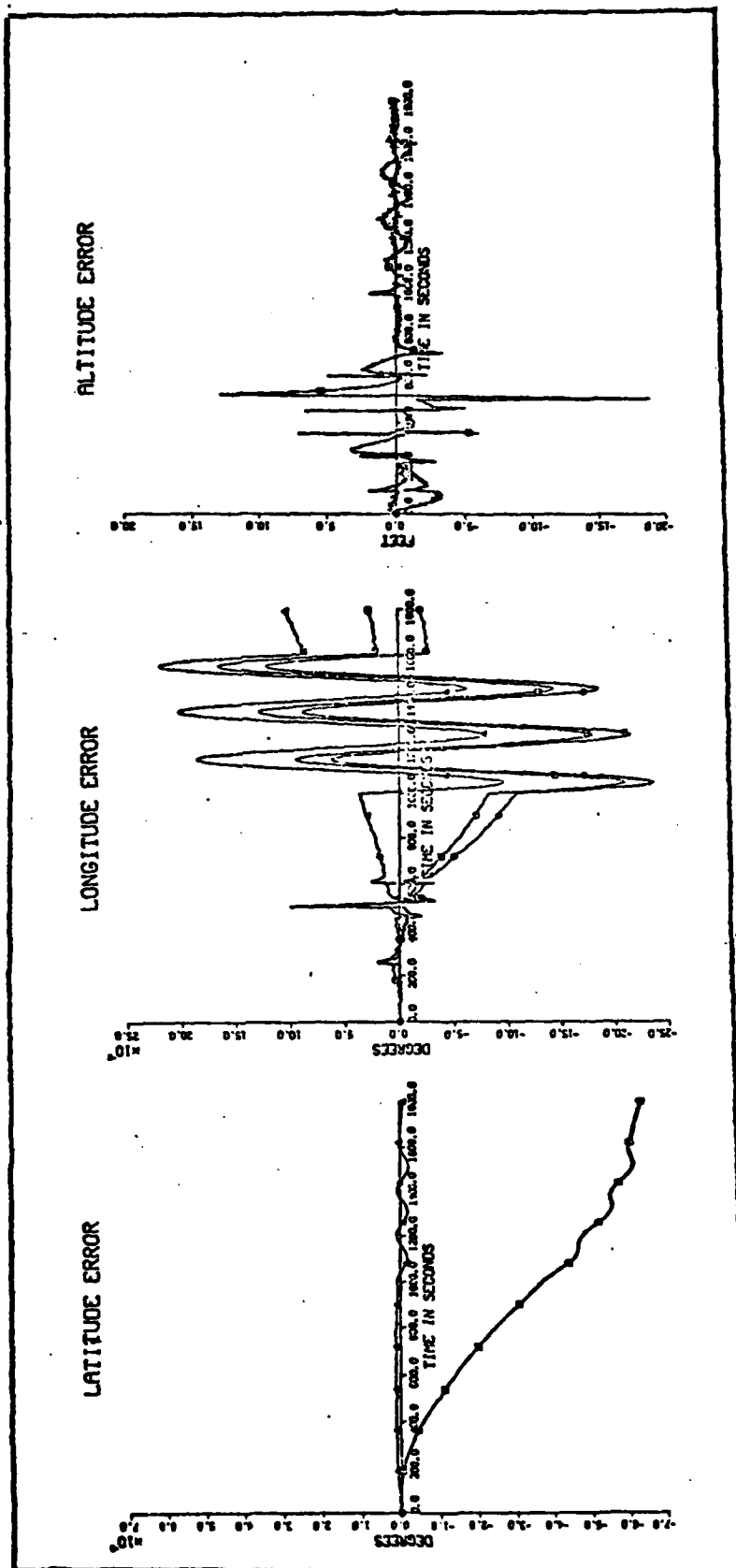


Figure 31a. Comparison of Position Errors for Cases of all Accelerometer Errors at Full Value, Accelerometer Nonlinearity Reduced 50%, and Ideal Sensors

- * Case with accelerometer nonlinearity error reduced 50%.
- * Case with accelerometer errors at full value.
- △ Case with ideal sensors.

*These are so close in magnitude as to be essentially the same curve.

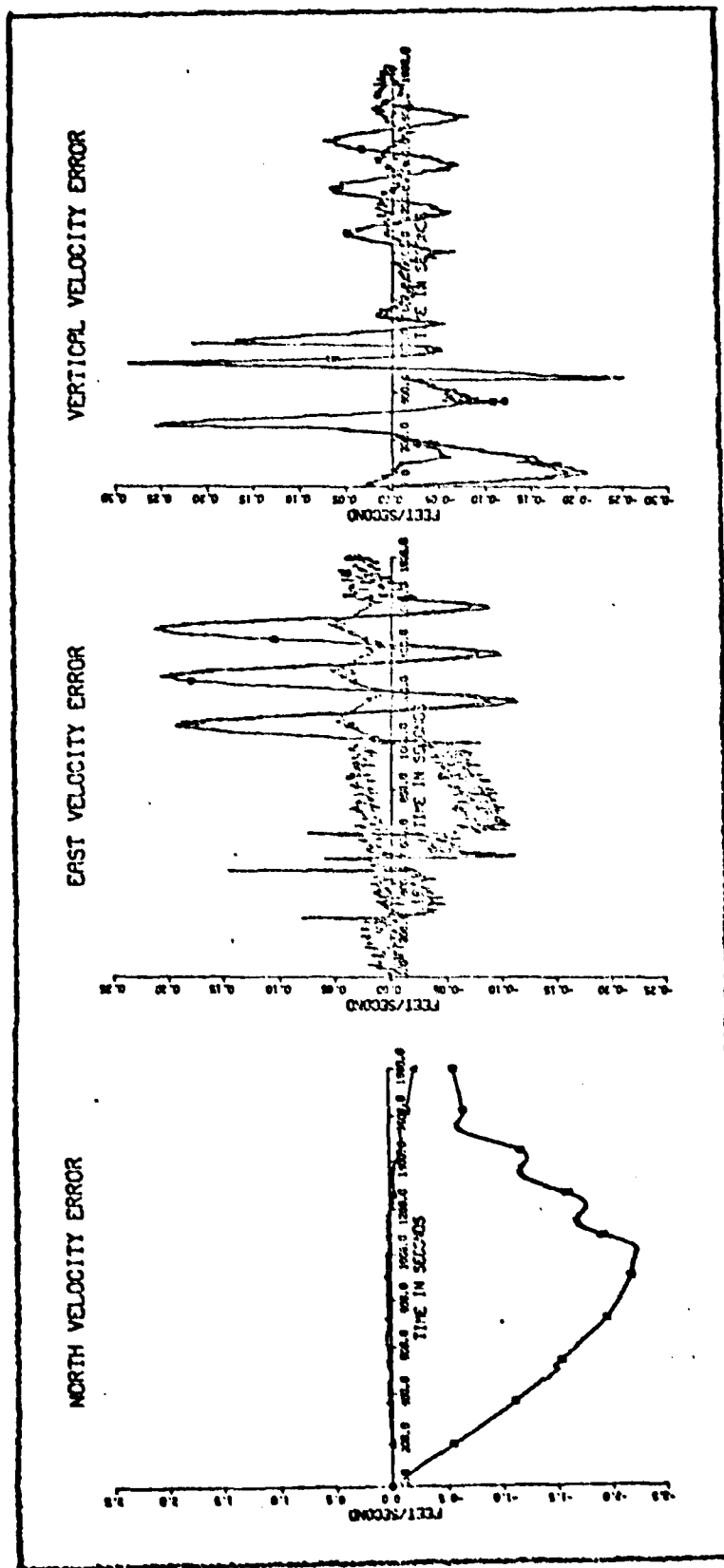


Figure 31b. Comparison of Velocity Errors for Cases of all Accelerometer Errors at Full Value, Accelerometer Nonlinearity Reduced to 50%, and Ideal Sensors

- Case with accelerometer nonlinearity error reduced to 50%.
- Case with accelerometer errors at full value.
- △ Case with ideal sensors.

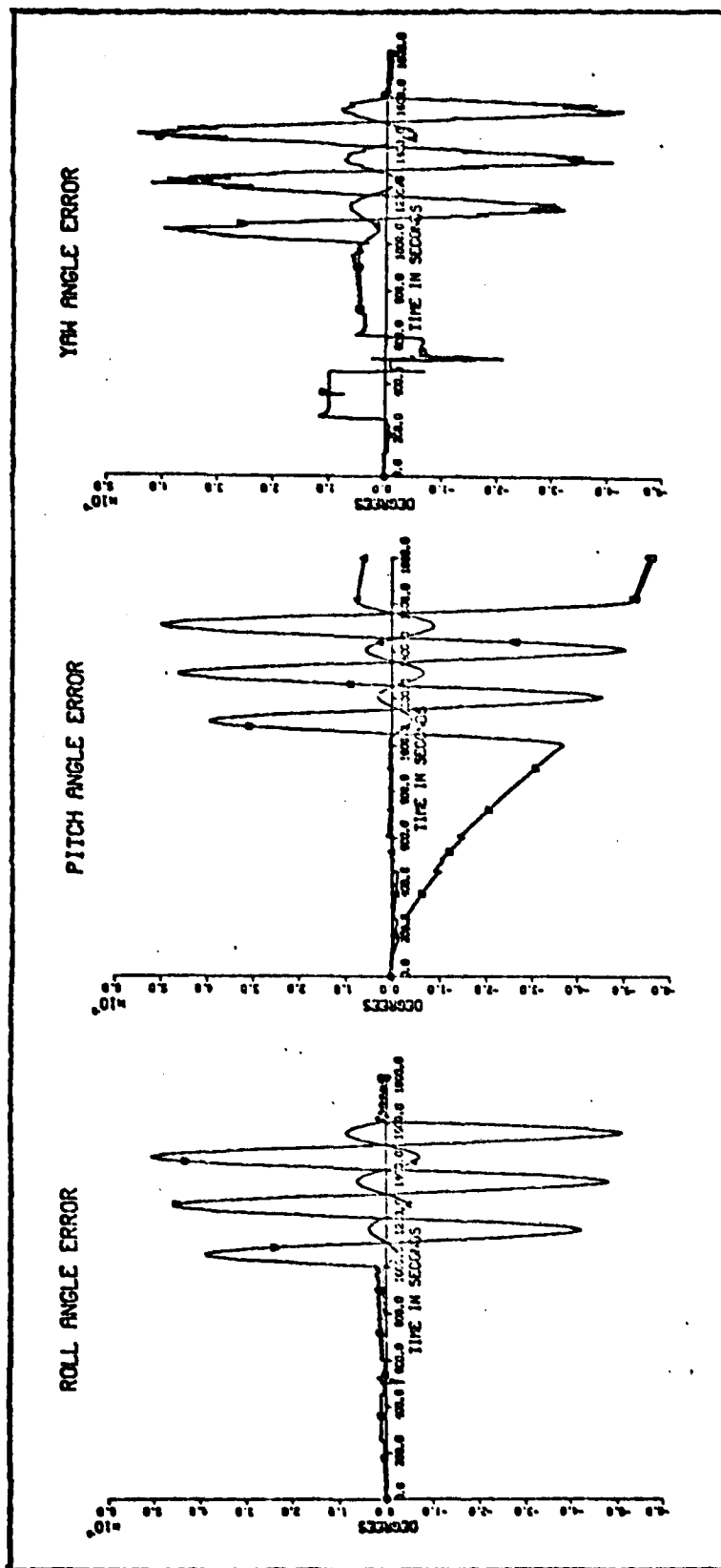


Figure 31c. Comparison of Attitude Errors for Cases of all Accelerometer Errors at Full Value, Accelerometer Nonlinearity Reduced 50% and Ideal Sensors

- Case with accelerometer nonlinearity error reduced to 50%
- Case with accelerometer errors at full value.
- △ Case with Ideal sensors.

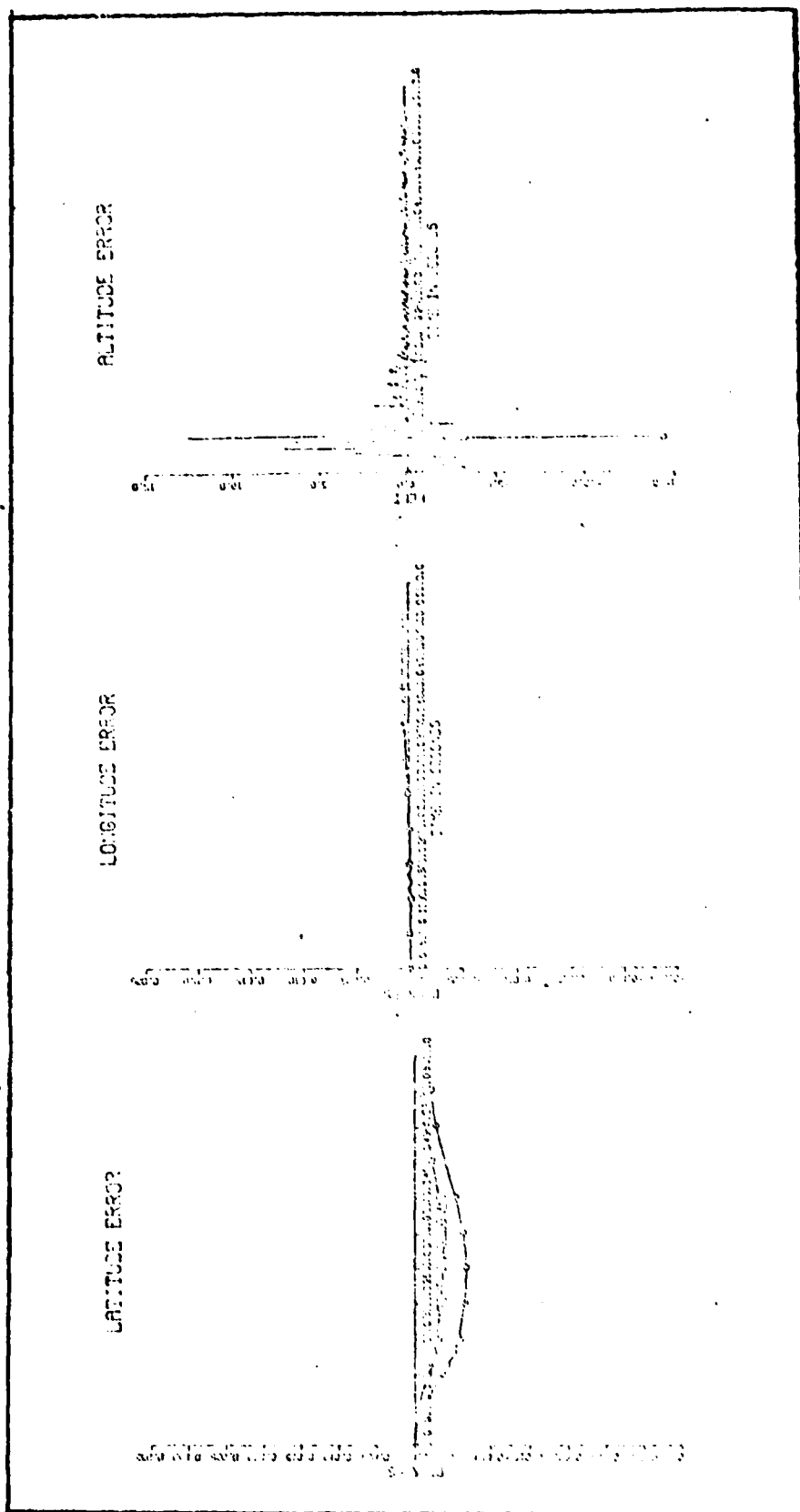


Figure 32a. Comparison of Position Errors for Cases of All Accelerometer Errors at Full Value, All Reduced 50%.

- Case with all accelerometer errors reduced to 50%.
- Case with all accelerometer errors at full value.

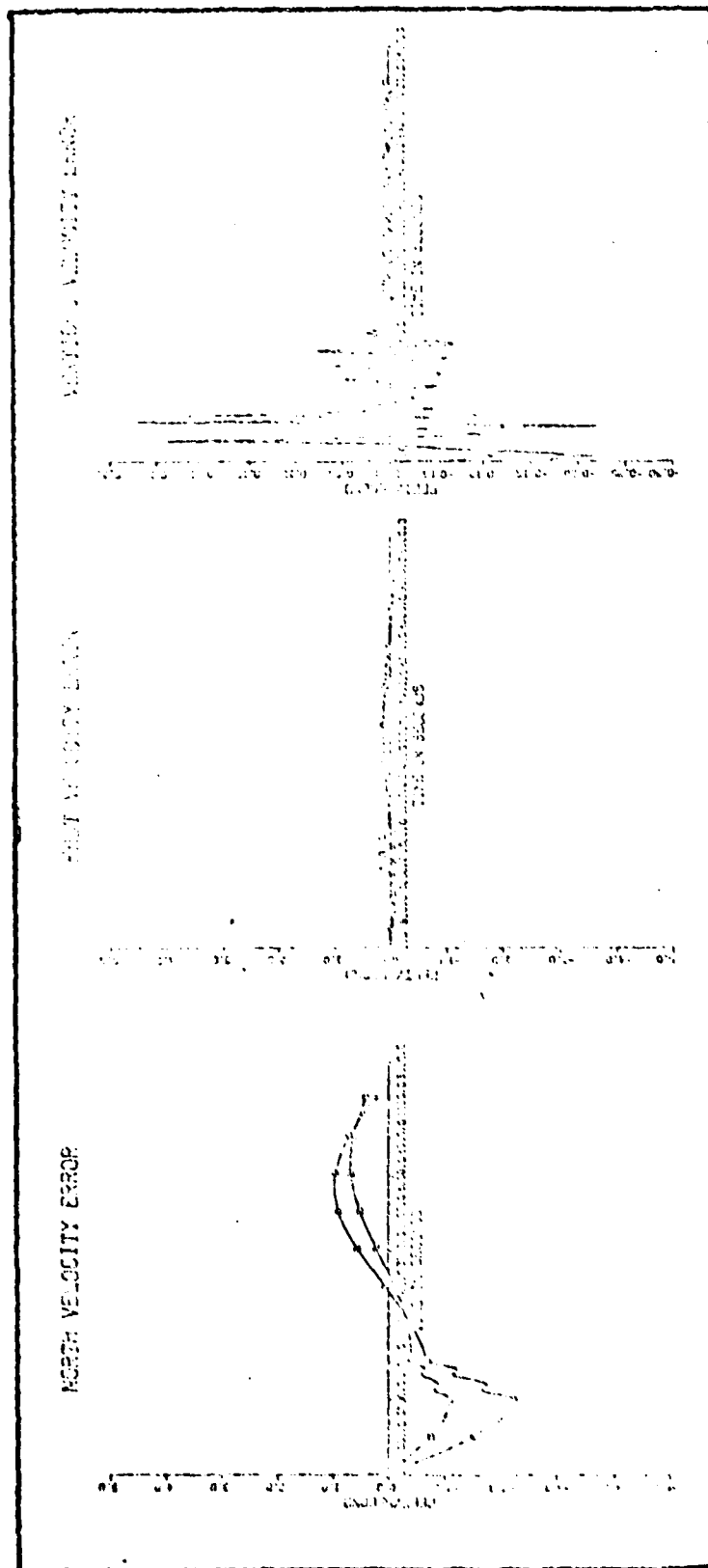


Figure 32b. Comparison of Velocity Errors for Cases of All Accelerometer Errors at Full Value, all Reduced 50%.

- Case with all accelerometers errors reduced to 50%.
- Case with all accelerometer errors at full value.

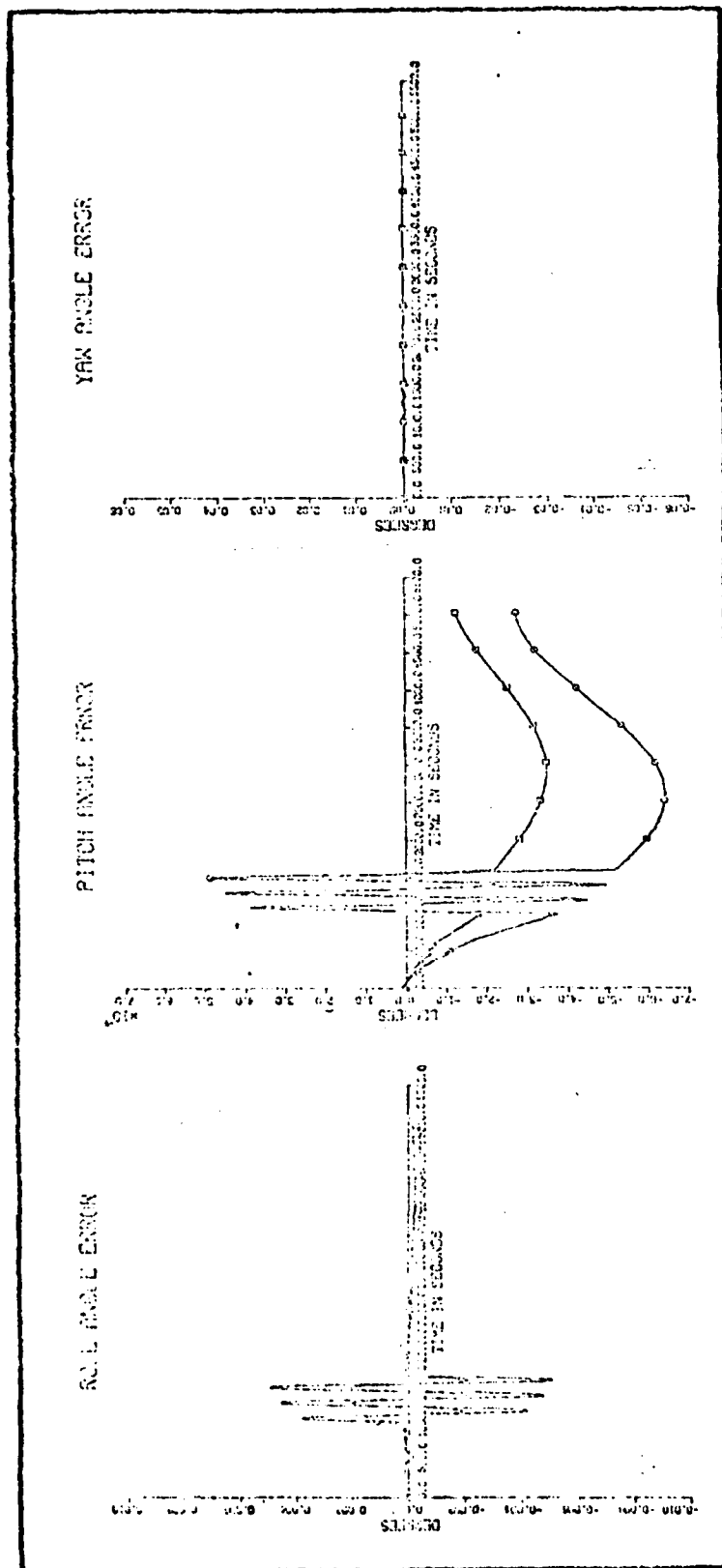


Figure 32c. Comparison of Attitude Errors for Cases of All Accelerometer Errors at Full Value, All Reduced 50%.

□ Case with all accelerometer errors reduced to 50%.
○ Case with all accelerometer errors at full value.

Table 5 shows a comparison of the results obtained in the sensitivity analysis on the accelerometer. Note that when the bias and misalignment error are reduced separately, the east velocity and longitude errors are increased. This increase disappears when both error sources are reduced since the east velocity error and thus, longitude are dependent upon the difference in the two gyro errors.

Conclusions on Sensitivity Analysis

After examining the effect on INS performance of both laser gyro and accelerometer errors, it is found that the laser gyro errors create more degradation. The findings show that improvements in gyro errors are necessary to achieve a performance specification of $\leq 1\text{nm/hr}$ position error and $\leq 3\text{ ft/sec}$ velocity error when no structural modes are sensed.

The sensitivity analysis just discussed indicates that this performance specification is achievable by reducing the sensor errors by 50%. Figure 33 shows the INS error time histories for the case using the sensor error values stated in Chapter two, Tables 1 and 2, and that using 50% of these values. This shows that with the 50% values for the sensor errors, the performance specification is met. This specification could also be met at some lower value, or a different combination of lower values, of the sensor errors.

The implications of this analysis have been that to

TABLE V

Sensitivity to Accelerometer Errors

INS Error	Bias	MIS	Scale Factor	Cross-Coupling	Nonlinearity	ALL
Latitude	27%	27%	0%	0%	0%	27%
Longitude	-1000%	-1000%	0%	0%	0%	0%
Altitude	0%	0%	0%	0%	0%	0%
North Velocity	27%	27%	0%	0%	0%	27%
East Velocity	-800%	-800%	0%	0%	0%	0%
Vertical Velocity	0%	0%	0%	0%	0%	0%

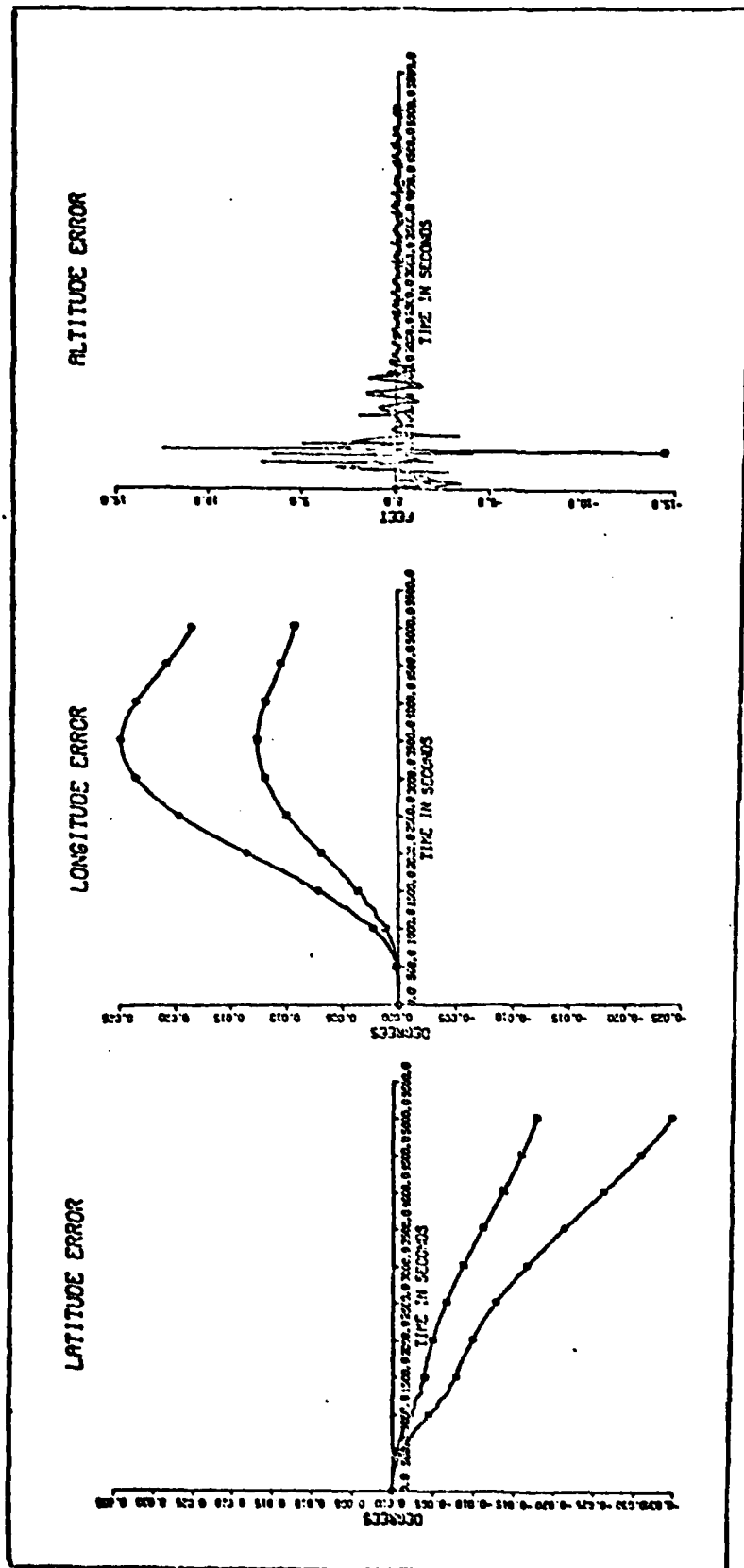


Figure 33a. Comparison of Position Errors for Cases of All Sensor Errors at Full Value and all Reduced 50%.

☐ Case with all reduced 50%.
 Case with all at full value.

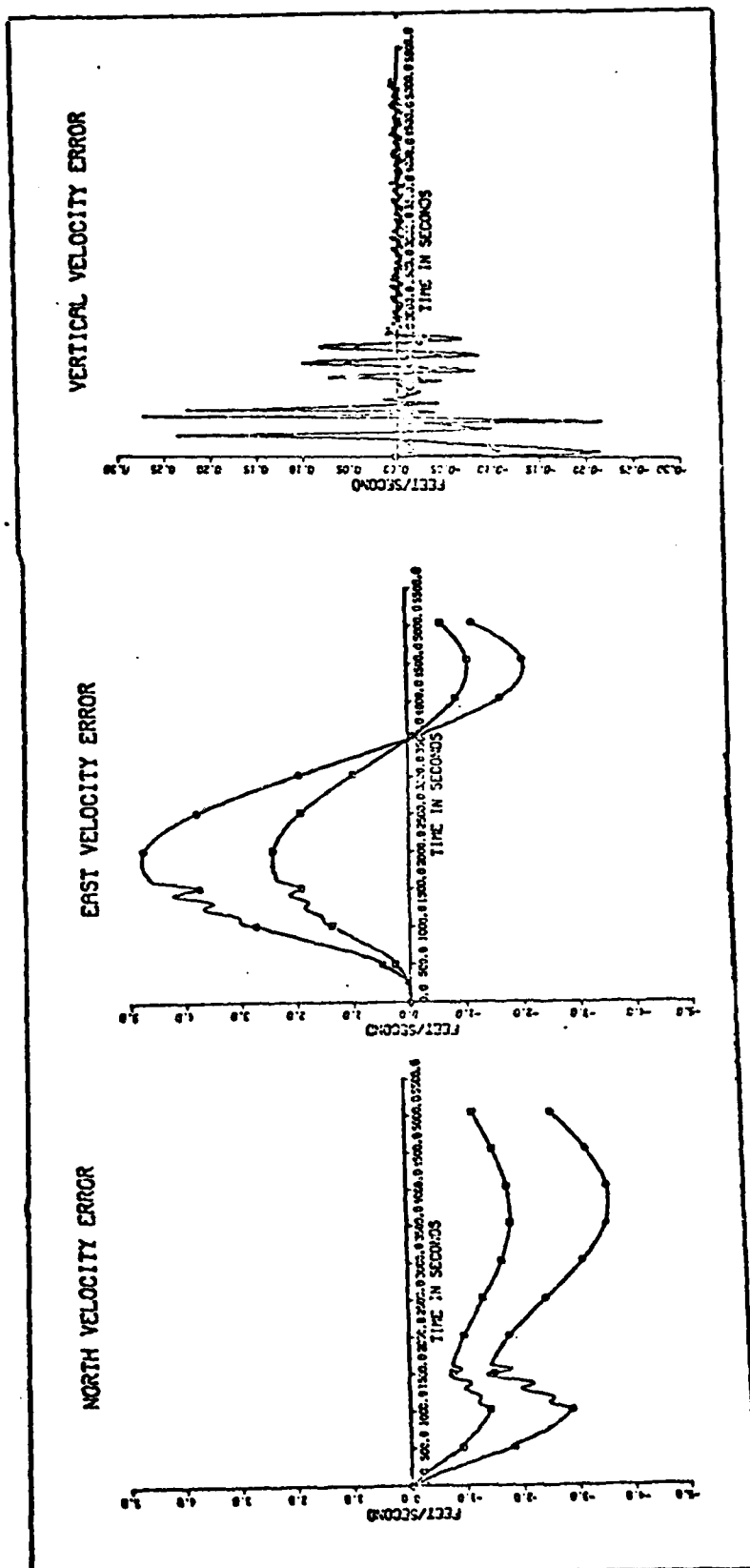


Figure 33b. Comparison of Velocity Errors for Cases of All Sensor Errors at Full Value and all Reduced 50%.

□ Case with all reduced 50%.

○ Case with all at full value.

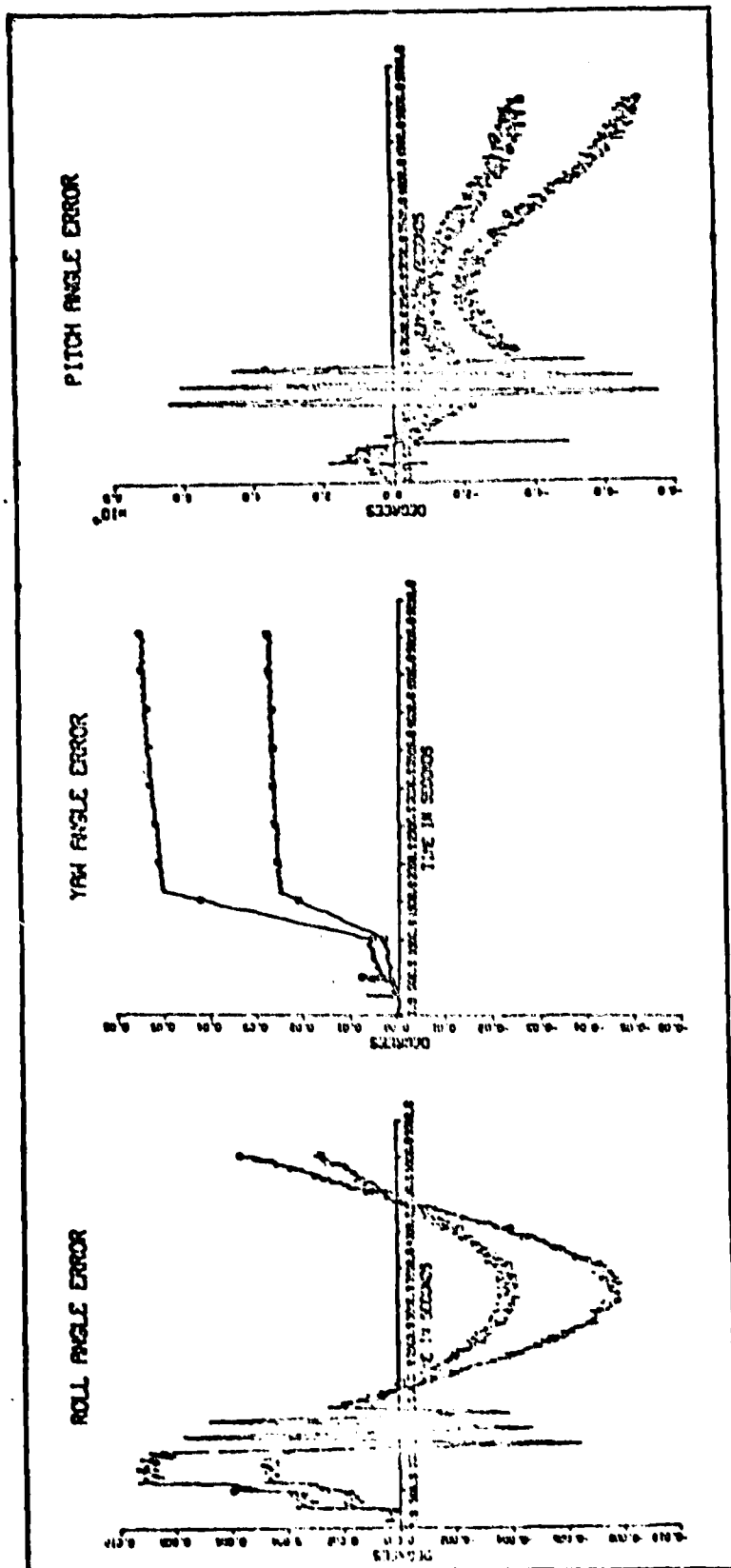


Figure 33c. Comparison of Velocity Errors for Cases of All Sensor Errors at Full Value and all Reduced 50%

- Case with all reduced 50%.
- Case with all at full value.

bring strapped-down INS performance in a high dynamic environment down to a competitive level with gimbaled systems, improvements in the quality of gyros used on the platforms is a necessary step.

CHAPTER V

Conclusions and Recommendations

This section consists of two parts. The first part is the conclusions that have been drawn from this research effort and the second is recommendations for further study in this research area.

Conclusions

Several conclusions can be drawn from this research effort. First of all, it has been shown that the laser gyro offers better performance than the mechanical two-degree-of-freedom gyro. This is determined by comparing results obtained using presently achievable performance specifications for each of these classes of instruments. The INS performance obtained for each is then compared against a performance specification of ≤ 1 nm/hr position error and ± 3 ft/sec velocity error when no structural modes are sensed. Due to its inherently larger misalignment error, the two-degree-of-freedom gyro was found to result in a much larger east velocity and, thus, longitude error, than the laser gyro.

Another conclusion that is drawn from this work is in regards to the study on the individual sensor error and structural mode effects on INS performance. In this portion of this work, it is found that the INS errors are degraded more so by the laser gyro errors than the accelerometer errors.

Also, it is found that the structural modes create substantial degradation, especially to the north velocity and latitude errors, of the INS performance. This analysis is made based on the assumption that the sensor are in an orthogonal triad at the center-of-gravity of the aircraft. This result, coupled with the laser gyro errors being more of a factor in INS performance than accelerometer errors, indicates that strong consideration of the location of the gyro should be made.

Still another important point brought out in this research is the sensitivity of the INS errors to sensor errors. Since the effects of the accelerometer errors on INS performance are practically negligible when compared to the effect of the laser gyro errors, the results of the sensitivity analysis on the laser gyro errors is more importance than that of the accelerometer. The sensitivity analysis indicates that the bias, misalignment, and scale factor errors are responsible for almost all of the laser gyro error induced INS errors. Using once again the ≤ 1 nm/hr position error and ≤ 3 ft/sec velocity error specification it is found that a 50% reduction in the laser gyro errors would result in an INS performance improvement of 50% which would be enough to meet the specification above.

A final overall conclusion is that although the high dynamic environment of a fighter-type aircraft causes unacceptable degradations in the INS performance, it does seem feasible that there is a bright future for the strapped-down INS.

Recommendations

In performing the research for this paper, several recommendations for future study have come to mind. Among these are to investigate both sensor location and configuration. The sensor location is important because of the detrimental effect that the structural modes have on the INS performance. Also, a different sensor configuration could reduce the magnitude of the misalignment error effects on the INS errors.

Another possibility for future study would be in regards to the simulation used in the present research. The present simulation model is an F-4 aircraft. It would be better, though, if the simulation could be updated such that it incorporates an F-15 or F-16 aircraft model.

A final recommendation should be to continue to refine and improve upon inertial sensor technology. The sensitivity analysis indicated that a big step forward in improving the strapped-down performance. In this area, however, the emphasis should be on the laser gyro rather than the accelerometer. Also, a more detailed sensitivity analysis may lend more insight into the minimum reduction in sensor errors that is necessary to meet the specification used in this study.

Bibliography

1. Daly, K., P. Motyka, R. Nurse, P. P. Palmer, and G. Schmidt. "Development of Capability for Multifunction Integrated Reference Assembly Evaluation." Report AFAL-TR-77-64. The Charles Stark Draper Laboratory, Inc., Cambridge, Mass., July 1977.
2. Maybeck, Peter S. "Wander Azimuth Implementation Algorithm for a Strapped-down Inertial System." Report AFFDL-TR-73-80. Wright-Patterson AFB, Ohio: Air Force Flight Dynamics Laboratory, October 1973. (AD 784752).
3. Motyka, Paul, Roy Nurse, K. Daly. "Multifunction Inertial Reference Assembly Technology (MIRAT) Simulation Development, Configuration Evaluation, and Test Plan Development". Report AFAL-TR-78-33. The Charles Stark Draper Laboratory, Inc., Cambridge, Mass., March 1978.
4. Motyka, Paul R. "Navigation Technology Development". Report AFAL-TR-76-105, Vol III, Section 6. The Charles Stark Draper Laboratory, Inc., Cambridge, Mass., October 1978.
5. Slater, John M. Inertial Navigation. New York: John Wiley and Sons, Inc., 1962.
6. Widnall, W. S. and P. A. Grundy. "Inertial Navigation System Error Models". Report TR-03-73. Intermetrics Inc., Cambridge, Mass., 11 May 1973.
7. Widnall, William S. and Prasun K. Sinka. "Some Effects of High Dynamic Trajectories on Strapped-down Inertial Navigation System Performance". Report IR-225. Intermetrics, Inc., Cambridge, Mass., 6 January 1978.

Appendix A

Notation

A brief description of the notation used in this paper is presented here as an aid to someone unfamiliar with this notation. Several different coordinate frames have been used in this paper. These coordinate frames are indicated by a lower case letter used as a subscript or a superscript, with the superscript indicating the frame in which the quantity is coordinatized while the subscript indicates the frame the quantity is referenced to. The coordinate frames used are as follows:

Inertial frame (i): This frame has origin at the earth's center and is nonrotating with respect to inertial space.

Earth frame (e): This frame is nonrotating with respect to the earth and has its origin at the center of the earth. The unit vectors are defined as follows: x_e points toward the equator and the Greenwich meridian, y_e points toward the equator and 90° e, z_e points toward the North Pole.

Computational frame (c): This is the frame in which the navigation calculations are done. Its origin is at the center of gravity of the aircraft and the unit vectors are defined as follows: x_c is positive up with respect

to Earth's surface, y_c is positive East with respect to Earth's surface, z_c is positive at some angle - (wander angle), from North with respect to the Earth's surface.

Body frame (b): The body frame has its origin at the center of gravity of the aircraft axes. Its unit vector are defined along the aircraft axes. Its unit vectors are defined along the aircraft axes, x_b is out of the top, y_b is out the right side, and z_b is out the nose of the aircraft.

Vectors are denoted by a line underneath the vector symbol; and if needed have a superscript to indicate the coordinate frame in which the vector is expressed. As an example, \underline{f}^c is the specific force vector coordinatized in the computational frame. When angular velocities are used, a double subscript is used to indicate the two reference frames between which the angular velocity exists. \underline{w}_{ie} is the angular velocity vector of frame (e) with respect to frame (i).

When the individual components of a vector are used, they will be indicated by the same symbol as the vector quantity, but without the underscoring and with an additional subscript x, y, or z to indicate which component. therefore, w_{iex}^c is the x component of angular velocity of the earth frame with respect to the inertial frame as coordinatized in the computational frame. When all components of a given vector are being defined, the following

configuration will be used:

$$\underline{w}_{ie}^c = \begin{bmatrix} w_{iex}^c \\ w_{iey}^c \\ w_{iez}^c \end{bmatrix} \quad (A-1)$$

Direction cosine matrices are used to transform a vector from one reference frame to another. They will be denoted by a capital C, with a superscript denoting the frame the vector is being transformed to and a subscript denoting the reference frame the vector is transformed from. Thus,

$$\underline{f}^c = C_b^c \underline{f}^b \quad (A-2)$$

The elements of the direction cosine matrix will be defined as follows:

$$C_b^c = \begin{bmatrix} CCB_{11} & CCB_{12} & CCB_{13} \\ CCB_{21} & CCB_{22} & CCB_{23} \\ CCB_{31} & CCB_{32} & CCB_{33} \end{bmatrix} \quad (A-3)$$

The values of the individual elements of a direction cosine matrix are determined by knowledge of their initial condition and the angular rates between the two frames of interest. Thus, if \underline{w}_{ib} (coordinatized in either frame) and the initial conditions of C_i^b are known, then $C_i^b(t)$ can be completely specified.

Another notation that has been employed is that for a skew symmetric matrix. When a cross product between two vectors is desired, $(\underline{w}_{ie} \times \underline{r})^e$, and the cross product is

coordinatized in a single frame, it is defined as,

$$w_{ie}^{ek} \underline{r}^e = (\underline{w}_{ie} \times \underline{r})^e \quad (A-4)$$

Therefore w_{ie}^{ek} is defined as,

$$w_{ie}^{ek} = \begin{bmatrix} 0 & -w_{iez}^e & w_{iey}^e \\ w_{iez}^e & 0 & -w_{iex}^e \\ -w_{iey}^e & w_{iex}^e & 0 \end{bmatrix} \quad (A-5)$$

A final note on notation is in regards to the time derivatives of vector quantities. Two notations will be used. These are dot above the vector or a lower case p preceding the vector.

$$\frac{d}{dt} \underline{f}^c = \dot{\underline{f}}^c = p \underline{f}^c \quad (A-6)$$

When the operator p is used, if the vector quantity has a superscript to indicate the frame it is coordinatized in, p will indicate the time derivative of that quantity with respect to the reference frame indicated by the superscript. If no superscript is used, the frame that the time derivative is taken in will be indicated by a subscript on the p. Therefore, the Theorem of Coriolis can be stated for any vector \underline{v} as,

$$p_i \underline{v} = p_b \underline{v} + \underline{w}_{ib} \times \underline{v} \quad (A-7)$$

Appendix B

Derivative of the Velocity Differential Equation

The velocity differential equation used in the strapped-down local vertical wander azimuth navigation model is derived here for completeness. This equation is,

$$\dot{\underline{V}} = \underline{f} + \underline{g} - (2\underline{w}_{ie}^c + \underline{w}_{ec}) \times \underline{V} \quad (\text{B-1})$$

From Newtonian mechanics, the second derivative of position as seen from an inertial frame is,

$$\underline{P_i} \ddot{\underline{r}} = \underline{G} + \underline{f} \quad (\text{B-2})$$

where \underline{f} is the specific force and \underline{G} is the mass attraction vector. Defining \underline{g} as the gravity vector composed of mass attraction and centripetal components,

$$\underline{g} = \underline{G} - \underline{w}_{ie} \times (\underline{w}_{ie} \times \underline{r}) \quad (\text{B-3})$$

equation (B-2) can be written as,

$$\underline{P_i}^2 \ddot{\underline{r}} = \underline{g} + \underline{f} + \underline{w}_{ie} \times (\underline{w}_{ie} \times \underline{r}) \quad (\text{B-4})$$

Now, defining velocity as the time rate of change of the position vector as seen from the earth frame,

$$\underline{V} = p_e \underline{r} \quad (B-5)$$

and applying the Theorem of Coriolis, the time rate of change of position with respect to inertial space is found to be,

$$\begin{aligned} p_i \underline{r} &= p_e \underline{r} + \underline{w}_{ie} \times \underline{r} \\ &= \underline{V} + \underline{w}_{ie} \times \underline{r} \end{aligned} \quad (B-6)$$

Taking the derivative of this equation results in,

$$\begin{aligned} p_i^2 \underline{r} &= p_i \underline{V} + \underline{w}_{ie} \times p_i \underline{r} \\ &= p_i \underline{V} + \underline{w}_{ie} \times \underline{V} + \underline{w}_{ie} \times (\underline{w}_{ie} \times \underline{r}) \end{aligned} \quad (B-7)$$

Now, substituting into equation (B-4) yields,

$$p_i \underline{V} = \underline{g} + \underline{f} - \underline{w}_{ie} \times \underline{V} \quad (B-8)$$

Applying the Theorem of Coriolis again gives,

$$p_i \underline{V} + \underline{w}_{ic} \times \underline{V} \quad (B-9)$$

Equating equations (B-8) and (B-9) yields,

$$\begin{aligned} p_c \underline{V} &= \underline{f} + \underline{g} - (\underline{w}_{ie} + \underline{w}_{ic}) \times \underline{V} \\ &= \underline{f} + \underline{g} - (2\underline{w}_{ie} + \underline{w}_{ec}) \times \underline{V} \end{aligned} \quad (B-10)$$

which when coordinatized in the computational frame is the velocity differential equation implement in the strapped-down simulation navigation model.

Appendix C

Coordinate Frame Relationships

Two transformation matrices are used in this report. These matrices are C_b^c , the body-to-computational transformation matrix, and C_e^c , the earth-to-computational frame transformation matrix. This section provides the derivation of these matrices. The earth-to-computational frame transformation is considered first.

Figure C-1 shows a diagram of the relationship between the earth frame and the computational frame. These two frames are aligned when α , L , and l are all zero. At this orientation the respective x , y , and z components of each frame are aligned. To get the transformation matrix between these two frames, the directional cosine matrix for a rotation of about x_c , of about y_c , and of about z_c , (α = wander angle, L =latitude, l =longitude), is found. Now defining the order of rotations as first the z_c axis rotation, then the y_c axis rotation, and finally the rotation about the x_c axis, the direction cosine matrices are multiplied together to form C_e^c .

$$C_e^c = \begin{bmatrix} 1 & 0 & 0 \\ 0 & \cos\alpha & \sin\alpha \\ 0 & -\sin\alpha & \cos\alpha \end{bmatrix} \begin{bmatrix} \cos L & 0 & \sin L \\ 0 & 1 & 0 \\ -\sin L & 0 & \cos L \end{bmatrix} \begin{bmatrix} \cos l & \sin l & 0 \\ -\sin l & \cos l & 0 \\ 0 & 0 & 1 \end{bmatrix} \quad (C-1)$$

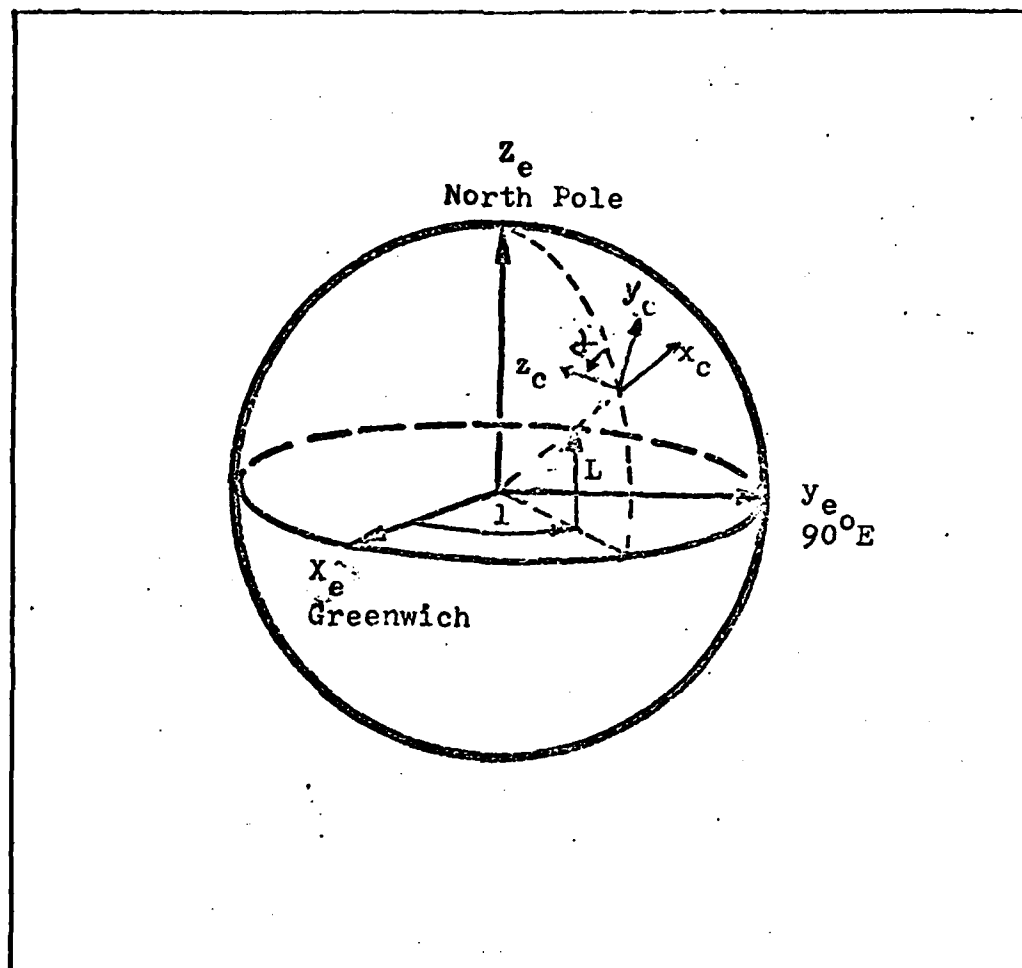


Figure C-1. Wander Azimuth (Computation) and Earth Coordinated Frames (Ref 2:9)

Defining the elements of C_e^C as

$$C_e^C = \begin{bmatrix} CCE_{11} & CCE_{12} & CCE_{13} \\ CCE_{21} & CCE_{22} & CCE_{23} \\ CCE_{31} & CCE_{32} & CCE_{33} \end{bmatrix} \quad (C-2)$$

results in,

$$\begin{aligned} CCE_{11} &= \cos L \cos l \\ CCE_{12} &= \cos L \sin l \\ CCE_{13} &= \sin L \\ CCE_{21} &= -\sin \alpha \sin L \cos l - \sin l \cos \alpha \\ CCE_{22} &= -\sin \alpha \sin L \sin l + \cos l \cos \alpha \\ CCE_{23} &= \sin \alpha \cos L \\ CCE_{31} &= -\cos \alpha \sin L \cos l + \sin \alpha \sin l \\ CCE_{32} &= -\cos \alpha \sin L \sin l - \sin \alpha \cos l \\ CCE_{33} &= \cos \alpha \cos L \end{aligned} \quad (C-3)$$

From this, latitude, longitude, and wander angle can be calculated.

$$L = \tan^{-1}(CCE_{13} / (CCE_{11}^2 + CCE_{13}^2)^{1/2}) \quad (C-4)$$

$$l = \tan^{-1}(CCE_{12} / CCE_{11}) \quad (C-5)$$

$$\alpha = \tan^{-1}(CCE_{23} / CCE_{33}) \quad (C-6)$$

The other transformation matrix used is the one to transform a vector from the body-to-the-computational frame. Figure C-2 shows the relationship between these

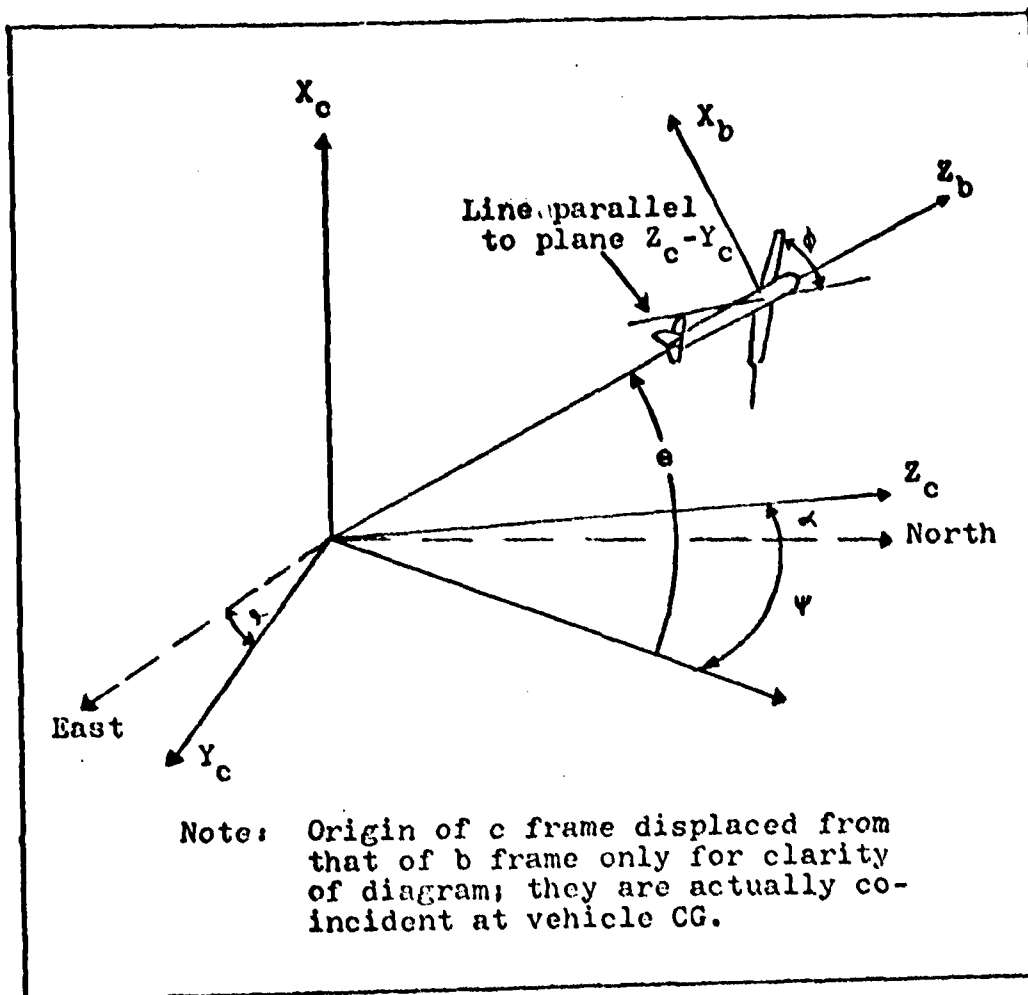


Figure C-2. Wander Azimuth (computation) and Body Coordinate Frames (Ref 2:13)

frames. As was done with the earth-to-computational frame transformation, the body-to-computational frame transformational matrix is defined as the product of three direction cosine matrices. Using the Euler angles for the respective rotations results in a rotation of Φ about z_c , θ about y_c , and finally $(\psi + \alpha)$ about x_c :

$$C_b^c = \begin{bmatrix} 1 & 0 & 0 \\ 0 & \cos(\psi + \alpha) & \sin(\psi + \alpha) \\ 0 & -\sin(\psi + \alpha) & \cos(\psi + \alpha) \end{bmatrix} \begin{bmatrix} \cos\theta & 0 & \sin\theta \\ 0 & 1 & 0 \\ -\sin\theta & 0 & \cos\theta \end{bmatrix} \begin{bmatrix} \cos\phi & -\sin\phi & 0 \\ \sin\phi & \cos\phi & 0 \\ 0 & 0 & 1 \end{bmatrix} \quad (C-7)$$

where α is the roll angle, θ is the pitch angle, and ψ is the yaw angle.

Defining the elements of C_b^c as,

$$C_b^c = \begin{bmatrix} CCB_{11} & CCB_{12} & CCB_{13} \\ CCB_{21} & CCB_{22} & CCB_{23} \\ CCB_{31} & CCB_{32} & CCB_{33} \end{bmatrix} \quad (C-8)$$

results in,

$$CCB_{11} = \cos\theta \cos\phi \quad (C-9)$$

$$CCB_{12} = -\cos\theta \sin\phi \quad (C-10)$$

$$CCB_{13} = \sin\theta \quad (C-11)$$

$$CCB_{21} = \cos(\psi + \alpha) \sin\phi - \sin(\psi + \alpha) \sin\theta \cos\phi \quad (C-12)$$

$$CCB_{22} = \cos(\psi + \alpha) \cos\phi + \sin(\psi + \alpha) \sin\theta \sin\phi \quad (C-13)$$

$$CCB_{23} = \sin(\psi + \alpha) \cos\theta \quad (C-14)$$

$$CCB_{31} = -\sin(\psi + \alpha) \sin\phi - \cos(\psi + \alpha) \sin\theta \cos\phi \quad (C-15)$$

$$CCB_{32} = -\sin(\psi + \alpha) \cos\phi + \cos(\psi + \alpha) \sin\theta \sin\phi \quad (C-16)$$

$$CCB_{33} = \cos(\psi + \alpha) \cos\theta \quad (C-17)$$

From these elements, the Euler angles, roll, pitch, and yaw are determined:

$$\phi = \tan^{-1}(-CCB_{12} / CCB_{11}) \quad (C-18)$$

$$\theta = \tan^{-1}(CCB_{13} / (CCB_{11}^2 + CCB_{12}^2)^{\frac{1}{2}}) \quad (C-19)$$

$$\psi = \tan^{-1}(CCB_{23} / CCB_{33}) - \alpha \quad (C-20)$$

VITA

Richard H. Reynolds was born 30 January 1956 in Asmara, Ethiopia. He graduated from Greenwood High School, Greenwood, South Carolina, in 1974. From 1974-1978, he attended Clemson University from which he received a Bachelor of Science Degree in Electrical Engineering. Upon graduation he was commissioned in the United States Air Force and entered the Air Force Institute of Technology as a candidate for a Master of Science in Electrical Engineering.

Permanent Address: Route 10 Box 32
Greenwood, S. C. 29646

UNCLASSIFIED

SECURITY CLASSIFICATION OF THIS PAGE(When Data Entered)

20. errors in position and velocity to each inertial sensor is determined. Using this sensitivity analysis, the sensor parameters required to obtain a performance specification of ± 1 nm/hr position error and ± 3 ft/sec velocity error are defined. Finally, recommendations of areas for improvement are presented.

SECURITY CLASSIFICATION OF THIS PAGE(When Data Entered)